

# UNIVERSITY OF NAPLES FEDERICO II

Department of Structures for Engineering and Architecture

PHD PROGRAMME IN  
STRUCTURAL, GEOTECHNICAL AND SEISMIC ENGINEERING  
XXIX CYCLE



**STEFANO CAROZZA**

PHD THESIS

**PERFORMANCE-BASED STRUCTURAL  
RELIABILITY ASSESSMENT FOR RAINFALL-  
INDUCED HYDROGEOLOGICAL PHENOMENA**

TUTOR: PROF. FATEMEH JALAYER

**2017**



---

## Contributions and data source

One of the main challenges of this work is to manage in a systematic way the interaction between the several disciplines involved in the hydrogeological risk assessment (i.e., geological, geotechnical, hydrologic, hydraulic, structural engineering, probabilistic and reliability assessment). It is clear that we would not have been able to make hydrogeological risk assessment without data, methods and technical support provided by several experts in the different disciplines.

To this end, a brief list of the data sources used in this thesis is reported below:

1. Geological studies for Sarno and Castellammare di Stabia, definition of debris flow scenarios, volumes estimation: Prof. **Antonio Santo**, Dr. **Melania De Falco** and **Dr. Giovanni Forte** (*Department of Civil, Architectural and Environmental Engineering of the University of Naples Federico II*).
2. Hydraulic propagation and hazard maps production for the cases study of Sarno and Castellammare di Stabia: Prof. **Francesco De Paola**, Dr. **Giuseppe Speranza** (*Department of Civil, Architectural and Environmental Engineering of the University of Naples Federico II*).
3. Fast visual survey of buildings in the City of Sarno **Luca Martino** (a graduate student of the program of *Structural and Geotechnical Engineering*).
4. Hydraulic propagation of the debris flow of October 2009 event for the case study of Scaletta Zanclea: Prof. **Giuseppe Tito Aronica** (*Department of Engineering of University of Messina*).
5. Regional maps: Technical Regional Map (CTR 2004).
6. Survey of the buildings in Castellammare di Stabia: **Istituto Cooperativo per l'Innovazione** (ICIE, Naples).



---

## Abstract

Risk assessment for rainfall-induced hydrogeological phenomena in urban areas is an important issue for stakeholders, in order to manage the hydrogeological risk in urbanized areas and to plan the future urbanization. The aim of this work is to propose a complete framework for risk assessment in urban areas for two main rainfall-induced phenomena: debris flow and flooding. The work involves several disciplines and wraps them together in a systematic way in order to be used as a DSS (Decision Support System). The work presented in this thesis is developed within the Italian research project METROPOLIS funded by the National Operative Program (PON 03PE\_00093\_4) and focused on the study of the integrated and sustainable methods and technologies for resilience and safety of urban systems. The project aims at defining the methodology and at developing innovative and sustainable technologies for the evaluation and management of the natural and anthropic risks for urban systems, in order to address mitigation strategies based on integrated decision support systems.

The thesis focuses on the reliability assessment of portfolios of buildings located in areas susceptible to hydrogeological hazards. A portfolio of buildings can include one or more structural classes where a given class is characterized by a group of features (e.g., building material, decade of construction, number of storeys, etc.). Within each class, specific statistical considerations are made to characterize both the uncertainty due to lack of knowledge and building-to-building variability in mechanical, geometrical and load properties. The adopted framework is draws obvious analogies with the Performance Based Earthquake Engineering (PBEE) framework. In the context of risk assessment, three main aspects are investigated: the hazard, the vulnerability and the exposure. The first two aspects are described in detail; the exposure quantification, instead, is outside the scope of this work.

The hazard evaluation involves specific geological, geotechnical, hydrological and hydraulic competences. This issue has been addressed by a team of specialists that produced the hazard maps for this work for both debris flows and flooding. While for flooding problem it is possible to obtain a complete hazard curve (for each geographical point of

---

interest) in terms of intensity measure (e.g., flood height and/or flood velocity) versus return period of the rainfall event, for debris flow phenomena the question is much more complex. In case of debris flow, in fact, the event does not depend only on return period of the rainfall that triggers the debris flow but depends also on the boundary and initial conditions of the slope. The knowledge of these conditions is almost never available in un-gauged conditions; hence, a scenario-based approach has been adopted in order to solve the risk assessment problem.

Analytic vulnerability assessment is performed by calculating the robust fragility curves representing the probability to have an intensity measure value lower than or equal to a certain value which correspond to assumed limit states –considering also the uncertainties in the parameters of the fragility model. The fragility curves represent the vulnerability of a structural class and are calculated by adopting a Bayesian approach and relying on a Monte Carlo Simulation (MCS) process for the propagation of uncertainties. In order to estimate the structural capacity for a given limit state, an incremental analysis procedure has been performed during the MCS. The structural model is elastic and finite-element-based accompanied by a defined set of safety checks in order to catch all the potential failure mechanisms of the walls –arguably the most vulnerable structural elements directly subjected to hydrogeological-induced actions.

In this thesis, the proposed framework is implemented in an Object-Oriented Java software tool, named HyDRA. HyDRA performs the propagation of uncertainties in a MCS process by executing a specified number of structural analyses of models generated according to user-defined probability distributions (through the MCS process). HyDRA produces as results: the safety checks, the robust fragility curves for specified limit states and the risk maps.

The framework is applied on three case studies. In order to validate the structural model and the analysis procedure, two past events have been considered: the flash flood/debris flow event in Scaletta Zanclea (Messina, Italy) occurred in 2009 (a single masonry building has been considered) and the debris flow in Sarno (Salerno, Italy) occurred in 1998 where a portfolio of buildings has been considered. Finally, an application on Castellammare di Stabia (Naples, Italy) is proposed in order to provide the risk maps as an instrument in the service of risk management and promoting risk awareness for hydrogeological phenomena.

**Keywords:** risk assessment, structural reliability, limit states, uncertainty propagation, hazard, hydrogeological phenomena, debris flow, flood, vulnerability, fragility, safety checking, decision support system, software implementation.

---

# Table of contents

CONTRIBUTIONS AND DATA SOURCE .....	3
ABSTRACT .....	5
TABLE OF CONTENTS.....	7
<b>CHAPTER 1.....</b>	<b>11</b>
INTRODUCTION.....	11
1.1 <i>Motivation</i> .....	12
1.2 <i>Objectives and products</i> .....	13
1.3 <i>Organization and outline</i> .....	14
1.4 <i>Basic definitions</i> .....	15
1.5 <i>Performance-based framework</i> .....	17
1.6 <i>The case studies</i> .....	19
1.6.1 <i>Masonry building in Scaletta Zanclea</i> .....	19
1.6.2 <i>Portfolio of buildings in Sarno</i> .....	22
1.6.3 <i>Portfolio of buildings in Castellammare di Stabia</i> .....	23
<b>CHAPTER 2 .....</b>	<b>25</b>
HYDROGEOLOGICAL HAZARD .....	25
2.1 <i>Landslide hazard assessment</i> .....	25
2.1.1 <i>Overview</i> .....	25
2.1.2 <i>Debris- and mud-flow</i> .....	25
2.1.3 <i>Debris flow peak discharge estimation</i> .....	29
2.1.4 <i>Uncertainty modelling in peak discharge estimation</i> .....	32
2.2 <i>Flood hazard assessment</i> .....	33
2.3 <i>Bi-dimensional numerical propagation in FLO-2D</i> .....	35
2.3.1 <i>Debris- and mud-flow propagation in FLO-2D</i> .....	38
<b>CHAPTER 3 .....</b>	<b>41</b>
STRUCTURAL VULNERABILITY .....	41
3.1 <i>State of art in hydrogeological vulnerability assessment</i> .....	41

---

3.2 <i>The general framework for hydrogeological vulnerability and risk analysis</i> .....	43
3.2.1 Performance measures and interface variables for hydrogeological risk analysis .....	43
3.2.1.1 Flood risk assessment .....	45
3.2.1.2 Debris flow risk assessment .....	46
3.2.2 Structural class and uncertainties characterization .....	46
3.2.2.1 The uncertainties in geometrical parameters .....	48
3.2.2.2 Uncertainties in material mechanical properties .....	49
3.2.2.3 The uncertainties in loading .....	49
3.2.3 Overview of the implemented Monte Carlo Simulation framework .....	50
3.2.4 Incremental analysis procedure .....	53
3.2.5 The procedure for Robust Fragility assessment .....	54
3.2.6 Probability- and performance-based safety checking .....	56
3.3 <i>Structural analysis</i> .....	58
3.3.1 Structural model .....	58
3.3.2 Statics and hydrogeological-induced actions .....	62
3.3.3 Material models .....	65
3.3.4 Safety checks .....	67
3.3.5 Limit states definition .....	71
<b>CHAPTER 4</b> .....	<b>73</b>
HYDRA: A NEW SOFTWARE FOR HYDROGEOLOGICAL RISK ANALYSIS .....	73
4.1 <i>Introduction</i> .....	73
4.2 <i>HydRA description</i> .....	75
4.3 <i>Command manual</i> .....	77
4.3.1 Input description .....	77
4.3.1.1 Analysis .....	77
4.3.1.2 Materials .....	78
4.3.1.3 Geometry .....	79
4.3.1.4 Loads .....	80
4.3.1.5 Constraints definition .....	83
4.3.1.6 Other definitions .....	83
4.3.2 Outputs description .....	83
4.3.3 Example of usage .....	86
4.3.3.1 HydRA setup .....	86
4.3.3.2 Example of implementation of a complete input file .....	87
4.3.3.3 Analysis results .....	89
<b>CHAPTER 5</b> .....	<b>93</b>
FRAMEWORK APPLICATIONS .....	93
5.1 <i>Debris flow damage incurred to a real building: an in situ back analysis</i> .....	93
5.1.1 Debris flow actions reconstruction .....	94
5.1.2 Structural model and analysis .....	95
5.1.3 Structural response and damage pattern comparison with analysis results .....	99

---



5.2 <i>Sarno: Portfolio damage analysis due to the 1998 debris flow disaster</i> .....	103
5.2.1 Debris flow actions modelling .....	103
5.2.2 Structural portfolio characterization .....	105
5.2.3 Vulnerability and risk assessment .....	107
5.3 <i>Castellammare di Stabia: risk analysis</i> .....	110
5.3.1 Characterizing debris flow and flooding actions .....	110
5.3.2 Structural portfolio characterization .....	114
5.3.3 Vulnerability and risk assessment .....	117
<b>CHAPTER 6</b> .....	<b>125</b>
CONCLUSIONS AND FINAL REMARKS .....	125
REFERENCES .....	129
LIST OF FIGURES .....	139
LIST OF TABLES .....	143

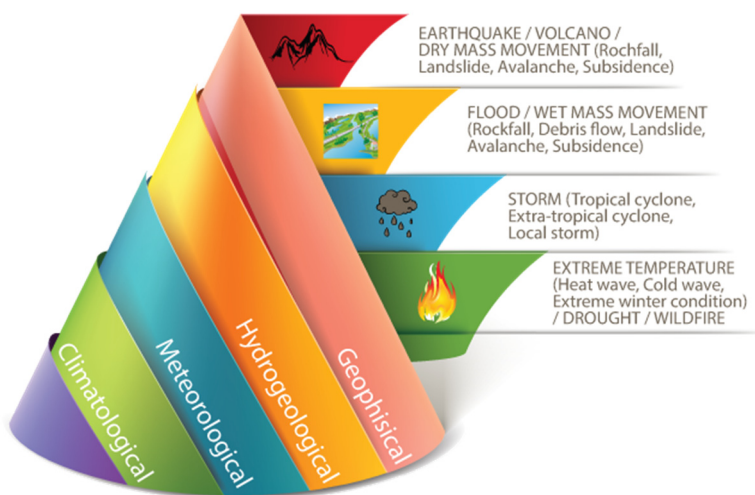


---

# Chapter 1

## Introduction

Natural disaster is a serious disruption of the functioning of a community or a society involving widespread human, material, economic or environmental losses and impacts, which exceed the ability of the affected community or society to cope using its own resources ([UNISDR 2009](#)). As reported in Tab. 1-1, natural disasters can be caused by four hazards categories, i.e. geophysical, hydrogeological, meteorological or climatological events. Between 1961 and 2010 ([Guha-Sapir and Hoyois 2012](#)), natural disasters produced a global annual average of 129.6 million victims worldwide. Around 80% of these victims affected by natural disasters were concentrated in the last decades. This is a consequence of two strictly correlated phenomena: (a) the rapid demographic growth; (b) the formation of urban settlements in disaster-prone areas often without performing adequate (if any) risk assessment of the area.



*Tab. 1-1: Natural hazards subgroup definition and classification based on ([Guha-Sapir and Hoyois 2012](#))*

In the observed period (1961-2010), around 14% of natural disasters took place in Europe. Italy is ranked at the 3<sup>rd</sup> place for number of natural disasters (101) after Russia (128) and France (126).

In the Mediterranean catchment areas, hydrogeological natural hazards can cause serious damage and economic losses. For example, an estimated 1.2 billion Euros worth of damage was caused in the 2002 Gard (France) single flash flood event ([Huet et al. 2003](#)), 65 million Euros of damage in the 2000 Magarola (Spain) flash flood ([Botija et al. 2001](#)), 300 million Euros of damage in the 1994 Pinios (Greece) flash flood ([Gaume et al. 2004](#)) and 4.6 million Euros of damage in the 2007 Mastroguglielmo (Italy) flash flood event ([Aronica et al. 2009](#)). Past flash flood and debris flow events have often caused high numbers of casualties; for example, over 80 people died in the 1996 Biescas flood in Spain ([Alcoverro et al. 1999](#)), 47 died in the flash flood on the Malá Svinka River in Slovakia in 1998, 23 were killed in the 2002 Gard flood, two died in the flash flood and debris flow event at Cable Canyon in San Bernardino County in California in 2003 ([Restrepo et al. 2009](#)) and 19 000 were killed in the Cordillera de la Costa, Vargas (Venezuela) flash flood and debris flow disaster in 1999 ([Larsen et al. 2002](#)).

Due to its geological and geomorphological structure, almost the entire Italian territory is prone to geophysical (earthquake and volcano) and hydrogeological (flood, landslide and debris flow) natural hazards. However, since the end of the second world war, the country has been subjected to rapid urbanization, often neglecting the available information about areas prone to hydrogeological risk. This resulted in a significant increase in the asset exposed to risk. About 42% of the Italian territory is susceptible to hydrogeological hazards ([Trigila et al. 2015](#)) which breaks down into 19.3% prone to landslides and 22.7% prone to floods. Moreover, it is estimated that 37.9% of the population is exposed to life-threatening risks (Fig. 1-1 and Fig. 1-2). The hydrogeological hazard is an issue of particular concern because of its impact on the population, infrastructures, communication systems, lifelines, economic and productive sectors.

## 1.1 Motivation

Hydrogeological risk analysis is inter-disciplinary and polyhedral: it requires geological, geotechnical, hydrological, hydraulic, structural engineering and probabilistic expertise. The renders the risk assessment process particularly complex and challenging.

The work presented in this thesis is developed within the Italian research project METROPOLIS funded by the National Operative Program (PON 03PE\_00093\_4) and focused on the study of the integrated and sustainable methods and technologies for resilience and safety of urban systems. The project aims at defining the methodology and at developing innovative and sustainable technologies for the evaluation and management of the natural and anthropic risks for urban system, in order to address mitigation strategies

based on integrated decision support system.

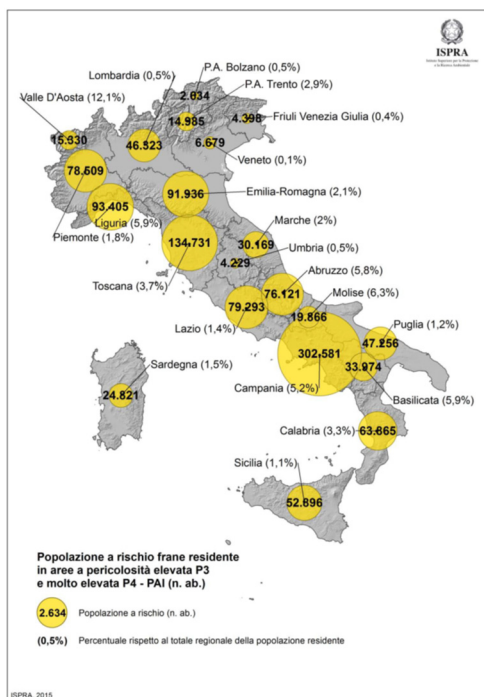


Fig. 1-1: Inhabitants of highly landslide prone areas in Italian regions (Trigila et al. 2015).

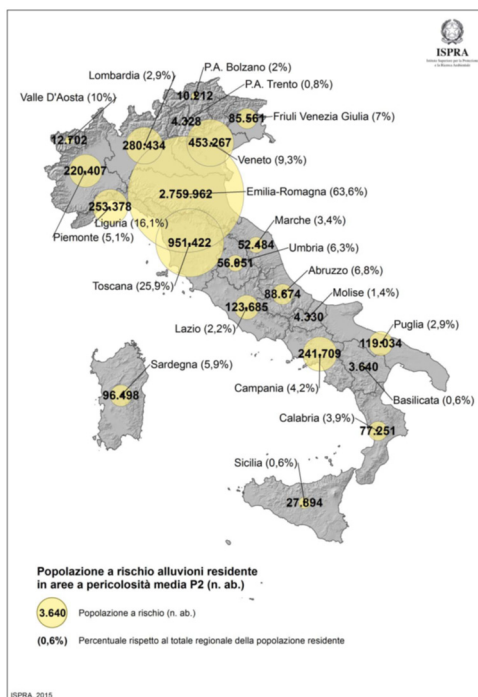


Fig. 1-2: Inhabitants of highly flood prone areas in Italian regions (Trigila et al. 2015).

The innovative approach adopted by METROPOLIS project consists in defining integrated risk assessment procedures, taking into account several hazard sources and several subsystems composing the urban system, considering interaction of phenomena due to intra/inter functional links between the components and subsystems.

This thesis is focused on two specific tasks within the METROPOLIS project, i.e. the “Structural vulnerability assessment for the hydrogeological hazard” (task 3.1.2) and “Vulnerability assessment for the hydrogeological hazard for a class of buildings” (task 3.2.2). The first task regards the study of the vulnerability of single buildings (considered as physical components of the urban system) subjected to hydrogeological hazard. The second one, instead, regards the analytical vulnerability and risk assessment of a class of buildings subjected to hydrogeological hazard.

## 1.2 Objectives and products

The focus of this work is on spatial vulnerability and risk assessment for a portfolio of buildings, subjected to rapid hydrogeological phenomena. The present work has the following main objectives:

1. Elaboration of a general probability-based methodology for the analytical assessment

- of the vulnerability of portfolio of building. This methodology consists in defining: (a) the intensity measure the engineering demand parameter(s) and the performance variable for the structural analysis; (b) the structural models and the analysis type; (c) the limit states; (d) the uncertainty propagation model.
2. Development of a Java software able to assess the structural vulnerability and risk, according to the following steps: (a) propagation of the uncertainties, considering risk assessment both for a single building and also a portfolio of buildings, using a simulation based approach; (b) structural analysis; (c) evaluation of the structural fragility adopting an efficient and simulation-based method which gives the so-called “robust” fragility curve and an associated plus/minus one-standard deviation interval; (d) integration of the risk, expressed in different metrics.
  3. Calculation of the class fragility curves for a real portfolio of buildings located in Castellammare di Stabia (one of the case study cities in the province of Naples, Italy) located in an area highly susceptible to rapid hydrogeological phenomena.
  4. Realization of hydrogeological risk maps for the city of Castellammare di Stabia.

### 1.3 Organization and outline

A modular approach has been adopted in the writing of this thesis in order to facilitate a clear presentation of the different aspects of this work. After a brief introduction and the general definitions, the risk assessment procedure is analysed and explained in detail -- describing all the hypotheses, the assumptions and the scope of the research.

The thesis is organized in six chapters that trace the flow chart reported in Fig. 1-3.

In Chapter 1 a brief introduction, motivations, objectives, outline, all the general definitions, basic concepts, the performance-based risk assessment approach and the description of the case studies are presented.

In Chapter 2 hazard evaluation for the rainfall-induced phenomena is discussed with specific focus on flood and debris flow. The hazard assessment procedure is described from the point of view of its implementation in the risk assessment procedure.

In Chapter 3 the aspects related to structural vulnerability assessment for a single building and for a class of buildings are described. The chapter carefully lays out concepts such as propagation of uncertainties with a simulation-based approach, robust structural fragility assessment, definition of limit states, structural model, performance variable, loading and structural analysis.

In Chapter 4 the software platform HydRA (**H**ydrogeological **R**isk **A**nalysis) is presented. It is important to note that all the methodological aspects discussed in Chapter 3 are implemented in the platform.

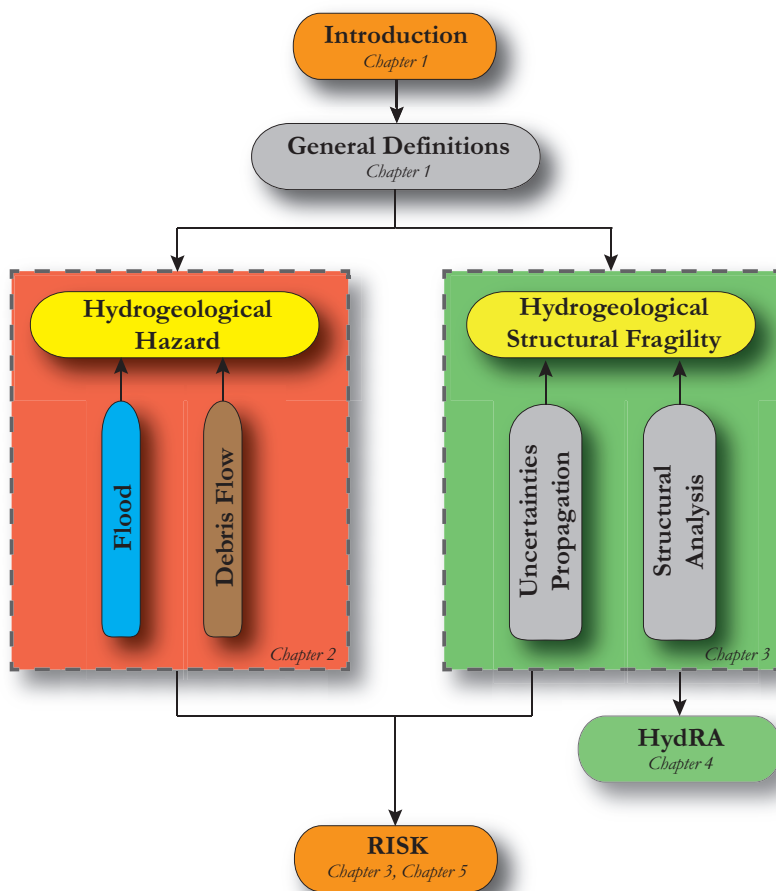


Fig. 1-3: Contents flow chart.

In Chapter 5 the methodology and the proposed software platform have been applied in order to validate the framework for two past events: a masonry building damaged in the Scaletta Zanclea flash flood event, 2009 (Messina, Italy); a portfolio of buildings in the Episcopio neighbourhood, Sarno (Salerno, Italy) affected by the debris flow event, 1998. Finally, a comprehensive hydrogeological risk analysis has been performed on the buildings, susceptible to flooding and debris flow, located in the historical centre of Castellammare di Stabia (Napoli, Italy).

In Chapter 6 the main conclusions and the final remarks are summarized.

## 1.4 Basic definitions

In order to simplify the comprehension of this work and to ensure a correct transfer of information, a list of basic definitions used in the work is proposed in this paragraph. The following terms make reference to the conventional *terminology in disaster and risk reduction* proposed by [UNISDR \(2009\)](#) with some integrations reported by [Marzocchi et al. \(2012\)](#).

- **Damage.** The amount of destruction, either in health, financial, environmental functional and/or other terms as a consequence of an occurred hazard; its value can be obtained by convoluting the value at risk (or exposed value) by the vulnerability.
- **Disaster.** A serious disruption of the functioning of a community or a society involving widespread human, material, economic or environmental losses and impacts, which exceeds the ability of the affected community or society to cope using its own resources.
- **Event.** Anything produced by a risk source in a certain area that can generate phenomena with potentially adverse consequences. The adverse event can be due to a risk source located inside or outside the site where the event takes place.
- **Exposure.** People, property, systems, or other elements present in hazard zones that are thereby subjected to potential losses. Measures of exposure can include the number of people or types of assets in an area. These can be combined with the specific vulnerability of the exposed elements to any particular hazard to estimate the quantitative risks associated with that hazard in the area of interest.
- **Hazard.** A dangerous phenomenon, substance, human activity or condition that may cause loss of life, injury or other health impacts, property damage, loss of livelihoods and services, social and economic disruption, or environmental damage.
- **Loss.** It measures the total potential loss due to an adverse event in a given area. It can be expressed in human casualties, either in economic or conventional terms (since it is difficult to express heritage or environmental losses monetarily). It depends on the various activities (human, cultural, economic) as well as on the environmental characteristics of the referred area.
- **Risk assessment.** A methodology to determine the nature and extent of risk by analysing potential hazards and evaluating existing conditions of vulnerability that together could potentially harm exposed people, property, services, livelihoods and the environment on which they depend.
- **Risk.** the combination of the consequences of an event (damage) and the associated probability of its occurrence (probabilistic hazard); it may be understood as the expected loss due to a particular hazard for a given area and reference period. In some cases, (e.g., when the exposed value is not explicitly considered), risk is understood as the probability (or rate) that a negative consequence (e.g. loss) can occur in a given period of time following a specific adverse event. Analytically it is the convolution of hazard, vulnerability and exposure.
- **Scenario.** A representation of one or more linked adverse events causing and/or caused by threatening phenomena. Several scenarios can be identified for each adverse event.
- **Vulnerability.** The characteristics and circumstances of a community, system or asset that make it susceptible to the damaging effects of a hazard. There are many aspects



of vulnerability, arising from various physical, social, economic, and environmental factors. Examples may include poor design and construction of buildings, inadequate protection of assets, lack of public information and awareness, limited official recognition of risks and preparedness measures, and disregard for wise environmental management. Vulnerability varies significantly within a community and over time. This definition identifies vulnerability as a characteristic of the element of interest (community, system or asset) which is independent of its exposure. However, in common use the word is often used more broadly to include the element's exposure.

### 1.5 Performance-based framework

The methodology used in this work follows the principles proposed by [Cornell and Krawinkler \(2000\)](#) who founded the Performance Based Earthquake Engineering (PBEE) framework. The approach is synthesized in the general formulation written in Eq. 1-1:

$$\lambda(DV) = \int \int \int P[DV > dv | DM] \cdot f_{DM|EDP}[dm] \cdot f_{EDP|IM}[edp] \cdot d(edp) \cdot d(dm) \cdot |d\lambda_{IM}| \quad 1-1$$

$\lambda(DV)$  is a risk metric and represents the mean annual frequency of the Decision Variable (DV) exceeding a specific value. For instance, it can be the mean annual frequency that the direct economic loss is larger than a certain percentage of the replacement cost. The exposure term  $P[DV > dv | DM]$  is the probability that the decision variable  $DV$  is larger than a certain value  $dv$  given a specific damage measure  $DM$ . The fragility term  $f_{DM|EDP}[dm]$  is the probability density function (PDF) for the damage measure (DM) given a known value of the engineering demand parameter (EDP). The fragility term  $f_{EDP|IM}[edp]$  is the probability density function (PDF) for the engineering demand parameter (EDP) given a known value of the intensity measure (IM). The hazard term  $|d\lambda_{IM}|$  is the absolute value of the increment of the rate of having an intensity measure (IM) greater than a certain level.

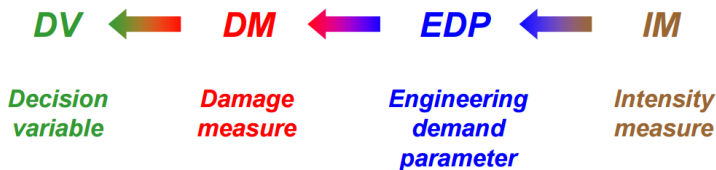


Fig. 1-4: Relation between the four generic variables of performance based framework.

The four generic variables involved in Eq. 1-1 have been described in detail by [Deierlein et al. \(2003\)](#) in the context of performance-based earthquake engineering. Starting from the general definitions, these generic variables are defined in the following in the context of hydrogeological risk assessment.

**Intensity measure (IM)** is a scalar or a vector of parameters that describes the intensity of the hydrogeological phenomenon of interest. The  $IMs$  need to respect four conditions: efficiency (the EDP given IM should have a small conditional variance); scaling robustness (the higher  $IMs$  values should correspond to higher magnitudes of the hydrogeological event); hazard computability (it should be possible to obtain a hazard curve in terms of  $IMs$ ); sufficiency (the EDP given IM should be independent of other characteristics of the hydrogeological phenomenon). In the case of rainfall induced phenomena, possible  $IMs$  can be: the flow height  $H$ , the flow velocity  $V$  or the vector  $[H, V]$ .

**Engineering demand parameters (EDPs)**, which are calculated analytically through structural analysis, are quantities that describe the local and/or global response of the structure. In this work, the structure response is described in terms of various stress components.

**Damage measures (DMs)** are discrete variables that represent the structural damage state.

**Decision variables (DVs).** In the PBEE approach, the decision variables are generally linked to the losses incurred in a structure taking into account casualties/fatalities, repair costs, downtime, and replacement and recycling/disposal costs.

In this work, the risk is evaluated as the mean annual frequency of exceeding a specific limit state  $LS$ . It is possible to rewrite the Eq. 1-1 in a more specific and concise manner for the scope of this work (Eq. 1-2):

$$\lambda_{LS} = \int_{IM} P[LS | IM] \cdot |d\lambda_{IM}| \quad 1-2$$

where:  $\lambda_{LS}$  is the mean annual frequency of exceeding the given limit state  $LS$  ( $DV=LS$ );  $IM$  is the chosen intensity measure for the hydrogeological hazard (the height of the flow  $H$  or the velocity of the flow  $V$  or the vector  $[H, V]$ );  $P[LS | IM]$  is the fragility term and is expressed as the probability of exceeding the limit state  $LS$  given  $IM$ ;  $\lambda_{IM}$  is the hazard expressed in terms of the mean annual frequency of exceeding a given  $IM$  level. It should be noted that in Eq. 1-2 the decision variable DV is directly conditioned in the intensity measure (IM). The adopted performance-based probabilistic framework is described in more detail in Chapter 3.

In order to express the risk not only as a rate but also in terms of annual probability of exceeding a given limit state, it is possible to assume that the hydrogeological phenomena is modelled as a homogenous Poisson process with the rate equal to  $\lambda_{LS}$ . Under such hypothesis, it is possible to express the risk as reported in the Eq. 1-3 where  $P[LS]$  is the (first-excursion) probability of exceeding the limit state LS in one year.

$$P[LS]=1-\exp(-\lambda_{LS})$$

## 1.6 The case studies

In this section, a brief description of the case studies considered in the work is reported. As it is shown in Fig. 1-5, the case studies are located in the south of Italy: (1) a two-storey masonry building in Scaletta Zanclea (Messina, Sicilia region); (2) The buildings in the Episcopio neighbourhood, Sarno (Salerno, Campania region); (3) two portfolios of buildings located in the centre of the city of Castellammare di Stabia (Naples, Campania region).

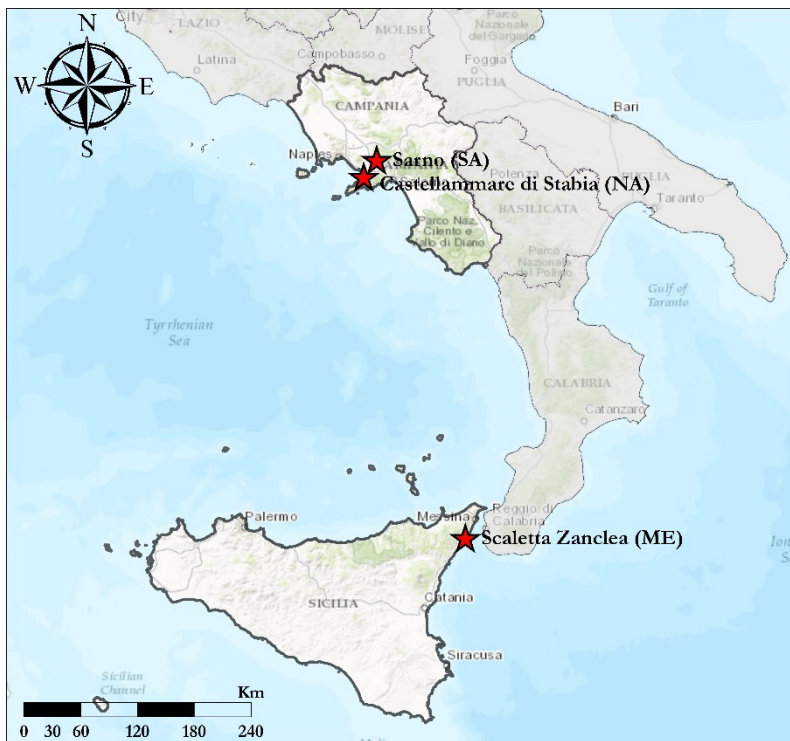


*Fig. 1-5: Localization of the case studies.*

### 1.6.1 Masonry building in Scaletta Zanclea

The small village of Scaletta Zanclea is located on the Ionic Coast of the northeastern part of Sicily, 20 km far from the southeastern side of the city of Messina. The village is crossed by the Racinazzi torrent, which has a catchment area of approximately 1.6 km<sup>2</sup>, with elevations that range between 0 and 790 m a.s.l, with an average value of 384 m a.s.l. The topography is very rugged and the slope is steep (with an average value of 0.18%). The main channel is long about 3.3 km and it receives some tributaries canalized into narrow pathways, as they approach the main channel, and characterized by the same morphology

of the main torrent.

The catchment is predominantly rural, with grassland and crop cultivation (46%) and shrubs and sparse forests (42.4%) in the upper mountainous part, while the areas in the valley floor (7.3%) are highly urbanized. Moreover, several slopes formed due to past local or global instability processes, and the stability conditions of the shallowest portions of most of the rock slopes are, in some cases, unsatisfactory due to the poor geotechnical properties of the cover soils.

The climate is typically Mediterranean, with rainfall events (mainly convective) characterised by short durations and high intensities during the wet season (October – April), and very few events during the dry season (May – September). The mean annual rainfall height is about 970 mm, with around 84% occurring in the wet season and 16% in the dry season.

In the afternoon of 1st October, 2009, a deep cyclone developed in the southern part of the Mediterranean basin, producing an intense rainstorm over Sicily that particularly affected the area of Messina. The flash flood and debris flow triggered by the consequent heavy rainfall locally involved properties, buildings, roads and bridges, and blocked the traffic for many hours. A total of 38 people died and damage close to 550 millions of Euros was estimated (Regional Department of Civil Protection for Sicily, 2009).

During the late evening, the village of Scaletta Zanclea was hit by a large debris flow coming from the Racinazzi torrent, and this caused the collapse of some buildings and casualties. The A/18 Messina-Catania motorway, the state road 114 and the Giampileri-Scaletta rail line were closed off due to the landslides.

Rainfall maps ([Aronica et al. 2010](#)) show how the storm covered the southern part of the city of Messina and was concentrated on the Ionic sea coast, mainly in the area around Giampileri and Scaletta Zanclea. The event developed in few hours: more than 220 mm of rain fell in less than four hours, with a peak of about 120 mm/hr in 10 minutes.

The structure that is the object of the present analysis is situated in the town of Scaletta-Zanclea, near to Messina, on the SS114 "Consolare Valeria" road, right next to the Racinazzi torrent (Fig. 1-6).

This building was built at the end of 1800 and was restored after the 1908 Messina earthquake. It is composed of two levels: an intermediate RC slab and a wooden tiles roof. The structure is constituted of irregular masonry with fractured stones and small/medium size bricks (Fig. 1-7). This type of masonry was very common in the Messina area in the past. In the 1950s, the existing masonry was replaced by bricks.

The structure was seriously damaged during the event of October 2009. The northern wall in the principal façade (in front of the "Consolare Valeria" road) presents the major damage in correspondence of the corner with the eastern wall, the upper-right corner of the

left door and the right side of the middle door. The wall that is positioned parallel to the Racinazzi torrent also suffered major damage which affected the wall panel to the left of the window in the corner with the northern wall. Moreover, a small, dependent structure on this side of the building was completely swept away by the debris flow. All the doors were carried away by the mud that invaded the ground floor. The balconies of the first level and the parapets were broken, and the building is still uninhabited.

The choice of this building as case study is motivated by the following considerations: (1) the major damage caused to the building due to the 2009 flash flood event; (2) it represents a typical 19th century masonry building; (3) the large availability of in situ test results on material mechanical properties for wall panels made of similar materials; and (4) the availability of documentation concerning the structural layout.

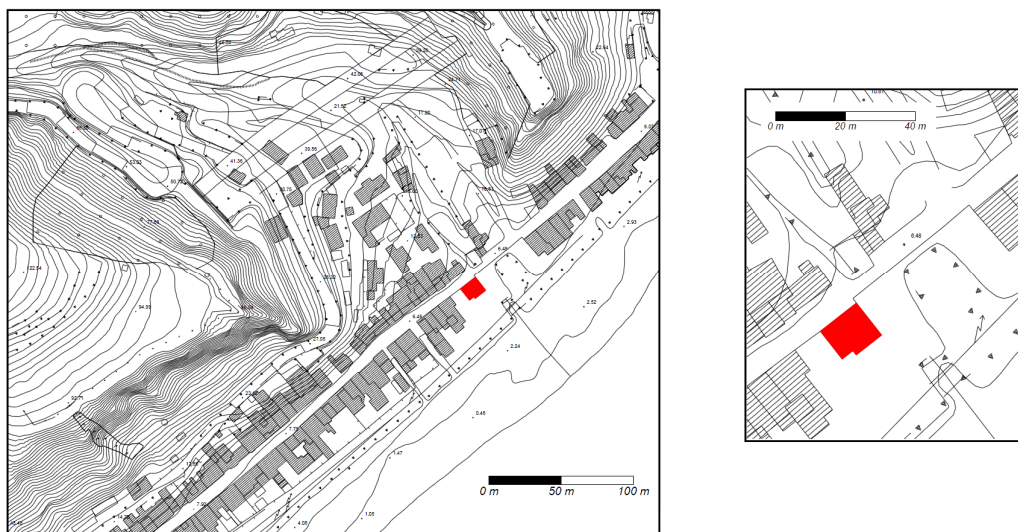


*Fig. 1-6: Localization of the case study building (Jalayer et al. 2016).*



*Fig. 1-7: Case-study building before and after the event of October 2009.*

## 1.6.2 Portfolio of buildings in Sarno

Between the 5<sup>th</sup> and 6<sup>th</sup> of May in 1998, a huge landslide event affected the urban areas of Sarno (SA), Quindici (AV), Siano (SA), Bracigliano (SA) and San Felice a Cancellò (CE) in the southern of Italy, causing 159 deaths. 137 people died in the Episcopio neighbourhood of the city of Sarno. On 5<sup>th</sup>-6<sup>th</sup> May, in a 48 hours period, more than one hundred slope instability phenomena occurred along the slopes illustrated in Fig. 1-8. A rainfall height equal to 120mm was measured by the rain gauges located at the toe of the Pizzo d'Alvano massif, 240m a.s.l. (Cascini et al. 2008). A total debris volume of about 2,000,000 m<sup>3</sup> was displaced, 40% of which consisted of eroded materials along the channels. The debris covered distances ranging from a few hundred meters up to distances larger than 2 km with velocities estimated to be in the range of about 5-20 m/s (Faella and Nigro 2003).

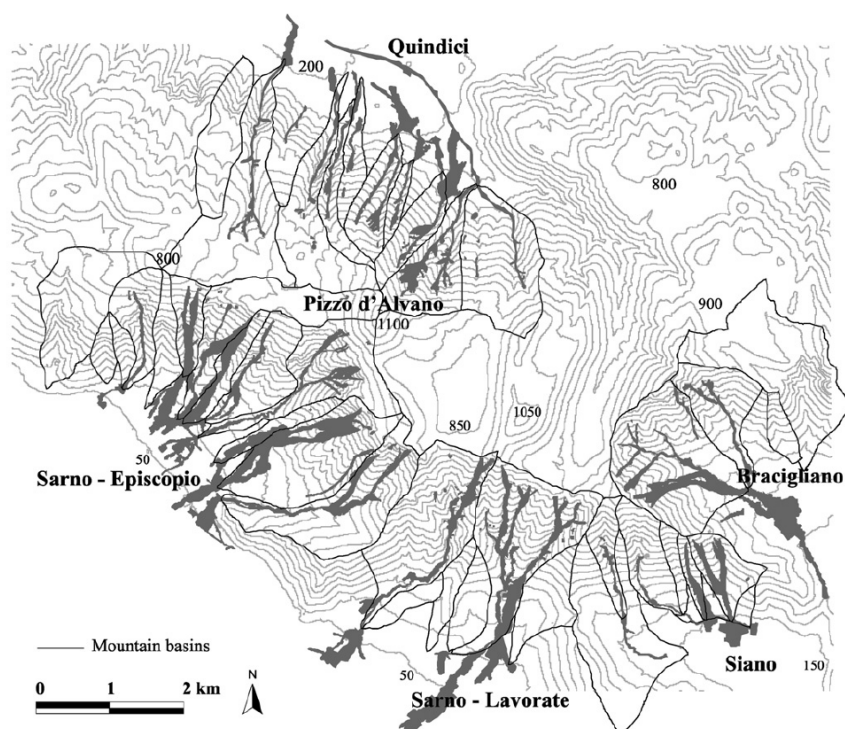


Fig. 1-8: Overview of the main flow-like mass movements in May 1998 (Cascini et al. 2008).

Episcopio district was one of the most affected in terms of both casualties and the incurred damaged to the buildings. Fig. 1-9 illustrates the observed damage of the buildings inside located the footprint of the event (Zanchetta et al. 2004).

Many scientists have studies the Sarno disaster from various points of view. Sarno event has been chosen as a case study in this work in order to validate the methods proposed herein by comparing the analytical results with the observed damage occurred to the buildings.

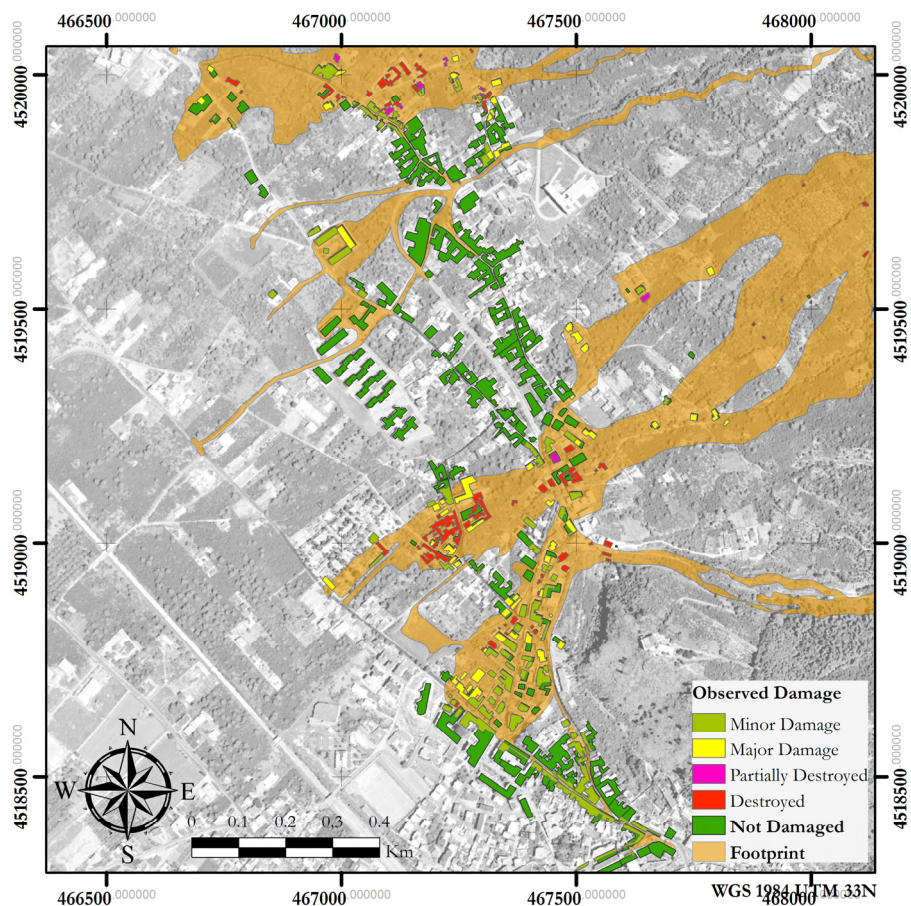


Fig. 1-9: Portfolio of affected buildings in Episcopio district (Zanchetta et al. 2004)

### 1.6.3 Portfolio of buildings in Castellammare di Stabia

The Sorrento peninsula, which divides the Gulf of Naples from the Gulf of Salerno is one of the most landslide-susceptible areas in the Campania region. Numerous debris flow events have been triggered in the peninsula, affecting several districts and leading to many casualties. Castellammare di Stabia is one of the principal landslide-susceptible areas within the peninsula and has been subjected to many debris flow events in the past. A list of the events that have affected Castellammare di Stabia are reported in Tab. 1-2 (Calcaterra et al. 2003; Calcaterra and Santo 2004; Di Crescenzo and Santo 1999).

As it is shown in Tab. 1-2, Castellammare di Stabia is highly prone to debris flow events. However, due its geo-morphological position, it can be also susceptible to flooding. Fig. 1-10 shows the delineation of the footprints of eventual debris flow and flooding phenomena.

Date	Affected cities
31 <sup>th</sup> August 1931	Castellammare di Stabia
20 <sup>th</sup> August 1935	Gragnano – Castellammare di Stabia
25 <sup>th</sup> December 1950	Castellammare di Stabia – Pozzano
17 <sup>th</sup> February 1963	Gragnano – Pimonte - Castellammare di Stabia
14 <sup>th</sup> April 1967	Castellammare di Stabia - Pozzano
22 <sup>th</sup> February 1986	Castellammare di Stabia – Vico Equense
23 <sup>th</sup> February 1987	Gragnano - Castellammare di Stabia
10 <sup>th</sup> January 1997	Gragnano - Castellammare di Stabia – Corbara – Pagani – Pimonte – S. Egidio del Monte Albino

Tab. 1-2: Debris flow events in Castellammare di Stabia in the last 100 years.

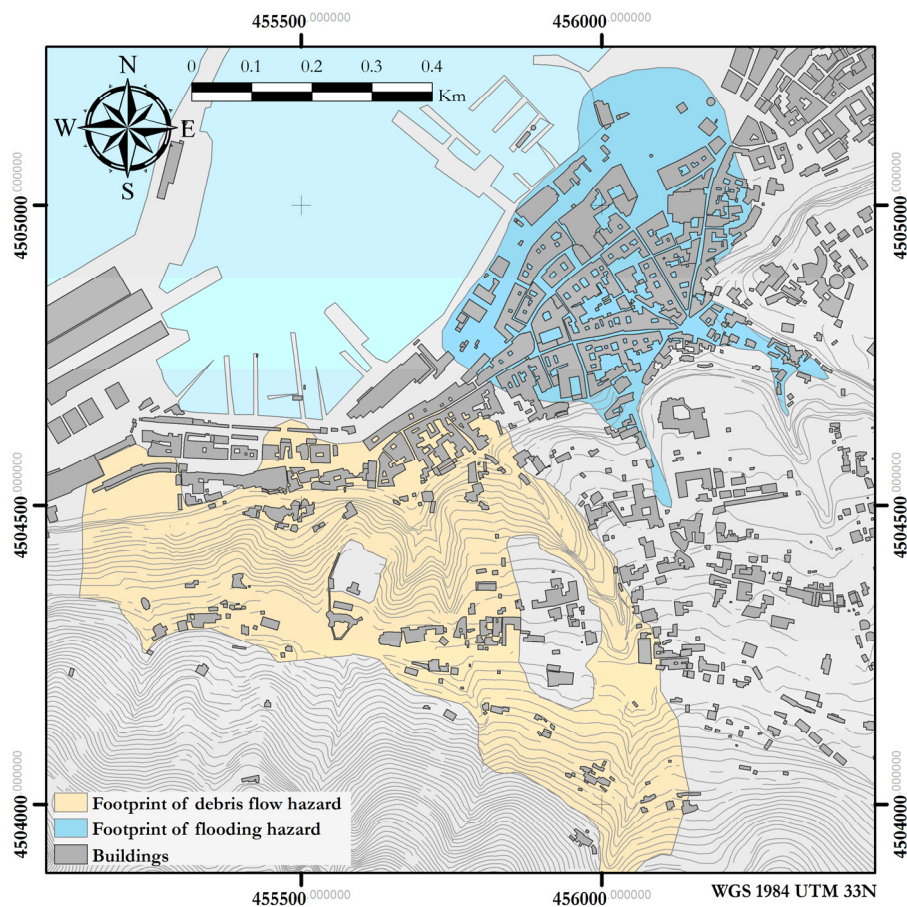


Fig. 1-10: Portfolio of buildings considered in Castellammare di Stabia.

Castellammare di Stabia has been chosen herein as a case-study for hydrogeological risk analysis.



---

# Chapter 2

## Hydrogeological hazard

*This chapter provides a brief overview of the state of the art in hydrogeological hazard assessment. The chapter is divided in three main parts: (1) landslide hazard assessment; (2) flood hazard assessment; (3) a bi-dimensional propagation model for both landslide and flooding.*

### 2.1 Landslide hazard assessment

#### 2.1.1 Overview

Landslide is the “movement of a mass composed by rocks, soil, water and debris along a slope”. Landslides are a widespread phenomenon in Italy and they have an important impact on the socio-economical system. Landslides are classified on the basis of different characteristics such as duration and frequency of occurrence of the movement, type and cause of the movement, the mechanical properties of the material involved, detachment or sliding area. A representation of landslide types, proposed by [Highland \(2004\)](#), is reported in Fig. 2-1. The classification is based on the type of movement and the type of transported material. Another interesting classification of landslides is the one proposed by [Cruden and Varnes \(1996\)](#) based on correlation between the flow velocity and the damage incurred (Fig. 2-2).

#### 2.1.2 Debris- and mud-flow

Debris flows, mudslides, mudflows or debris avalanches, are fast slope movements that generally occur during intense meteorological phenomena involving saturated soils (U.S. Geological Survey). Typically, small slips “soil slumps” arise on very steep slopes and evolve up to reach speeds of 15-20 m/s. Similar to landslides, debris flows are characterized by high speed, no visible warning signs. The debris flows can transport and deposit material up to several kilometres.

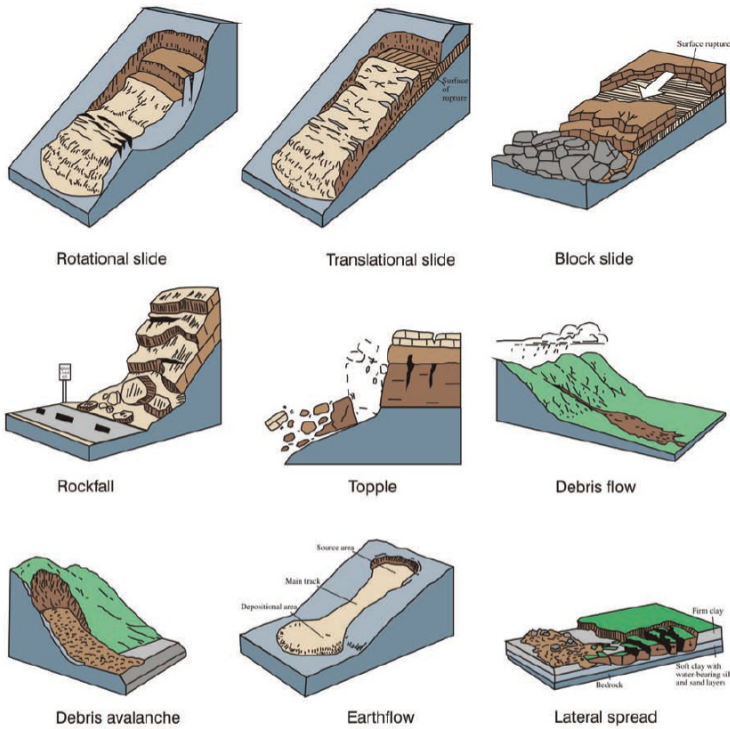


Fig. 2-1: Types of landslides (*Highland 2004*)

Velocity Class	Description	Velocity (mm/sec)	Typical Velocity	Probable Destructive Significance
7	Extremely Rapid	$5 \times 10^3$	5 m/sec	Catastrophe of major violence; buildings destroyed by impact of displaced material; many deaths; escape unlikely
6	Very Rapid	$5 \times 10^1$	3 m/min	Some lives lost; velocity too great to permit all persons to escape
5	Rapid	$5 \times 10^{-1}$	1.8 m/hr	Escape evacuation possible; structures, possessions, and equipment destroyed
4	Moderate	$5 \times 10^{-3}$	13 m/month	Some temporary and insensitive structures can be temporarily maintained
3	Slow	$5 \times 10^{-5}$	1.6 m/year	Remedial construction can be undertaken during movement; insensitive structures can be maintained with frequent maintenance work if total movement is not large during a particular acceleration phase
2	Very Slow	$5 \times 10^{-7}$	15 mm/year	Some permanent structures undamaged by movement
	Extremely SLOW			Imperceptible without instruments; construction POSSIBLE WITH PRECAUTIONS

Fig. 2-2: Landslide rate of movement (velocity) classification taken from *Cruden and Varnes (1996)*.

In literature, the debris flows are classified according to various parameters such as the speed, the granulometric composition, the trigger mechanism, the duration, magnitude, etc. [Coussot and Meunier \(1996\)](#) created a ranking as a function of type (e.g., cohesive or granular) and the solid versus liquid proportions of the transported material (considering also the floating objects). [Ancely \(2001\)](#) classifies these phenomena, as a function of their mechanical behaviour, in three classes: (a) muddy debris flow, characterized by visco-plastic behaviour, due to a wide particle size range and a good percentage of clay materials; (b) granular debris flows, in which the particle size distribution is wide, with lower amounts of fine-grained material than muddy debris flow (class a); (c) lahar debris flows: the particle size distribution is narrow with a limited percentage of fine-grained material. The mass behaviour is expected to be frictional/viscous and modest slopes are enough to produce the mass flow. A synthesis of the classification proposed by [NRC \(1982\)](#) based on the sediment concentration is reported in Fig. 2-3.

	Sediment Concentration		Flow Characteristics
	by Volume	by Weight	
Landslide	0.65 - 0.80	0.83 - 0.91	Will not flow; failure by block sliding
	0.55 - 0.65	0.76 - 0.83	Block sliding failure with internal deformation during the slide; slow creep prior to failure
Mudflow	0.48 - 0.55	0.72 - 0.76	Flow evident; slow creep sustained mudflow; plastic deformation under its own weight; cohesive; will not spread on level surface
	0.45 - 0.48	0.69 - 0.72	Flow spreading on level surface; cohesive flow; some mixing
Mud Flood	0.40 - 0.45	0.65 - 0.69	Flow mixes easily; shows fluid properties in deformation; spreads on horizontal surface but maintains an inclined fluid surface; large particle (boulder) setting; waves appear but dissipate rapidly
	0.35 - 0.40	0.59 - 0.65	Marked settling of gravels and cobbles; spreading nearly complete on horizontal surface; liquid surface with two fluid phases appears; waves travel on surface
	0.30 - 0.35	0.54 - 0.59	Separation of water on surface; waves travel easily; most sand and gravel has settled out and moves as bedload
	0.20 - 0.30	0.41 - 0.54	Distinct wave action; fluid surface; all particles resting on bed in quiescent fluid condition
Water Flood	< 0.20	< 0.41	Water flood with conventional suspended load and bedload

*Fig. 2-3: flow classification as a function of sediment concentration (NRC 1982).*

The evolutionary stages of a debris flow can be identified as: trigger, propagation and deposit. The beginning of debris flow is caused by the presence of triggering and the presence of other predisposing factors among which the most important is represented by

the geotechnical characteristics of the slope. In fact, the shear strength of the material is the key parameter that is involved in assessment of the stability of a slope. At the same time, the weather-related conditions play an important role. In fact, a theme of great relevance in the scientific community is the definition of rainfall trigger thresholds. [Guadagno \(1991\)](#) and [Calcaterra et al. \(2000\)](#), with specific reference to the event of Sarno 1998, demonstrated that the problem of the rainfall thresholds can be evaluated empirically, by proposing different calibrations of the intensity-duration threshold relation ([Caine 1980](#)). These relations solve the problem of triggering subjected to a series of assumptions: the effect of the rainfall events preceding the triggering event are not considered; parameters defining the soil condition are not taken into account.

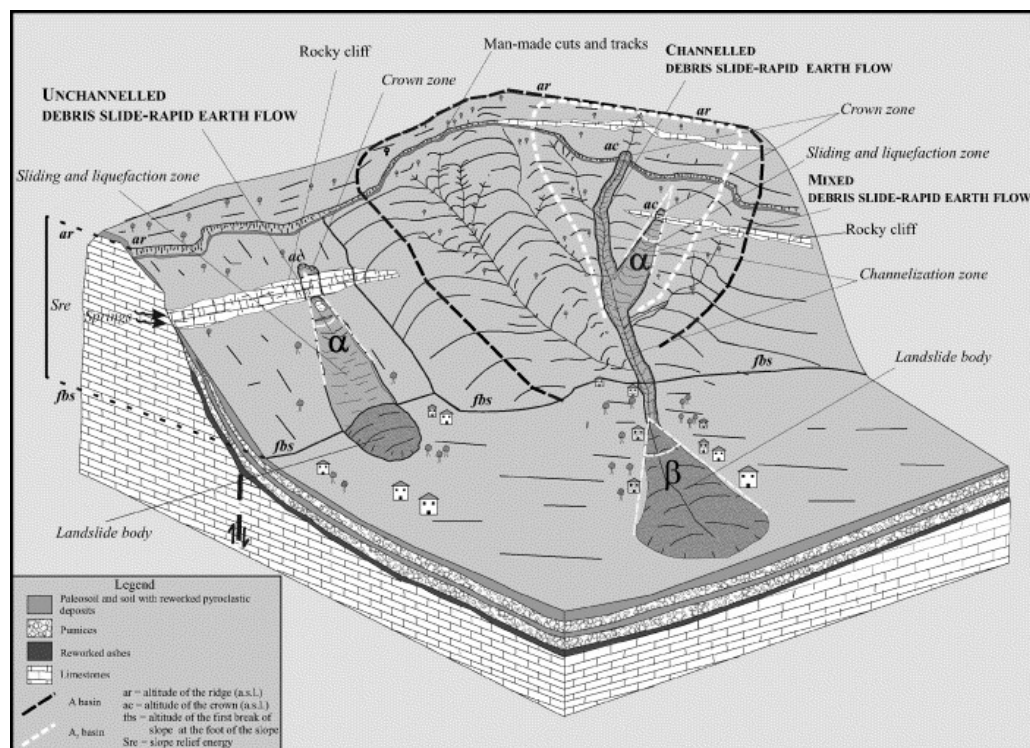


Fig. 2-4: Main morphological parameters of a debris flow ([Di Crescenzo and Santo 2005](#)).

Regarding the propagation, it is possible to divide the debris flow in channelled and un-channelled debris flow (Fig. 2-4). The channelled debris flow events are characterized by high speed and density and their propagation is strongly conditioned by more-or-less deep impluvia paths, where it is possible to observe high increase in the transported volume. The un-channelled debris flow events are flow slides involving slopes devoid of watersheds and they are characterized by a pseudo-triangular shape and by lower speeds compared to channelled debris flow events.

The final evolutionary stage of a debris flow is the deposit. It depends on the decreasing

slope, the end of the channels in the deposit area, the loss of speed, and the presence of large debris in the flow front. Of great importance is also the loss of water contained in the debris flow; this causes a variation in the rheological characteristics of the material causing the flow stand still.

An important parameter for comparing different debris flow phenomena is the magnitude of the event. It is defined as the volume moved during the phenomenon and it is generally defined as a function of the peak flow discharge. A useful classification of the debris flow magnitude class linked to the mobilized volumes, peak discharge and potential consequences is proposed by [Jakob \(2005\)](#) and is summarized in Fig. 2-5

Size class	$V$ , range (m <sup>3</sup> )	$Q_b$ , range (m <sup>3</sup> /s)	$Q_v$ , range (m <sup>3</sup> /s)	$B_b$ (m <sup>2</sup> )	$B_v$ (m <sup>2</sup> )	Potential consequences
1	<10 <sup>2</sup>	<5	<1	<4×10 <sup>2</sup>	<4×10 <sup>3</sup>	Very localized damage, known to have killed forestry workers in small gullies, damage small buildings
2	10 <sup>2</sup> –10 <sup>3</sup>	5–30	1–3	4×10 <sup>2</sup> –2×10 <sup>3</sup>	4×10 <sup>3</sup> –2×10 <sup>4</sup>	Could bury cars, destroy a small wooden building, break trees, block culverts, derail trains
3	10 <sup>3</sup> –10 <sup>4</sup>	30–200	3–30	2×10 <sup>3</sup> –9×10 <sup>3</sup>	2×10 <sup>4</sup> –9×10 <sup>4</sup>	Could destroy larger buildings, damage concrete bridge piers, block or damage highways and pipelines
4	10 <sup>4</sup> –10 <sup>5</sup>	200–1500	30–300	9×10 <sup>3</sup> –4×10 <sup>4</sup>	9×10 <sup>4</sup> –4×10 <sup>5</sup>	Could destroy parts of villages, destroy sections of infrastructure corridors, bridges, could block creeks
5	10 <sup>5</sup> –10 <sup>6</sup>	1500–12,000	300–3×10 <sup>3</sup>	4×10 <sup>4</sup> –2×10 <sup>5</sup>	4×10 <sup>5</sup> –2×10 <sup>6</sup>	Could destroy parts of towns, destroy forests of 2 km <sup>2</sup> in area, block creeks and small rivers
6	10 <sup>5</sup> –10 <sup>6</sup>	N/A	3×10 <sup>3</sup> –3×10 <sup>4</sup>	>2×10 <sup>5</sup>	2×10 <sup>6</sup> –3×10 <sup>7</sup>	Could destroy towns, obliterate valleys or fans up to several tens of km <sup>2</sup> in size, dam rivers
7	10 <sup>6</sup> –10 <sup>7</sup>	N/A	3×10 <sup>4</sup> –3×10 <sup>5</sup>	N/A	3×10 <sup>7</sup> –3×10 <sup>8</sup>	Could destroy parts of cities, obliterate valleys or fans up to several tens of km <sup>2</sup> in size, dam large rivers
8	10 <sup>7</sup> –10 <sup>8</sup>	N/A	3×10 <sup>5</sup> –3×10 <sup>6</sup>	N/A	3×10 <sup>8</sup> –3×10 <sup>9</sup>	Could destroy cities, inundate large valleys up to 100 km <sup>2</sup> in size, dam large rivers
9	10 <sup>8</sup> –10 <sup>9</sup>	N/A	3×10 <sup>6</sup> –3×10 <sup>7</sup>	N/A	3×10 <sup>9</sup> –3×10 <sup>10</sup>	Vast and complete destruction over hundreds of km <sup>2</sup>
10	>10 <sup>9</sup>	N/A	3×10 <sup>7</sup> –3×10 <sup>8</sup>	N/A	>3×10 <sup>10</sup>	Vast and complete destruction over hundreds of km <sup>2</sup>

$V$  is the total volume,  $Q_b$  and  $Q_v$  are the peak discharge for bouldery and volcanic debris flows, respectively,  $B_b$  and  $B_v$  are the area inundated by bouldery and volcanic debris flows. N/A signifies that bouldery debris flows of this magnitude have not been observed.

*Fig. 2-5: Size classification for debris flow (Jakob 2005).*

### 2.1.3 Debris flow peak discharge estimation

The methodology explained in this section provides a closed form solution for modelling the uncertainties and performing a probabilistic assessment of the debris flow peak discharge ([De Paola et al. 2015](#)). This methodology is used later on for the evaluation of the debris flow peak discharge for the presented case studies.

The trigger model used in this work is based on the runoff capacity of sediments on channelled rock walls. The debris flow descending from the rocky walls may be calculated either by using a hydrological model or by defining a triangular hydrograph identified by the peak flow discharge and the duration of the event (measured from the triggering instant). [Gregoretti and Fontana \(2008\)](#) proposed a trigger model for a debris flow, comparing the critical runoff that triggers a debris flow with the peak flow value. The relation presented by the authors to obtain the critical discharge is expressed as:

$$q_{crit} = 0.78 \cdot d_M^{1.5} \cdot \tan \mathcal{G}^{1.27} \quad 2-1$$

where  $q_{crit}$  is the critical discharge per linear meter;  $d_M$  is the average dimension of the sediments;  $\mathcal{G}$  is the slope angle. The trigger of debris flow occurs if the expected water discharge  $Q_R$  is larger than  $Q_{crit} = q_{crit} \cdot B$  where  $B$  is the channel width.

Based on the hypothesis of constant volumetric concentration of the sediments and neglecting the velocity variation due to the influence of the dragged debris, it is possible to calculate the debris flow discharge  $Q_T$  as a function of water discharge  $Q_R$ :

$$Q_T = \frac{V_T}{V_R} \cdot Q_R \quad 2-2$$

Where  $V_T$  and  $V_R$  are the debris flow and the water volume, respectively.

The volume  $V_T$  can be calculated by writing the volumetric balance reported in Eq. 2-3:

$$V_T = V_s + V_R + V_W \quad 2-3$$

where  $V_s$  is the volume of the solid phase and  $V_W$  is the water volume of the mobilized mass.  $V_W$  can be computed by employing Eq. 2-4:

$$V_W = \frac{1-c^*}{c^*} \cdot \mathcal{S} \cdot V_s \quad 2-4$$

where  $c^*$  is the volumetric concentration of dry sediments and  $\mathcal{S}$  is the degree of saturation. Substituting Eqs. 2-3 and 2-4 in Eq. 2-2, it is possible to obtain Eq. 2-5:

$$Q_T = \frac{V_s \cdot \left[ 1 + \frac{1-c^*}{c^*} \right] + V_R}{V_R} \cdot Q_R \quad 2-5$$

The volume of the solid phase  $V_s$  may be provided through in situ measurements, geomorphological estimates, empirical relationships, or expertize evaluations of the sediments volume. The technique used to obtain the debris flow discharge can be considered as volume based.

Alternatively, the debris flow discharge can be estimated based on the mean volumetric concentration of the sediments  $C_V$  (Eq. 2-6).

$$C_V = \frac{V_s}{V_s + V_R + V_W} \quad 2-6$$

Replacing Eq. 2-4 in Eq. 2-6, it is possible to obtain volume  $V_R$  as reported in the Eq. 2-7.

$$V_R = \frac{1 - (1 - S) \cdot C_V - \frac{C_V}{\epsilon^*} \cdot S}{C_V} \cdot V_S \quad 2-7$$

Combining together Eqs. 2-2, 2-3 and 2-7, another expression for the evaluation of the debris flow discharge is achieved, depicted in the Eq. 2-8.

$$Q_T = \frac{1}{1 - (1 - S) \cdot C_V - \frac{C_V}{\epsilon^*} \cdot S} \cdot Q_R \quad 2-8$$

Equations 2-5 and 2-8 are perfectly equivalent and express the debris flow hydrogram for the solid-fluid phase. The first equation is solid-volume-based while the second one is a function of the mean volumetric concentration of the solid sediments. In case of a saturation degree  $S$  equal to unity, Eq. 2-8 converges to the solution proposed by [Takahashi \(1978\)](#) and reported in Eq. 2-9:

$$Q_T = \frac{1}{1 - \frac{C_V}{\epsilon^*}} \cdot Q_R \quad 2-9$$

The liquid phase discharge can be evaluated using the “rational formulation” ([Turazza 1880](#)) reported in the Eq 2-10.

$$Q_R = \frac{1}{360} \cdot C \cdot I_{dT} \cdot A_m \quad 2-10$$

where:  $A_m$  is the catchment area;  $C$  is the runoff coefficient;  $I_{dT}$  is the average rainfall intensity (mm/h) corresponding to the return period  $T$ . With reference to the guidelines proposed in the Campania Region project VAPI ([Rossi and Villani 1994](#)), it is possible to express the average rainfall intensity according to Eq. 2-11 :

$$I_{dT} = (K_1 + K_2 \cdot \ln T) \cdot \frac{\mu_0}{\left(1 + \frac{d}{d_c}\right)^{C_i - D \cdot \varepsilon}} \quad 2-11$$

where:  $K_1$  and  $K_2$  are two coefficients (for the Campania Region they are fixed to 0.456 and 0.11, respectively);  $T$  is the return period;  $d_c$ ,  $C_i$ ,  $D$  and  $\mu_0$  are coefficients that describe the rainfall area;  $\varepsilon$  is the altitude above the mean sea level (expressed in meters). The term  $d$  in Eq. 2-11 is the critical rainfall duration and can be assumed to be equal to the runoff time (a.k.a. debris flow lag-time). Several authors proposed different formulation to estimate the runoff time ([Giandotti 1934](#); [Viparelli 1961](#)); however, the one proposed by [Chen et al.](#)

(2004) and reported in Eq. 2-12 is more suitable for the treatment of the uncertainties:

$$t_c = \frac{l}{v} + \frac{1}{72} \cdot \frac{L^{1.6}}{H^{0.6}} \quad 2-12$$

where:  $l$  is the length (in km) of the path that a drop of water has to travel to reach the flow (surface flow);  $v$  is the water velocity in the channel (it has been estimated in the interval 1.08-2.26 km/h by [Chen et al. \(2004\)](#));  $L$  is the channel length (in km);  $H$  is the difference in elevation between the ends of the stream (in km).

Assuming that  $V_R = Q_R \cdot t_c$  and combining equations from 2-9 to 2-12, it is possible to write calculate the debris flow discharge  $Q_T$ :

$$Q_T = \frac{1}{360} \cdot \frac{C \cdot A_m \cdot (K_1 + K_2 \cdot \ln T) \cdot \mu_0}{\left(1 + \frac{\left(\frac{l}{v} + \frac{1}{72} \cdot \frac{L^{1.6}}{H^{0.6}}\right)^{C_1 - D_{\text{sc}}}}{d_c}\right)} + \frac{1}{3600} \cdot \frac{V_s}{\left(\frac{l}{v} + \frac{1}{72} \cdot \frac{L^{1.6}}{H^{0.6}}\right)} \cdot \left[1 + \frac{(1-c^*)}{c^*} \cdot S\right] \quad 2-13$$

Eq. 2-13 provides a relationship in closed form for the calculation of the debris flow peak discharge, for a given return period  $T$  of the rainfall event. Eq. 2-13 may be multiplied by a reductive coefficient that [Tubino and Lanzoni \(1993\)](#) have derived from experimental data and fixed equal to 0.73.

#### 2.1.4 Uncertainty modelling in peak discharge estimation

As described by [De Paola et al. \(2015\)](#), the problem of discharge estimation is affected by several sources of uncertainty grouped in three categories: (a) the topographic parameters; (b) soil properties which have a significant spatial variability; (c) the debris flow mobilized volume and sediment concentration. Authors ([De Paola et al. 2015](#)) have threatened the problem of uncertainty modelling by implementing the entire methodology of debris flow discharge estimation (the closed-form in Eq. 2-13) in a Monte Carlo simulation framework.

The vector of the uncertain parameter may be defined as  $\Theta = [C, c^*, A_m, l, v, L, H, V_s]$  where the uncertainty in each parameter is described through its marginal probability distribution (eventual correlations are not considered). The probability distributions are fitted based on available estimates and measurements for the catchment object of the analysis or based on literature. An example of uncertainty characterization proposed by [Chen et al. \(2004\)](#) for a village near Taiwan is reported in Tab. 2-1 in order to give an idea of the order of magnitude of the quantities involved in the problem.



Variables $x_i$	Samples N	Ranges	Mean Values $\mu_{x_i}$	Variance $CV_{x_i}$ (%)
$A_m$ (ha)	31	310.4 ↔ 396.6	355.6	6.81
$l$ (km)	31	1.36 ↔ 1.73	1.55	5.22
$L$ (km)	31	1.47 ↔ 1.90	1.69	5.01
$H$ (km)	31	0.21 ↔ 0.22	0.216	1.64
$C_v$	-	0.15 ↔ 0.56	0.355	28.87
$C$	-	0.5 ↔ 0.8	0.65	11.54
$v$ (km/hr)	-	1.08 ↔ 2.16	1.62	16.67

Tab. 2-1: Statistics of topographic and debris-flow characteristic parameters (Chen et al. 2004).

By performing a sufficiently large number of simulations, a distribution of the debris flow peak discharge is obtained. In order to express the uncertainty in the estimation of the debris flow discharge, a probability distribution can be fit to the histogram of the simulated peak discharge values (Fig. 2-6). In this way, for each value of the design discharge (to be used in the propagation process described in the following section), the probability that the total flow discharge  $Q_t$  is lower than or equal to the design value  $Q_d$  can be obtained.

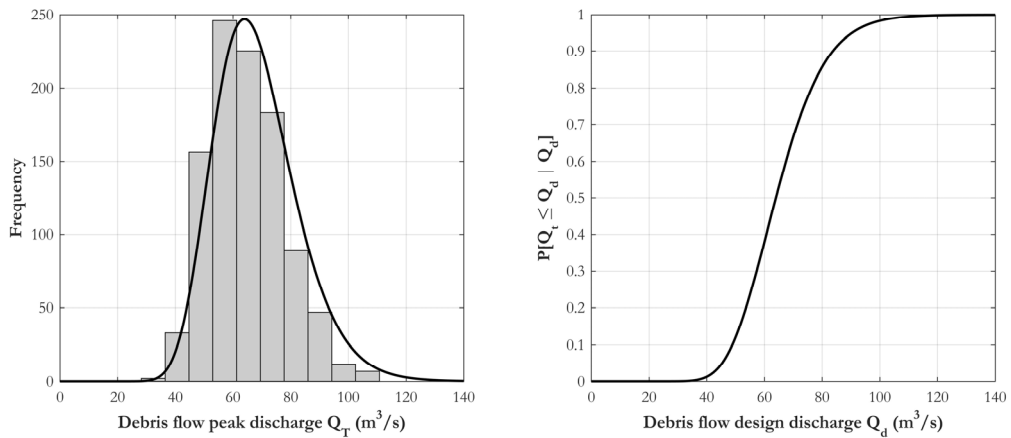


Fig. 2-6: Probability distribution of debris flow discharge.

## 2.2 Flood hazard assessment

Flood is commonly defined as a “temporary covering of land by water as a result of surface waters escaping from their normal confines or as a result of heavy precipitation” (Kron 2002). The definition is very general and implies that there are a lot of causes that may potentially contribute to flooding hazard. Given the dire importance of flooding hazard, the European Parliament published an executive document for the assessment and the management of flooding risk (EU 2007). This document basically prescribes a three-step procedure: (1) *preliminary flood risk assessment*, member states have to engage their departments to assess and consider the human health, life, environment and economic impact of floods; (2) *risk assessment*, all the necessary procedures for identifying the areas of significant risk which will then be modelled

in order to evaluate flood hazard and produce risk maps; (3) *flood risk management plans*, active involvement of all interested stakeholders in the process in order to mitigate and manage the flood risk.

The flood hazard assessment procedure outlined in this chapter is later on used for the case-studies. This procedure, which is particularly useful for flood discharge estimation in ungauged conditions, starts from the definition of the Intensity-Duration-Frequency curves (IDF) also known as rainfall curves ([Koutsoyiannis et al. 1998](#)). Based on the topography of the interested zone, it is possible to describe the catchment area/s, that is defined as the area from which a watercourse section receives surface runoff from rainfall. Once the catchment area is defined, the historical rainfall events may be used to calibrate the IDF curves for different return periods. Given a rainfall record, the intensity  $i$  is defined as the ratio between the rainfall depth  $h_r$  and the rainfall duration  $d$  (Eq. 2-14).

$$i = \frac{h_r}{d} \quad 2-14$$

To evaluate the rainfall curve corresponding to a specific return period, it is necessary to fit the rainfall data with a suitable probability model. The Generalized Extreme Value (GEV) family distributions are typically the most suitable to describe the extreme rainfall event and in the context of this work, a bi-parametric Gumbel model has been implemented ([Maione and Mosiello 1993](#)). In Eq. 2-15, the bi-parametric model for IDF curve is reported where  $a$  and  $n$  are the parameters of the IDF curve that can be estimated through a logarithmic regression  $\log(h_r)$  versus  $\log(d)$ .

$$h_r(d, T_R) = a \cdot d^n \quad 2-15$$

If the maximum annual rainfall data is not available for a desired duration, it is possible to disaggregate the available data in order to obtain the data for the chosen duration. Several models in literature provide such disaggregation techniques: [Connolly et al. \(1998\)](#) for short-time disaggregation (in the order of minutes up to 1 hour); [Olsson \(1998\)](#), [Güntner et al. \(2001\)](#) for long-time disaggregation (in the order of hours up to a full day).

After the definition of the rainfall curve, a time function of the flow discharge is necessary as the input of the hydraulic diffusion model. This function is known as hydrograph, and it is defined using a rainfall-runoff model. The area under the hydrograph is equal to the total discharge volume in the considered catchment. Since the water runoff is generally not directly measured in ungauged conditions, the classic curve number method (CNM) may be implemented ([SCS 1972](#)). The curve number (CN) value depends on the antecedent soil moisture conditions (AMC) in the catchment. There are three classes of AMC: AMC-I for dry soil; AMC-II for average condition of the soil; AMC-III for saturated soil.

According to the curve number method, the hydrograph in terms of discharge  $Q$  is implemented as a function of the time ([SCS 1972](#)). The hydrograph peak time  $t_p$  (in hours) can be obtained by the Eq. 2-16:

$$t_p = 0.5 \cdot D + t_l \quad 2-16$$

where:  $D$  is the rainfall duration in hours equal to concentration time proposed by [Viparelli \(1963\)](#);  $t_l$  is the catchment lag time in hours defined by the Eq. 2-17:

$$t_l = 0.342 \cdot \frac{L^{0.8}}{s^{0.5}} \cdot \left( \frac{100}{CN} - 9 \right)^{0.7} \quad 2-17$$

where  $L$  is the length of the main channel in kilometres and  $s$  is the mean slope (described in percentage).

### 2.3 Bi-dimensional numerical propagation in FLO-2D

A commercial software FLO-2D ([O'Brien et al. 2009](#)) is used to model the flow propagation. Flow propagation in FLO2D is based on the volume conservation and has been developed both for the propagation of flood and debris flow events. FLO2D is part of the hydraulic models approved by FEMA (Federal Emergency Management Agency) for flow-propagation studies. FLO-2D is capable of managing multiple input flood hydrographs, directly applied to both the un-channelled flows (2D propagation) and the channelled one (1D propagation). It can combine hydrological aspects (rainfall intensity, runoff, infiltration, etc.) with hydraulic aspects (channelling of flow through roads, the effect of buildings and obstructions on the flow, and the velocity variation of the flow between two elements). A schematic representation of the physical processes simulated by FLO-2D is reported in Fig. 2-7.

FLO-2D simulates the flow in a channel as a one-dimensional flow through the transversal sections, which may have rectangular, trapezoidal, or a user defined geometry. The flow along the roads is considered one-dimensional flow along a rectangular channel. The overland flow, can be modelled both as a two-dimensional flow and as multiple-channel flow. The code automatically considers the interactions between channels and floodplain through a particular processing routine that simulates the so-called “overbank” flow that is what happens when the maximum capacity of the channel is exceeded. This calculation routine allows the determination of the flow exchange with the surrounding terrain including the return to the channel flow. Similarly, the same routine computing also the flow exchange between the roads and the surrounding areas. Once the flow has passed the channel, it will disperse to other network elements depending on the topography, roughness and obstructions.

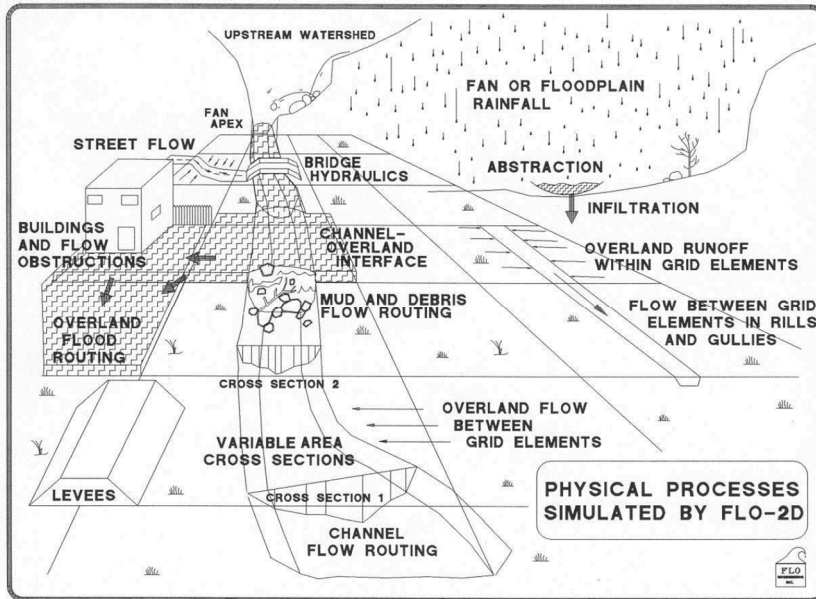


Fig. 2-7: Physical processes simulated by FLO-2D (O'Brien et al. 2009).

FLO-2D is based on the volumes conservation so that the flow in the computational domain is controlled by the topography and by the propagation resistance factors. The two-dimensional modelling is performed through a numerical integration of the flow-motion equations and of volumes conservation. The equations that govern these processes are the continuity equation (Eq. 2-18) and the dynamic wave equation (Eq. 2-19) also known as Saint Venant equations.

$$v \cdot \frac{\partial A}{\partial x} + A \cdot \frac{\partial v}{\partial x} + b \cdot \frac{\partial h}{\partial t} = 0 \quad 2-18$$

$$g \cdot \frac{\partial h}{\partial x} + v \cdot \frac{\partial v}{\partial x} + \frac{\partial v}{\partial t} = g \cdot (i - j) \quad 2-19$$

In Eq. 2-18 and 2-19:  $A$  is the area of the cross section;  $b$  is the depth of the flow at the section;  $v$  is the mean velocity at the section;  $b$  is the width of the top of the section;  $x$  is the position of the section measured from the upstream end;  $t$  is the time;  $g$  is the gravity acceleration;  $j$  is the energy loss per unit length of channel and per unit weight of fluid.

The Saint Venant equations cannot be solved analytically unless one makes some very restrictive assumptions, which are unrealistic for most situations. Therefore, numerical computational techniques have been implemented to solve the problem. The calculation procedure used in the code is based on the resolution scheme of central finite differences. Although this numerical scheme has a simple formulation, it has the drawbacks that the time-step must be very small and the numerical stability is restricted. In fact, the scheme of

finite differences may require a lot of computation time in cases when the flow waves up slightly, brusque changes in slope take place, and channels with highly variable sections are simulated.

To give an idea about the necessary operations for the propagation of flows with FLO-2D, the main steps of the algorithm will be briefly described hereafter.

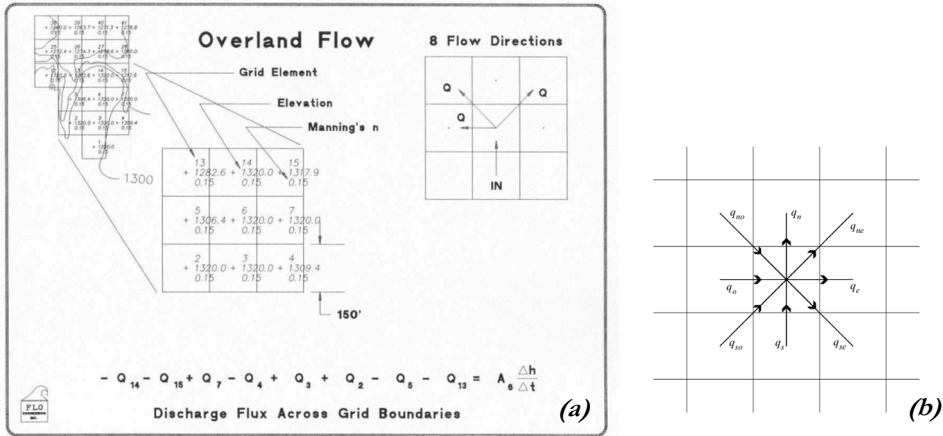


Fig. 2-8: (a) discharge flow across the sections in FLO-2D; (b) eight considered flow directions. (O'Brien et al. 2009).

Regarding Fig. 2-8(a), the entire area of propagation downstream is divided in cells. For each cell, FLO-2D evaluates the initial flow height, the roughness coefficients and the other hydraulic parameters (hydraulic radius, area of the transversal section, slope, wet perimeter) referring to the eight possible directions of the flow (Fig. 2-8(b)) by means of an arithmetical mean between the parameters of the actual cell and the one in the considered direction. Known all the hydraulic parameters, it is possible to obtain – for each possible direction– the velocity using the [Manning et al. \(1890\)](#) formula:

$$v = \frac{k}{n} \cdot R_b^{2/3} \cdot S^{1/2} \quad 2-20$$

Where:  $R_b$  is the hydraulic radius;  $S$  is the slope;  $k$  is a conversion factor;  $n$  is the Gauckler-Manning coefficient. The obtained values of velocity are used to solve the complete dynamic problem (Eq. 2-18 and 2-19) as seed in a Newton-Rapson algorithm ([Jennrich and Sampson 1976](#)). Three attempts are performed and if the procedure does not converge the solution of diffusive flow equation is used. The local acceleration is evaluated dividing the difference of the velocities (in the considered direction) by the time interval  $\Delta t$ . Therefore, the choice of the time interval has a crucial importance and it should be sufficiently little to ensure the stability of the solution (according to Courant-Friedrich-Lewy condition ([MacCormack and Paullay 1972](#))) but not too small to render the computational effort prohibitive.

Once the computational cycle on a time-step is completed, the stability criteria are

checked: if one or more elements do not satisfy the criteria, the results obtained for that step are discarded and the calculation is repeated for a smaller time interval.

### 2.3.1 Debris- and mud-flow propagation in FLO-2D

The adopted rheological model in FLO-2S is the quadratic one proposed by [O'Brien and Julien \(1985\)](#), which is particularly sensitive to the concentration of sediment in the flow, which may change continuously (e.g. due to the effect of dilution, remobilization of sediments that were deposited, etc.). In the quadratic model, the total tangential stress for debris flow or mud flow is defined as (Eq. 2-21):

$$\tau = \tau_y + \eta \left( \frac{dv}{dy} \right) + C \left( \frac{dv}{dy} \right)^2 \quad 2-21$$

where:  $\tau_y$  is the Mohr-Coulomb cohesion;  $\eta$  is the dynamic viscosity;  $C$  is the Bagnold's coefficient;  $v$  is the velocity;  $y$  is the flow depth. To parametrize all the involved terms, Eq. 2-21 is rewritten in terms of *energy dissipation slope*  $S_f$  (Eq. 2-22) integrating on the flow depth.

$$S_f = \frac{\tau_y}{\gamma_m \cdot b} + \frac{K \cdot \eta \cdot v}{8 \cdot \gamma_m \cdot b^2} + \frac{[n \cdot b \cdot \exp(m \cdot C_v)]^2 \cdot v^2}{b^{4/3}} \quad 2-22$$

where:  $\gamma_m$  is the specific weight of the mixture liquid-solid;  $b$  is the flow height;  $K$  is a coefficient that depend on the  $n$  Manning's parameter;  $v$  is the velocity;  $b$  and  $m$  are coefficients fixed equal to 0.0538 and 6.09, respectively;  $C_v$  is the volumetric concentration.

The Eq. 2-22 is numerically solved by FLO-2D and the obtained velocity represents the flow velocity across each one of the eight possible directions of the cell. Using the obtained velocity and the mean flow depth at each cell, the complete dynamic problem is solved calculating the Eq. 2-18 and 2-19.

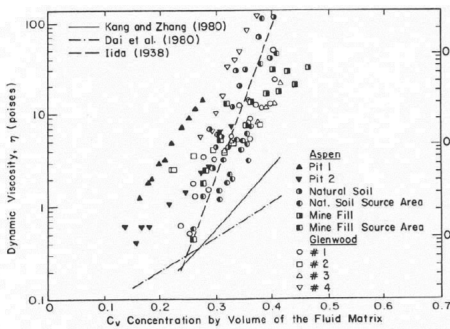


Fig. 2-9: Dynamic viscosity function of volumetric concentration ([O'Brien et al. 2009](#)).

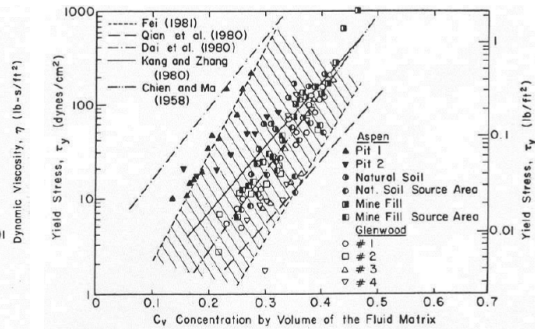


Fig. 2-10: Yield stress function of volumetric concentration ([O'Brien et al. 2009](#)).

The dynamic viscosity  $\eta$  and the Mohr-Coulomb cohesion  $\tau_y$  are generally correlated

to the volumetric concentration of sediments (Fig. 2-9 and Fig. 2-10) and several analytical relations exist fitted both on real field data and on literature data, as reported in Tab. 2-2.

Source	$\tau_y = \alpha e^{\beta C_v}$ (dynes/cm <sup>2</sup> )		$\eta = \alpha e^{\beta C_v}$ (poises)	
	$\alpha$	$\beta$	$\alpha$	$\beta$
Field Data				
Aspen Pit 1	0.181	25.7	0.0360	22.1
Aspen Pit 2	2.72	10.4	0.0538	14.5
Aspen Natural Soil	0.152	18.7	0.00136	28.4
Aspen Mine Fill	0.0473	21.1	0.128	12.0
Aspen Watershed	0.0383	19.6	0.000495	27.1
Aspen Mine Source Area	0.291	14.3	0.000201	33.1
Glenwood 1	0.0345	20.1	0.00283	23.0
Glenwood 2	0.0765	16.9	0.0648	6.20
Glenwood 3	0.000707	29.8	0.00632	19.9
Glenwood 4	0.00172	29.5	0.000602	33.1
Relationships Available from the Literature				
Iida (1938) <sup>*</sup>	-	-	0.0000373	36.6
Dai et al. (1980)	2.60	17.48	0.00750	14.39
Kang and Zhang (1980)	1.75	7.82	0.0405	8.29
Qian et al. (1980)	0.00136	21.2	-	-
	0.050	15.48	-	-
Chien and Ma (1958)	0.0588	19.1-32.7	-	-
Fei (1981)	0.166	25.6	-	-
	0.00470	22.2	-	-

*Tab. 2-2: Yield stress and viscosity as function of sediment concentration (O'Brien et al. 2009). Conversion: Shear stress, 1 Pa = 10 dynes/cm<sup>2</sup>; Viscosity, 1 Pa·sec = 10 dynes·sec/cm<sup>2</sup> = 10 poises.*





---

# Chapter 3

## Structural vulnerability

*In this Chapter the methodology proposed for the hydrogeological vulnerability assessment is outlined in detail. The methodology is focused primarily on the fragility assessment for a class of buildings and, without loss of generality, it can be applied to assess the fragility curve for a single building.*

### 3.1 State of art in hydrogeological vulnerability assessment

In the context of hydrogeological vulnerability assessment, the problem of landslide or debris flow is commonly distinguished from that of flooding. This distinction can be attributed to the following reasons: (a) the two problems generally involve areas that are quite different morphologically speaking: flooding is more of a problem in flat areas while landslides affect mainly the areas beneath the slopes; (b) the percentages of solid substances in landslides and debris flows are larger with respect to flooding so that the mass per unit of volume of the landslides is significantly larger with respect to that of flooding; (c) landslide is a gravitational phenomenon while flooding is a water-increasing phenomenon therefore the two hazards are substantially different from the velocity point of view; (d) the temporal scale: landslides have the scale of minutes or hours while flooding has the scale of several hours or days. The flash floods are somewhere between the two distinct phenomena explained above. Flash flood is defined as a flood that follows shortly (i.e. within few hours) after a heavy or excessive rainfall event ([Borga et al. 2007](#); [Gaume 2008](#); [Georgakakos 1986](#); [Sweeney 1992](#)).

Debris flow and landslide phenomena can potentially cause significant damage to buildings. The damage is mainly due to ([Kelman and Spence 2004](#); [Smith 1994](#)) (1) the hydro-dynamic component of the forces applied by the flow (since these phenomena are characterised by high velocity values); (2) the hydro-static component of the forces applied by the flow; (3) the accidental impact caused by flow-borne materials (e.g. rocks, trees and cars); (4) uplifting forces (buoyancy); (5) erosion and capillary effects. Depending on the

position of a building with respect to the flow and on the intensity of the event (e.g. the flow depth and velocity in correspondence of the building), the building may undergo significant non-structural and structural damage ([Faella and Nigro 2003](#)). The type of damage caused by a debris flow event also depends on the building type. For example, reinforced concrete (RC) frame structures may experience damage both to their primary load-bearing (the frame) and also to the secondary load-bearing systems (infill panels, ([Mavrouli et al. 2014](#))). On the other hand, for masonry structures, the load-bearing wall panels are subjected to the impact of the debris flow. Another important aspect, which is common to all structural types, is the role of the openings as the weakest links within a building. Usually, the doors and windows are the first elements to be swept away by a flow ([Mavrouli et al. 2014](#)).

In recent years, a number of studies have been performed with the aim of evaluating building vulnerability to debris flows based on expert judgement ([Bell and Glade 2004](#)), damage observation and loss estimation based on the past events ([Akbas et al. 2009](#); [Fuchs et al. 2007](#); [Quan Luna et al. 2011](#)). [Quan Luna et al. \(2011\)](#) derived physical vulnerability functions based on various intensity parameters such as the flow depth, impact pressure and kinematic viscosity. They used the ratio of the incurred monetary loss to the building reconstruction value (the 'loss ratio') as a non-dimensional measure of damage for the building. [Totschnig and Fuchs \(2013\)](#) proposed to extend and to merge physical vulnerability functions for residential buildings affected by fluvial sediment transport processes to other building types and torrent processes. These vulnerability functions used the sediment depth as intensity parameter and the 'loss ratio' as a proxy for physical damage to the building. They concluded that it is not strictly necessary for the vulnerability functions to be classified based on the different sediment-laden torrent process types. However, they highlighted the significant uncertainty associated with physical vulnerability prediction given the intensity parameter (in this case, sediment depth). [Papathoma-Köhle et al. \(2015\)](#) presented a multifunction tool-box for loss assessment, for rapid damage assessment due to debris flow and for updating of existing physical vulnerability curves. They underlined the problem of lack of sufficient data for the characterisation of vulnerability curves (defined in a similar manner in [Totschnig and Fuchs \(2013\)](#)) and showed how existing vulnerability curves can be improved adaptively if more damage data are available. They implemented a graphical user interface for damage recording and for the monetary loss assessment. The works described above have in common the fact that the physical vulnerability has been calculated quantitatively and based on empirical damage observations.

There have been a few attempts to quantify building vulnerability to debris flows using analytical models. [Nigro and Faella \(2010\)](#) classified the different failure mechanisms to debris flows for RC frames and masonry structures using limit analyses in order to calculate the critical flow velocity that can activate a structural failure mechanism. [Haugen and Kaynia \(2008\)](#), meanwhile, have proposed a methodology for calculating the dynamic response of

an equivalent single degree of freedom system to the impact of a debris flow.

Increasing attention has been focused during the past decades on the flood vulnerability and risk assessment. [Smith and Greenaway \(1988\)](#), [Torres et al. \(2013\)](#), [Davis \(1985\)](#), [Scawthorn et al. \(2006\)](#) and [Scawthorn et al. \(2006\)](#) defined general methodological approaches to flood risk assessment. Many research efforts are focused on several aspects of flooding problem, such as loss of life ([Jonkman et al. 2008](#); [Tapsell et al. 2002](#)), economic losses ([Pistrika 2009](#); [Pistrika and Tsakiris 2007](#)), and damage to buildings ([Bouchard 2007](#); [Schwarz and Maiwald 2008](#); [Smith 1994](#)). These works are mainly based on the observed damage after the flooding event classified using different discrete scales. [Kelman \(2002\)](#) classified the damage with a scale of six damage states (from DS0 to DS5) from no water contact to structural collapse or undermining of the foundation. Analogous to the definition of the damage grades in the European Macro-seismic Scale EMS-98 [Groenevelt and Grunthal \(1998\)](#), [Schwarz and Maiwald \(2008\)](#) and [Schwarz and Maiwald \(2012\)](#) proposed a modified damage scale distinguishing between structural and non-structural damage. [Charvet et al. \(2014\)](#) applied a statistical model to assess the fragility of different buildings with respect to Tsunami, based on the damage state classification of the Ministry of Land, Infrastructure and Transport (MLIT) defined after the tsunami occurred in Japan (2011) and depending on the index damage state (DS). A formulation to assess the vulnerability of a building in terms of damage state probability is proposed by [Nadal et al. \(2009\)](#) for riverine and coastal floods. [Dawson et al. \(2005\)](#) evaluated the flooding risk of a dike system through a sampling technique in a MC simulation approach.

## 3.2 The general framework for hydrogeological vulnerability and risk analysis

### 3.2.1 Performance measures and interface variables for hydrogeological risk analysis

In this work, the Performance Based approach proposed by [Cornell and Krawinkler \(2000\)](#) in the seismic field has been adapted for the hydrogeological case. As already explained in Section 1.5, it is possible to define the risk  $\lambda_{LS}$  in terms of mean annual frequency of exceeding a prescribed limit state  $LS$  as reported in Eq. 3-1:

$$\lambda_{LS} = \int_{IM} P[LS|IM] \cdot d\lambda_{IM} \quad 3-1$$

where:  $IM$  is the chosen intensity measure for the hydrogeological hazard (the height of the flow  $H$  or the velocity of the flow  $V$  or the vector composed of  $H$  and  $V$ ); The fragility term  $P[LS|IM]$  expresses the probability of exceeding the limit state  $LS$  given  $IM$ ; The hazard term  $\lambda_{IM}$  expresses the mean annual frequency of exceeding a given  $IM$  level.

In this work the limit state  $LS$  excursion is marked by a critical demand to capacity ratio corresponding to  $LS$  and denoted by  $DCR_{LS}$  exceeding unity. Adopting a vector-valued

IM consisted of height and velocity [H , V], it is possible to rewrite Eq. 3-1 as following:

$$\lambda_{(DCR_{LS} \geq 1)} = \int_{\Omega} \int_{\Omega_v} P[(DCR_{LS} \geq 1) | h, v] \cdot d\lambda_{(h,v)} \cdot dh \cdot dv \quad 3-2$$

where:

- $DCR$  is defined as the critical *Demand to Capacity Ratio* that represents the limit state  $LS$  according to a *safety factor* formulation ([Ditlevsen and Madsen 1996](#)). Therefore, the inequality  $DCR_{LS} \geq 1$  represents the exceedance of the limit state  $LS$ .
- $\lambda_{(DCR_{LS} \geq 1)}$  is the risk in terms of mean annual frequency of exceeding the given limit state  $LS$ .
- $h$  and  $v$  are the flow height and velocity, respectively. In general,  $h$  and  $v$  are functions of the *time*. However, for simplicity and without loss of generality, they are assumed to be envelope values for height and velocity. For instance, one can take the peak height  $h_{max}$  and the velocity at peak height  $v(h_{max})$  or vice versa the peak velocity  $v_{max}$  and the height at peak velocity  $h(v_{max})$ . In lieu of more detailed information the IM vector can consist of the pair of envelope values  $[h_{max}, v_{max}]$  assuming that the velocity and height maxima are perfectly synchronized.
- $\Omega_h$  and  $\Omega_v$  are the domains in which the variables  $h$  and  $v$  are defined, respectively.
- $P[(DCR_{LS} \geq 1) | h, v]$  is the probability that  $DCR_{LS}$  is larger than or equal to 1 given that the values of the flow height  $h$  and flow velocity  $v$  are known. This term represents the vulnerability part of the problem and it is expressed through the fragility curve ([Jalayer et al. 2016](#)) or the fragility surface that is estimated by propagating the uncertainties as described later in Section 3.2.3.
- $\lambda_{(h,v)}$  is the hazard term, also known as the inverse of the return period  $T_{R(h,v)}$ , expressed as the mean annual frequency of occurrence of a hydrogeological phenomenon characterized by height and velocity jointly exceeding of the couple of values  $[h, v]$ , respectively.

From a theoretical point of view, Eq. 3-2 completely describes the hydrogeological risk assessment in a probabilistic and performance based approach. However, the solution of the problem results rather complex:

1. In case of a vector-values intensity measure, the vulnerability assessment may result costly in computational terms;
2. In case of a two-component vector-valued intensity measure, the fragility curve becomes a surface and is more difficult to read and to grasp;
3. The calculation of hazard in the case of  $IM = [h, v]$  is possible only for flooding. For debris flow (in general, rainfall-induced cascading hydrogeological

phenomena), the hazard assessment is much more complex for the reasons explained in the sub-section 3.2.1.2.

The hydrogeological vulnerability (and risk) assessment problem implementing Eq. 3-2 is investigated separately in this work for flood and debris flow.

### 3.2.1.1 Flood risk assessment

In the case of flooding, the water tends to move from areas of higher altitude to lower altitude areas in a non-impulsive way. The water accumulation is a phenomenon that generally progresses with low speeds. Hence, the variable that has the greatest influence in the hazard assessment is the flow height  $h$ . Assuming that the occurrence of the hydrogeological phenomena characterized by exceeding the height value  $h$  and the velocity value  $v$  is a homogenous Poisson process, it is possible -without loss of generality- to write:

$$\left|d\lambda_{(h,v)}\right| = P[v|h] \cdot \left|d\lambda_{(h)}\right| \quad 3-3$$

Substituting the Eq. 3-3 in the Eq. 3-2:

$$\lambda_{(DCR_{i,s} \geq 1)} = \int_{\Omega} \int_{\Omega} P[(DCR_{i,s} \geq 1) | h, v] \cdot P[v|h] \cdot \left|d\lambda_{(h)}\right| \cdot dv \cdot dh \quad 3-4$$

where:  $\left|d\lambda_{(h)}\right|$  is the flooding hazard in terms of flow height and  $\lambda_{(h)}$  is the mean annual frequency of occurrence of a flooding phenomenon with a flow height greater than or equal to  $h$  (also known as the inverse of the return period of the rainfall  $T_{R(h)}$  capable of producing flooding height greater than equal to  $h$ );  $P[v|h]$  is the probability to have a certain velocity value given that the flow height is known.

The probability  $P[v|h]$  can be defined as an outcome of the hydraulic propagation (Section 2.3). That is, neglecting the uncertainties in the flow diffusion process,  $P[v|h]$  can be estimated deterministically. More specifically, the term  $P[v|h]$  can be modelled through the Dirac delta function ([Lighthill 1958](#)) as reported in the Eq. 3-5:

$$P[v|h] = \delta[v - v(h) | h] \quad 3-5$$

where  $v(h)$  is the velocity value function of the value of  $h$  (or a value of velocity that occurs at the same time as the corresponding value of height) and  $\delta[v - v(h)]$  is the Dirac delta. Substituting the Eq. 3-5 in the Eq. 3-4, the flood risk assessment expression simplifies to:

$$\lambda_{(DCR_{i,s} \geq 1)} = \int_{\Omega} \int_{\Omega} P[(DCR_{i,s} \geq 1) | h, v(h)] \cdot \left|d\lambda_{(h)}\right| \cdot dv \cdot dh \quad 3-6$$

### 3.2.1.2 Debris flow risk assessment

Assuming that the rainfall-induced debris flow occurrence is described by a homogenous filtered Poisson process, the risk expressed as the mean annual frequency of exceeding a given limit state can be calculated as:

$$\lambda_{\{DCR_{Y,S} \geq 1\}} = \int_{\Omega} \int_{\Omega} \int_{\Omega_{b,v}(i,d)} P[(DCR_{Y,S} \geq 1) | b, v] \cdot P[b, v | T, r] \cdot P[T | r = (i, d)] \cdot |d\lambda_{(i,d)}| \cdot db \cdot dv \quad 3-7$$

where:  $\lambda_{(i,d)}$  is the mean annual frequency of occurrence of a rainfall scenario  $r$  whose intensity and duration exceeds  $i$  and  $d$ , respectively. Note that it is assumed that the occurrence of a rainfall event of interest is expressed by a homogenous Poisson process.  $P[T | r = (i, d)]$  is the probability that a landslide is triggered given a certain rainfall event  $r = (i, d)$ . The probability  $P[T | r = (i, d)]$  is very complex to estimate because it depends on the initial and boundary conditions of the terrain ([Pagano et al. 2010](#); [Picarelli et al. 2008](#); [Picarelli et al. 2012](#)). Note that it is assumed that the occurrence of a landslide event is a filtered Poisson process with rate (a.k.a., mean annual frequency of occurrence) equal to  $P[T | r = (i, d)]$  where  $P[T | r = (i, d)]$  is the filter probability.  $P[b, v | T, r]$  is the probability to have a certain flow height and flow velocity given a certain rainfall scenario  $r$  and that the landslide has been triggered. Neglecting the uncertainties in the diffusion and the propagation of the debris flow given the rainfall scenario and that the landslide is triggered,  $P[b, v | T, r]$  can be modelled as a Dirac delta function denoted as  $P[b, v | T, r] = \delta[b - b_0, v - v_0 | T, r]$  and the triple integral in Equation 3-7 simplifies to:

$$\lambda_{\{DCR_{Y,S} \geq 1\}} = \int_{\Omega_{b,v}(i,d)} P[(DCR_{Y,S} \geq 1) | b_0, v_0] \cdot P[T | r = (i, d)] \cdot |d\lambda_{(i,d)}| \quad 3-8$$

where  $b_0$  and  $v_0$  are the propagated height and velocity at the location of interest.

Given the focus of this work on structural fragility assessment, the problem of landslide risk assessment has been tackled herein in a scenario-based manner (avoiding the complex problem of landslide trigger evaluation). Given that a landslide *scenario*  $S$  has happened, the Eq. 3-7 can be rewritten in a scenario-based approach:

$$P[(DCR_{Y,S} \geq 1) | S] = P[(DCR_{Y,S} \geq 1) | b_0, v_0] \quad 3-9$$

where  $b_0$  and  $v_0$  are the values of flow height and velocity, respectively, for a given landslide scenario  $S$ . Also in this case, it has been assumed that the uncertainties in the propagation and the diffusion of the flow are neglected for a given landslide/debris flow scenario.

### 3.2.2 Structural class and uncertainties characterization

A hydrogeological problem generally involves a relatively extended geographical area

in which a significant number of buildings, infrastructures, and elements of various nature are included. This work focuses on the buildings prone to the hydrogeological hazard and the group of all the buildings potentially affected by the same possible event which define a *portfolio of buildings*. A portfolio can be composed of several buildings that can have many differences (in terms of structural system, materials, number of storeys, class of use, etc.). It is possible to define, inside a portfolio, a certain number of *structural classes* composed of all the buildings sharing common characteristics enough to guarantee that their structural behaviour is similar. The assessment of the structural capacity of a class is a probabilistic problem because of the presence of many *uncertainty sources* in the problem. In particular, the uncertainties can be classified as (see e.g., [De Risi et al. \(2013\)](#)):

1. Modelling uncertainties: comprising all the parameters (related to: loading, mechanical material properties and constitutive laws, component capacities and capacity models and construction detailing) that affect the structural modelling and whose estimation is subjected to uncertainties
2. Building-to-building variability within a given class of buildings: Clearly the structural response of individual buildings within a given class is subjected to variabilities. This category employs probability distributions in order to model the building-to-building variability in various structural modelling parameters (of course, those parameters that are not common within the class. For example, if the class is defined by all masonry buildings, the structural material is not going to be subjected to building-to-building variability within the class).

It should be noted that the above distinction in the sources of uncertainty considered in this work is merely conceptual. From a practical point of view, both categories described above are handled in the same manner. From the mathematical point of view, an uncertain parameter can be modelled as a *random variable* that is an association between any possible outcome of an event (or a value) with a number that represents the probability that the event can occur. In this way, each uncertain parameter of the structural problem becomes a random variable characterized by its own probability distribution that describes the probability with which the variable can assume each possible value. The *uncertainty characterization* is the process of assigning probability distributions to a random variable. In the context of this work, a Bayesian approach is used. That is, the probability models assigned to each uncertain parameter reflect the amount of information available about the parameter of interest.

In Fig. 3-1, three example of probability distributions fitted to data are reported (uniform, Normal and Lognormal).

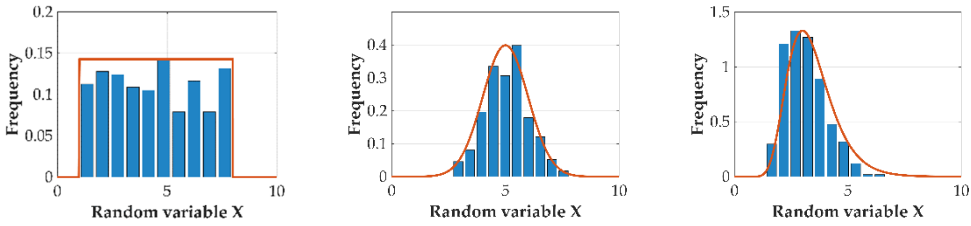


*Fig. 3-1: Example of probability distributions fit. From the left to right: uniform, normal and log-normal distribution fit.*

All the uncertain parameters considered in the problem are collected in a vector namely  $\Theta$ . That is, it is assumed that for a known vector  $\Theta$ , there are no uncertainties associated with the evaluation of the structural response to a given hydrogeological event of interest. The uncertain parameters considered in this work are further divided into following sub-groups: geometrical, material mechanical properties and loading. In this way, the vector  $\Theta$  can be considered composed of three sub-vectors as reported in Eq. 3-10.

$$\Theta = \{ \Theta_{\text{geometry}}, \Theta_{\text{material}}, \Theta_{\text{load}} \} \quad 3-10$$

In the following, it is described in detail how the uncertain parameters belonging to each sub group are characterized.

### 3.2.2.1 The uncertainties in geometrical parameters

As explained in the section related to the structural analysis, the hydrogeological hazard directly affects the external walls of the buildings. For this reason, in order to estimate the buildings capacity, it is necessary to take into account the uncertainties related to the walls geometry (load-bearing walls for masonry buildings and infill walls for reinforced concrete structures) and the building shape. Regarding the uncertainty categories discussed in the previous section, the geometrical uncertainties can be attributed to the building-to-building variability in each class of buildings.

The geometrical uncertain parameters are listed in Tab. 3-1.

$\Theta_{\text{geometry}}$		
Symbol	Parameter	Description
$S$	<i>Shape</i>	shape of the building, also defines the internal pattern of structural elements
$L$	<i>Wall length</i>	length of the entire wall façade (of a masonry building) or the length of the infill wall (for reinforced concrete building).
$H$	<i>Wall height</i>	height of the wall.
$T$	<i>Wall thickness</i>	thickness of the wall excluding covering.
$i$	<i>Internal span</i>	length of the wall span created by the orthogonal walls
$d_w$	<i>Door width</i>	width of the door
$d_h$	<i>Door height</i>	height of the door



$n_w$	Window width	width of the window
$n_{hb}$	Window height from bottom	distance between the upper part of the floor and the bottom part of the window
$o_R$	Openings rate	number of the openings on the wall divided by the length of the wall. It represents the average number of openings per unit length
$d_R$	Door rate	number of the doors on a given wall divided by the total number of openings.

Tab. 3-1: The uncertainties in geometrical parameters

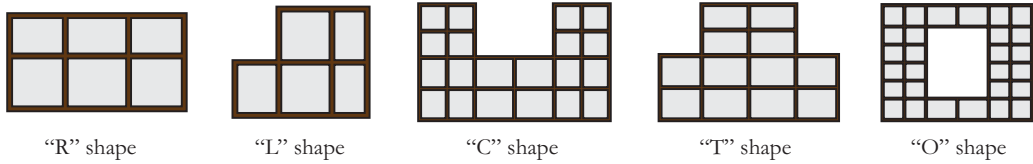


Fig. 3-2: Example of building shapes.

### 3.2.2.2 Uncertainties in material mechanical properties

The uncertain parameters related to material mechanical properties considered in this work are listed in Tab. 3-2.

$\text{Ⓜ}_{\text{material}}$		
Symbol	Parameter	Description
$E$	Young's modulus	elastic modulus of the linear elastic material in pure compression
$\gamma_m$	Material specific weight	weight per unit of volume of the structural material
$f_c$	Compressive resistance	compressive resistant stress
$f_t$	Tensile resistance	tensile resistant stress
$\tau_0$	Pure shear resistance	pure shear resistant stress of the material in absence of normal stresses.

Tab. 3-2: The uncertainties in material mechanical properties

### 3.2.2.3 The uncertainties in loading

The parameters listed in this category in Tab 3-3 represent the uncertainties in the evaluation of dead loads, hydrogeological loads (hydrostatics, hydrodynamics and accidental waterborne debris impact, as explained in 3.3.2):

$\text{Ⓜ}_{\text{loads}}$		
Symbol	Parameter	Description
$Q$	Dead loads	sum of all the dead loads exerted on the wall (e.g., floor weight, roof weight, etc.)
$\gamma_f$	Flow specific weight	weight per unit of volume of the flow characterized by a mixture of water and solid sediments
$D_c$	Drag coefficient	the coefficient quantifying the resistance offered by the ground to the flow
$\Omega$	Azimuth	angle between the North and the velocity vector of the flow measured

	<i>impact angle</i>	clockwise
$\varphi$	<i>Transfer coefficient</i>	coefficient quantifying the percentage of the hydrodynamic tangential loads applied to the wall.
$a_i$	<i>Accidental impact</i>	probability that a waterborne debris impacts on the wall.
$m$	<i>Impact mass</i>	mass of the waterborne debris.
$t$	<i>Impact duration</i>	duration of the impact of a waterborne debris.

Tab. 3-3: The uncertain in loading parameters

### 3.2.3 Overview of the implemented Monte Carlo Simulation framework

Monte Carlo Simulation (MCS) methods are a class of computational algorithms based on the repetition of random sampling to obtain numerical results of problems complicated (or impossible) to solve analytically. MCS methods are frequently used to solve three classes of problems: optimization, numerical integration and probabilistic assessment of multi-state systems. In 1930s, the Italian scientist Enrico Fermi was the first in MCS application during the study of neutron diffusion but he did not publish his study ([Metropolis 1987](#)).

In structural reliability, MCS methods are generally used to estimate the probability of failure of a structural system. Let the logical statement  $F$  be defined as: “failure of a structural system” or more generally “exceedance of a prescribed limit state  $LS$ ”. It is possible to evaluate the probability of failure using the total probability theorem by integrating over all possible values of the uncertain parameters considered in the problem:

$$P[F] = \int_{\Omega_{\Theta}} P[F | \Theta] \cdot f_{\Theta} \cdot d\Theta \quad 3-11$$

where:  $\Theta$  is the vector of all the uncertain parameters involved in the problem;  $f_{\Theta}$  is the joint probability density function of the uncertain parameters  $\Theta$ ;  $\Omega_{\Theta}$  is the domain of definition of the vector of the uncertainties  $\Theta$ . The integral in Eq. 3-11 might not lead to an analytical solution. Hence, in order to solve the problem numerically, it is possible to introduce an indicator binary function (defined in Eq. 3-12) which returns value 1 for each realization of the vector  $\Theta$  that leads to structural failure and 0 otherwise.

$$I(\Theta) = \begin{cases} 1 & \text{if the structural system fails} \\ 0 & \text{otherwise} \end{cases} \quad 3-12$$

Substituting Eq. 3-12 in Eq. 3-11, it is possible to approximate the probability of failure as reported in Eq. 3-13:

$$P[F] = \int_{\Omega_{\Theta}} I(\Theta) \cdot f_{\Theta} \cdot d\Theta \approx \hat{P}[F] = \frac{1}{N_{sim}} \cdot \sum_{i=1}^{N_{sim}} I(\Theta_i) = \frac{N_f}{N_{sim}} \quad 3-13$$

where:  $N_{sim}$  is the number of simulations to perform;  $N_f$  is the number of failures observed during the simulation process;  $\Theta^j$  is the  $j^{th}$  realization of the vector of uncertain parameters. The statistics of the estimator  $P[F]$  are reported, in particular the expected value, the variance and coefficient of variation in Eqs. 3-14, 3-15 and 3-16, respectively. It should be noted that in Eq. 3-16 the number of simulations  $N_{sim}$  is related to error of the estimation (cov) and the probability of failure. It is possible, in fact, to fix the level of probability and the acceptable error (in terms of coefficient of variation) and use the Eq. 3-16 to calculate the number of simulation needed to have a satisfactory estimation.

$$E(P[F]) = P[F] \tag{3-14}$$

$$\text{var}(P[F]) = \frac{P[F] \cdot (1 - P[F])}{N_{sim}} \tag{3-15}$$

$$\text{cov}(P[F]) = \frac{\sqrt{\text{var}(P[F])}}{P[F]} = \sqrt{\frac{1 - P[F]}{P[F] \cdot N_{sim}}} \tag{3-16}$$

In this work, MCS framework is used to estimate the structural fragility considering the uncertainties defined in section 3.2.2. The steps in the procedure are depicted in the logical scheme in Fig. 3-3. For each simulation, a realization of the vector  $\Theta$  is sampled from the joint probability distribution denoted as  $f_{\Theta}$  (defined based on the uncertainty characterization). Having all the numerical values of the uncertain parameters for a given simulation, it is possible to realize a complete structural model that can be solved through the incremental structural analysis (3.2.4). The procedure is repeated until the established number of simulations is achieved. For each simulation, the results of the analysis are going to be treated for the *robust fragility assessment* (section 3.2.5).

The uncertain parameters can be independent (if the information acquired about one parameter has no implication on other parameters) or can be correlated through a *correlation structure*. In case the uncertain parameters are independent, the joint distribution of the uncertain parameters  $f_{\Theta}$  is equal to the product of the marginal PDF's. That is, each uncertain parameter can be sampled individually.

To sample a parameter from its marginal PDF individually, a uniformly-distributed random variable  $r$  belonging to the interval  $[0, 1]$  is generated. Entering with value  $r$  in the probability axes of the parameter cumulative distribution function (the vertical axis in Figure 3-4), it is possible to obtain the sampled parameter as a one-to-one mapping of  $r$  through the cumulative distribution function as shown in Fig. 3-4.

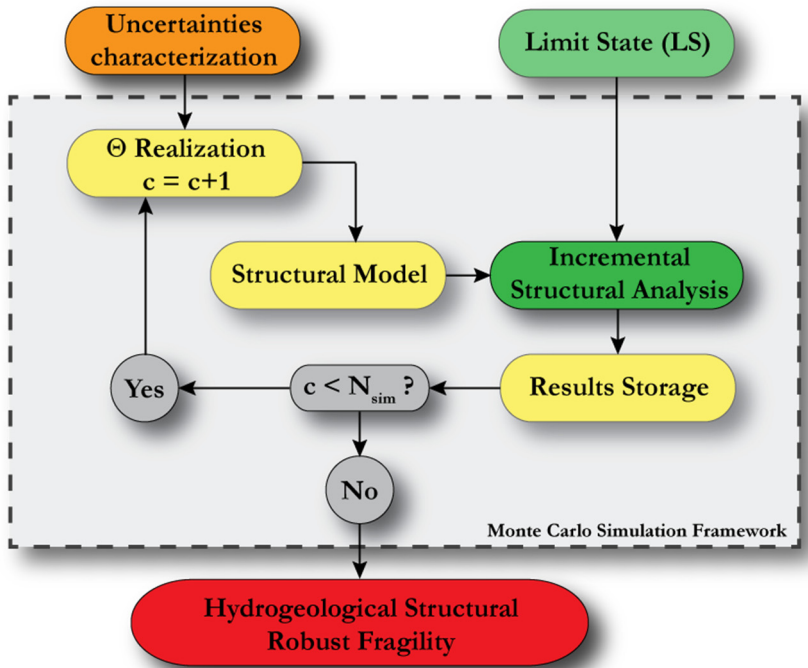


Fig. 3-3: MCS framework for structural fragility assessment.

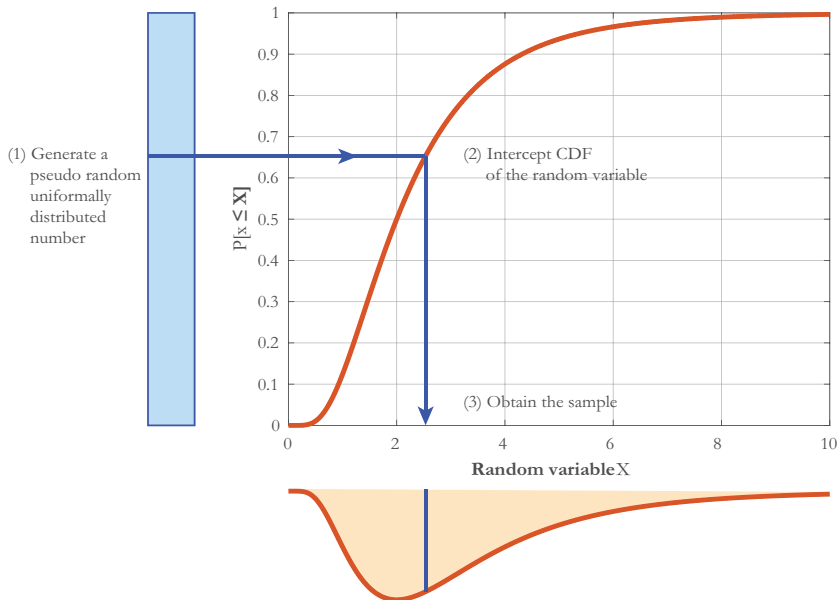


Fig. 3-4: Sampling from a marginal cumulative distribution function (CDF)

In the case of correlated parameters, the sampling procedure is a little bit more complicated. In the more general case, the joint probability density function for the vector

of uncertain parameters  $\Theta=[\theta_1,\theta_2, \dots,\theta_n]$  calculated by applying the product rule in probability (Jaynes 2003):

$$P(\Theta)=P(\theta_1,\theta_2,\dots,\theta_n)=P(\theta_1)P(\theta_2|\theta_1)P(\theta_3|\theta_1,\theta_2)\cdots P(\theta_n|\theta_1,\theta_2,\dots,\theta_{n-1}) \quad 3-17$$

According to the above equation, the first parameter  $\theta_1$  can be sampled from its marginal distribution,  $P(\theta_1)$ . Knowing the first parameter  $\theta_1$ , the second parameter  $\theta_2$  can be sampled from its conditional probability distribution  $P(\theta_2|\theta_1)$  by following the same procedure described above for the marginal distributions. Finally, the last component of the vector of the uncertain parameters  $\theta_n$  can be sampled from the conditional distribution  $P(\theta_n|\theta_1,\theta_2,\dots,\theta_{n-1})$ , knowing the  $n-1$  components of the vector (they are already sampled).

### 3.2.4 Incremental analysis procedure

In the implemented MCS framework, the critical demand to capacity ratio for a given limit state can be estimated by following an incremental analysis procedure. Before delving into the details of the structural analysis and modelling (described in detail in the Section 3.3), an overview of the adopted incremental analysis procedure has been outlined herein.

For a given realization of the vector of uncertain parameters  $\Theta$ , the incremental analysis procedure consists in the application of the hydrogeologically-induced loads as an increasing function of the chosen  $IM$  and calculating the  $DCR$  for each step of the analysis. Finally, it is possible to draw, for each realization of the vector of uncertain parameters, a curve composed of the pair  $[DCR_i^{(k)}, IM_i^{(k)}]$  where  $i$  is the  $i^{th}$  realization of the vector  $\Theta$  and  $k$  is the  $k^{th}$  analysis step.

Fig. 3-5 shows a typical representation of the curves obtained through the incremental analysis procedure. The hydrogeological loads are incremented as a linear function of the chosen  $IM$  (e.g., increasing flow height or increasing flow velocity) and the  $DCR$  for each analysis step are valued as explained in Section 3.3. When the  $IM$  is equal to 0, the points are representative of the stress state due to dead- and self-weight only.

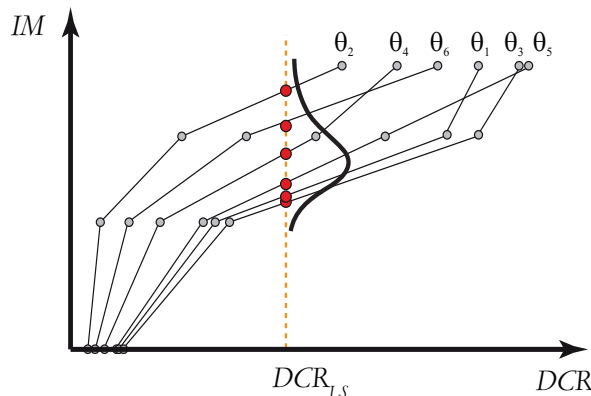


Fig. 3-5: Incremental analysis curves.

As shown in Fig. 3-5, given that each curve corresponds to a specific realization of the vector of uncertain parameters, a sample of  $\theta$  vector realizations would lead to a single realization of the incremental analysis curve. It can also be noted that the curves can be used to find (by interpolation) the distribution of the critical  $IM$  value corresponding to a prescribed value of the demand to capacity ratio for the prescribed limits state  $DCR_{LS}$  (e.g.,  $DCR_{LS}=1$ ).

### 3.2.5 The procedure for Robust Fragility assessment

A simulation-based Bayesian procedure can be employed in order to derive hydrogeological fragility curves conditioned on a Log Normal fragility model ([Jalayer et al. 2016](#); [Jalayer et al. 2013](#); [Jalayer et al. 2015](#)). This method can efficiently implement the results of the incremental analyses for a limited sample of  $\theta$  realizations (obtained through MCS herein) as “data” in order to provide a robust fragility curve (as a mean estimate over all possible fragility curves defined by a prescribed model, e.g., Log Normal model) and the mean plus/minus one standard deviation curves.

The log-normal model is perhaps the most universally adopted model for structural fragility. Three factors may have contributed to this widespread use; namely, the simplicity, non-negative argument variable, and the fact that it relies only on the first two (non-central) statistical moments (i.e., mean and standard deviation). Arguably, in circumstances where only the first two statistical moments are available, the Normal (log-normal) distribution is an optimal probability distribution to adopt ([Jaynes 2003](#)). It is worth mentioning that using a log-normal fragility model usually leads to more accurate estimations for the central part of the distribution. In other words, the Log Normal fragility model might not be the most suitable choice for tail-sensitive data. In this section, an overview of the method for robust fragility assessment is provided.

Assuming that a log-normal distribution identified by the vector of parameters  $\chi = [\eta, \beta]$  has been chosen as reported in Eq. 3-18:

$$P[LS | IM, \chi] = P[IM_{DCR_{LS}} \leq IM | \chi] = \Phi\left(\frac{\ln(IM/\eta)}{\beta}\right) \quad 3-18$$

where the vector of parameters  $\chi = [\eta, \beta]$  represents the median and the logarithmic standard deviation for the distribution of the natural logarithm of the critical  $IM$  values corresponding to the onset of limit state denoted by  $IM_{DCR_{LS}}$  (i.e., the  $IM$  values corresponding to  $DCR_{LS}=1$  from the incremental analysis curves described above). The joint probability distribution for parameters  $\chi$  of the log-normal distribution given vector  $\mathbf{D}$  (the vector of critical  $IM$  values calculated from the incremental analysis curves, red dots in Fig. 3-5) can be expressed as the posterior joint probability distribution for the mean and

standard deviation for the Normal probability distribution ([Box and Tiao 1992](#)):

$$p[\boldsymbol{\chi} | \mathbf{D}] = p[\eta, \beta | \mathbf{D}] = p[\eta | \beta, \mathbf{D}] \cdot p[\beta | \mathbf{D}] \quad 3-19$$

where  $p(\beta | \mathbf{D})$  is the posterior marginal distribution of  $\beta$  and  $p(\eta | \beta, \mathbf{D})$  is the posterior conditional distribution of  $\eta$  given  $\beta$ . The marginal PDF for  $\beta$  can be expressed as a derived  $\boldsymbol{\chi}$  distribution:

$$p[\beta | \mathbf{D}] = \left[ \frac{1}{2} \cdot \Gamma\left(\frac{\nu}{2}\right) \right]^{-1} \cdot \left( \frac{\nu \cdot s^2}{2} \right)^{\frac{\nu}{2}} \cdot \beta^{-(\nu+1)} \cdot e^{-\frac{\nu \cdot s^2}{2 \cdot \beta^2}} \quad 3-20$$

the posterior conditional distribution of  $\eta$  can be calculated as:

$$p[\eta | \beta, \mathbf{D}] = \sqrt{\frac{n}{2 \cdot \pi \cdot \beta^2}} \cdot \exp\left(-\frac{n \cdot (\ln \eta - \overline{\ln(IM_{DCR_{LS}})})^2}{2 \cdot \beta^2}\right) \quad 3-21$$

where  $\nu = n - 1$ ;  $\ln(IM_{DCR_{LS}})$  and  $s^2$  are the (logarithmic) sample average and sample variance of the set of critical IM values  $IM_{DCR_{LS}}$  for limit state  $LS$ , respectively. Finally, the robust fragility can be calculated by integrating over the joint (posterior) probability distribution of the log-normal fragility model conditioned on the set of data values  $\mathbf{D} = [D_i = IM_{i,DCR_{LS}}]$ :

$$P[LS | IM, \mathbf{D}] = E_{\boldsymbol{\chi}}[P(LS | IM, \mathbf{D}, \boldsymbol{\chi})] = \int_{\Omega(\boldsymbol{\chi})} \Phi\left(\frac{\ln(IM/\eta)}{\beta}\right) \cdot p[\boldsymbol{\chi} | \mathbf{D}] \cdot d\boldsymbol{\chi} \quad 3-22$$

where  $E_{\boldsymbol{\chi}}[\cdot]$  is the expected value operator over the vector of parameters  $\boldsymbol{\chi} = [\eta, \beta]$  and  $\Omega$  is the domain of vector  $\boldsymbol{\chi}$ . The variance  $\sigma^2$  in fragility estimation can be calculated as:

$$\sigma_{\boldsymbol{\chi}}^2 = E_{\boldsymbol{\chi}}[P(LS | IM, \mathbf{D}, \boldsymbol{\chi}) - P(LS | IM, \mathbf{D})]^2 = \int_{\Omega(\boldsymbol{\chi})} \left[ \Phi\left(\frac{\ln(IM/\eta)}{\beta}\right) - P(LS | IM, \mathbf{D}) \right]^2 \cdot p[\boldsymbol{\chi} | \mathbf{D}] \cdot d\boldsymbol{\chi} \quad 3-23$$

The robust fragility curve and its plus/minus one standard deviation confidence interval can be calculated efficiently using Monte Carlo Simulation. This is done by approximating Eqs. 3-22 and 3-23 in the following manner:

$$P[LS | IM, \mathbf{D}] \approx \tilde{R} = \frac{\sum_{i=1}^{N_{sim}} \Phi\left(\frac{\ln(IM/\eta_i)}{\beta_i}\right)}{N_{sim}} \quad 3-24$$

and,

$$\sigma_{\chi}^2 \approx \frac{\sum_{i=1}^{N_{sim}} \Phi \left[ \left( \frac{\ln(IM / \eta_i)}{\beta_i} \right) - \tilde{R} \right]^2}{N_{sim}} \quad 3-25$$

where:  $N_{sim}$  is the number of simulations;  $\eta_i$  and  $\beta_i$  correspond to the  $i^{th}$  realization of the vector of fragility parameters  $\chi_i$ . The vector  $\chi_i$  is simulated based on its probability density function  $p(\chi | \mathbf{D})$  in Eq. 3-19. This is achieved by first sampling  $\beta_i$  from its (posterior) marginal probability distribution in Eq. 3-20. In the next step, conditioning on  $\beta_i$ ,  $\eta_i$  is sampled from the conditional (posterior) distribution in Eq. 3-21. It should be noted that  $N_{sim}$  can assume very large values as the estimators shown in Eqs. 3-24 and 3-25 and the probability distributions in Eqs. 3-20 and 3-21 are all expressed in a closed- and analytic form.

### 3.2.6 Probability- and performance-based safety checking

A performance-based safety-checking objective can be expressed by the following generic inequality:

$$\lambda_{L,S} \leq \lambda_0 \quad 3-26$$

where  $\lambda_{L,S}$  is the mean annual frequency of exceeding an assumed limit state (i.e., a proxy for hydrogeological risk defined in Eq. 1-2) and  $\lambda_0$  is an acceptable risk level, expressed in terms of the annual frequency of exceedance or one over the return period  $T_R$ . The robust hydrogeological fragility curve denoted as  $P[LS | IM, \mathbf{D}]$  (blue continuous line in Fig. 3-6) can be integrated with flooding hazard  $k(IM)$ , expressed in terms of the mean annual frequency of exceeding a certain hydrogeological hazard intensity  $IM$  (red line in Fig. 3-6), in order to calculate the mean annual frequency of exceeding a prescribed limit state  $\lambda_{L,S}$ .

The mean annual frequency of exceeding a prescribed limit state (risk)  $\lambda_{L,S}$  can be expressed in a simple closed-form and analytical formulation based on the following set of simplifying assumptions ([Cornell et al. 2002](#); [Jalayer and Cornell 2004](#)): the robust fragility  $P[LS | IM, \mathbf{D}]$  can be expressed as a log-normal cumulative distribution function (CDF) with median  $\eta_{IM_{DCR_{L,S}}}$  and logarithmic standard deviation  $\beta_{IM_{DCR_{L,S}}}$ ; the hydrogeological hazard curve can be approximated by a power-law relation as a function of the hydrogeological  $IM$   $k_0 \cdot IM^{-k}$ . As a result, the performance objective in Eq. 3-26 can be expressed as following:

$$\lambda_{L,S} = k_0 \cdot \left( \eta_{IM_{DCR_{L,S}}} \right)^{-k} \cdot \exp \left( -\frac{1}{2} \cdot k^2 \cdot \beta_{IM_{DCR_{L,S}}}^2 \right) \leq \lambda_0 \quad 3-27$$

After simple algebraic manipulations, Eq. 3-27 can be rearranged and subsequently



expressed as:

$$\left(\frac{\lambda_0}{k_0}\right)^{-\frac{1}{k}} \leq \eta_{IM_{DCR_{LS}}} \cdot \exp\left(-\frac{1}{2} \cdot k \cdot \beta_{IM_{DCR_{LS}}}^2\right) \quad 3-28$$

The above performance-based safety-checking inequality can be represented in the following generic format:

$$IM(T_R) \leq FC \quad 3-29$$

where  $IM(T_R)$  is the hydrogeological  $IM$  corresponding to the hydrogeological return period  $T_R = 1/\lambda_0$  from the hydrogeological hazard curve or simply “hydrogeological demand”;  $FC$  is the factored critical hydrogeological  $IM$  or simply “factored capacity” (e.g., in meters of debris flow height):

$$IM(T_R) = \left(\frac{\lambda_0}{k_0}\right)^{-\frac{1}{k}} \quad 3-30$$

$$FC = \eta_{IM_{DCR_{LS}}} \cdot \exp\left(-\frac{1}{2} \cdot k \cdot \beta_{IM_{DCR_{LS}}}^2\right) \quad 3-31$$

In the presence of epistemic uncertainties for determining the median flooding height, it can be shown (Cornell et al. 2002) that the factored capacity  $FC_U$  can be calculated from the following:

$$FC_U = \eta_{IM_{DCR_{LS}}} \cdot \exp\left(-\frac{1}{2} \cdot k \cdot \beta_{IM_{DCR_{LS}}}^2\right) \cdot \exp\left(-\frac{1}{2} \cdot k \cdot \beta_U^2\right) \quad 3-32$$

where  $\beta_U$  represents the epistemic uncertainties in the estimation of the median hydrogeological  $IM$  from the fragility curve (i.e., the uncertainty in the parameters of the fragility model).

Fig. 3-6 shows a schematic representation of the factored capacity  $FC$  and the hydrogeological demand  $F_D = IM(T_R)$ . The figure features both the robust fragility curve (solid blue line) and its plus/minus one standard deviation curves (dashed blue lines). The hydrogeological hazard curve is plotted as a red solid line. As it can be seen from the figure,  $\beta_{IM_{DCR_{LS}}}$  is estimated as half of the logarithmic distance between the 84<sup>th</sup> and 16<sup>th</sup> percentiles and the epistemic uncertainty  $\beta_U$  as half of the logarithmic distance between the robust fragility plus and minus one standard deviation curves (Eqs. 3-33 and 3-34 respectively).

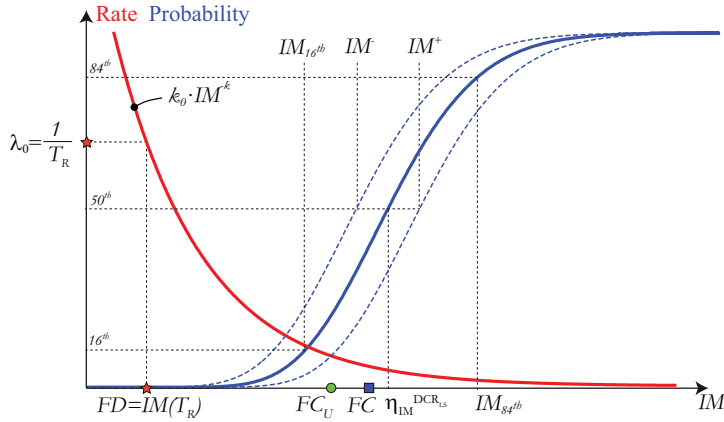


Fig. 3-6: The schematic diagram: robust fragility and the plus/minus one standard deviation confidence interval, hazard curve and the DCFD safety checking format.

The factored capacity  $FC$  (calculated from Eq. 3-31) is shown as a blue square and the factored capacity  $FC_U$  calculated taking into account the influence of the epistemic uncertainties (Eq. 3-32) is shown as a green dot on the Fig. 3-6.

$$\beta_{IM^{DCR,LS}} = \frac{1}{2} \cdot \ln \left( \frac{IM_{84^{th}}}{IM_{16^{th}}} \right) \quad 3-33$$

$$\beta_U = \frac{1}{2} \cdot \ln \left( \frac{IM^+}{IM^-} \right) \quad 3-34$$

The performance based safety check format proposed in Eq. 3-29 is also called *DCFD* (Demand and Capacity Factored Design). A more detailed discussion of how this safety-checking format may be useful to compare the efficiency of several hydrogeological risk mitigation strategies has been presented in [Carozza et al. \(2013\)](#) and [Carozza et al. \(2015\)](#).

### 3.3 Structural analysis

#### 3.3.1 Structural model

The study of the damages on the buildings produced by the historical hydrogeological disruption leads to three main considerations regarding the impact of these phenomena on the structures:

- (rigid body) displacement from original position due to the foundation/ground failure;
- severe damages in the structural and/or non-structural elements, which may lead to partial or total collapse of the structure;
- submersion of building by the flow and the debris;

- infiltration and invasion of debris flow and/or water inside the structure. Although the building may undergo minor structural damage, the infiltration of material severely impedes its functionality;

In Fig. 3-7, a selection of observed damages produced by the event of Sarno (SA, Italy) 1998 is reported. It can be seen that the walls are the most affected elements -because of their direct exposure to the flow- for both masonry structures and reinforced concrete structures. In case of reinforced concrete structures, damage in the columns are less frequent; this may be contributed to their smaller surface area exposed to the flow compared to infill walls. Nevertheless, [Faella and Nigro \(2003\)](#) did report cases of reinforced concrete structures with damaged columns.

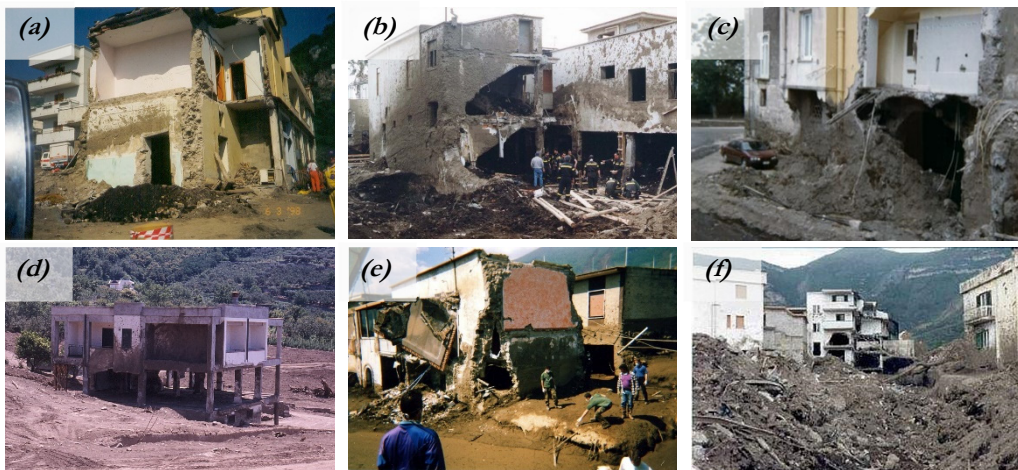


*Fig. 3-7: Some cases of damage produced by the event of Sarno (SA, Italy) 1998. (Courtesy of Dr. Melania De Falco and Vigili del Fuoco).*

The (local) failure of the walls has the immediate effect of allowing the entrance of the flow inside the buildings interrupting the functionality and putting at risk the lives of the people inside. Instead, from the structural point of view, the failure of one or more walls can induce different consequences based on the redundancy and the positioning of the resisting elements in the building. In fact, in case of reinforced concrete structures, the loss of the infill walls has no direct implications on the ultimate structural capacity (the walls are not primary load-resisting elements). This is while, in case of masonry structures, the failure of one or more walls can lead to the partial or total collapse of the building (the walls are primary load-resisting elements).

The pictures in Fig. 3-7 confirm what was said in the previous paragraph. The three cases of damaged masonry structures presented in Fig. 3-7 (a), (c) and (e), the walls directly affected by the debris flow have been completely destroyed and their loss in load-bearing capacity led to the partial collapse. In the cases of reinforced concrete damaged buildings in Fig. 3-7 (b), (d) and (f), the infill walls affected by the flow are completely destroyed but the primary load bearing structural system has remained almost intact.

Following the above considerations, the structural model employed to analytically assess the hydrogeological vulnerability should have three main characteristics:

1. To accurately represent the walls behaviour subjected to the gravity loads and hydrogeological induced loads;
2. To catch the failure mechanisms induced by the hydrogeological phenomena;

In literature there are several numerical models for masonry-like structures; such as but not limited to, *fiber-based elements*, *discrete elements methods*, *macro-element models*, *finite elements methods (FEM)*.

The *fiber-based elements* ([de Felice 2009](#); [Raka et al. 2015](#)) are generally suitable to model the normal stresses (the axial/flexural behaviour). The elements are modelled with a fiber-composed section where different constitutive laws can be assigned to each fiber.

The *discrete elements methods* ([Caliò et al. 2012](#); [Lemos 1998](#); [Pagnoni 1994](#); [Sinclair 2001](#)) provide to model the structures as an assembly of rigid blocks characterized by non-linear interface springs. These methods are useful to study the dynamics of discontinuous structures but they have a low feasibility in detailed modelling of large three-dimensional structures and the modelling of hydrogeologically-induced failure mechanisms.

The *macro-element models* ([Augenti et al. 2011](#); [Lagomarsino et al. 2013](#); [Magenes 2000](#)) consider the structures composed of a series of macro elements opportunely characterized based on the element nature (e.g., pier panels, floor panels, joint panels, etc.). These methods are very efficient computationally-speaking, but they are especially useful for modelling the in-plane failure. These models are less suitable for modelling the out-of-plane mechanisms (typical of a failure hydrogeological produced).

The *finite elements methods* ([Gambarotta and Lagomarsino 1997](#); [Lourenço 1996](#); [Luciano and Sacco 1998](#)) provide an efficient discretization of the structures in elements with finite dimensions (that, based on the needs, can be increased or reduced in order to manage the accuracy level wanted) with suitable shape functions which allow the resolution of the system. These methods are computationally demanding; however, they are particularly suitable for modelling the stress distribution inside the structure (especially helpful for back analyses and for catching all the possible failure mechanisms). In the context of *FEM*, there are two possibilities for modelling the masonry panels: using a micro-model of the masonry (mortar and blocks are modelled discretizing them separately) or a meso-model ([Pina-Henriques and Lourenço 2004](#)) of the masonry (mortar and blocks are modelled discretizing them together in recursive *Representative Volume Elements* as reported in Fig. 3-8).

In this work, the *FEM* has been implemented as a meso-scale model by considering each finite element as representative volume of the complete masonry (i.e., stones plus mortar for masonry buildings and bricks plus mortar for the infill walls of the reinforced concrete buildings). Fig. 3-9 depicts an example of mesh discretization of the implemented

FEM model. The openings are considered either as voids or as shell elements characterized by a material constitutive law representative of the closure system.

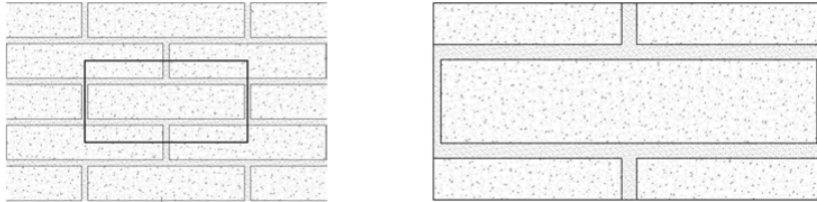


Fig. 3-8: The Representative Volume Element (RVE) proposed by [Pina-Henriques and Lourenço \(2004\)](#).

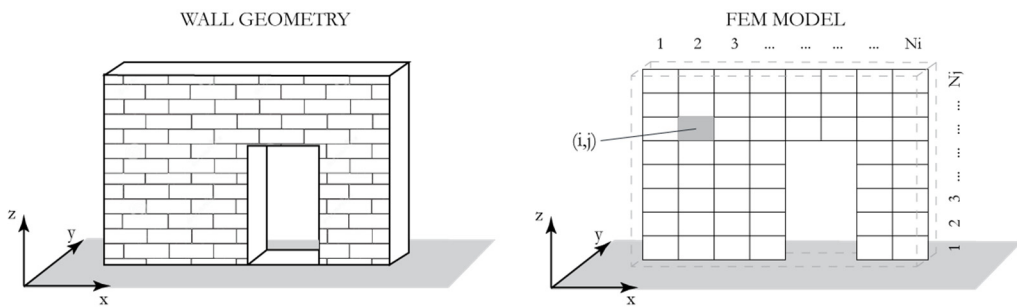


Fig. 3-9: Example of mesh discretization of a wall for the FEM analysis.

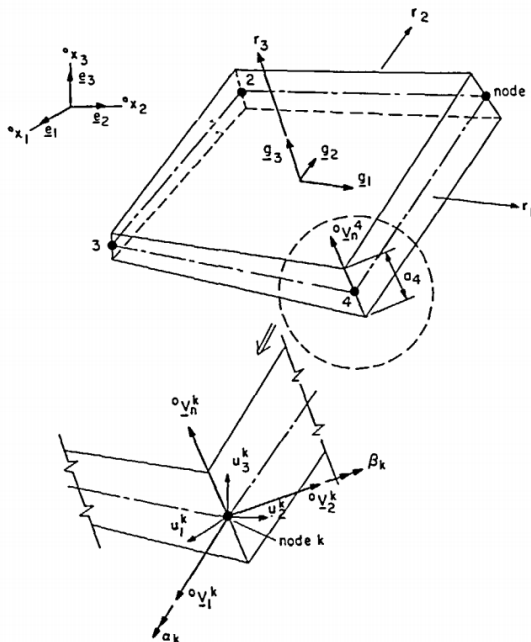


Fig. 3-10: The four-nodes shell element proposed by [Dvorkin and Bathe \(1984\)](#).

In this work the four-nodes shell element proposed by [Dvorkin and Bathe \(1984\)](#) and reported in Fig. 3-10, which is implemented in OpenSees software ([McKenna et al. 2006](#)), has been chosen. The elements are characterized by the material properties explained in section 3.3.3 and the loads are applied as forces and moments on the nodes obtaining by attributing the surface distributed loads based on their areas of influence. The boundary conditions are modelled through the application of restraints and constraints to the boundary nodes. For the three-dimensional model, the internal constraints are accounted considering the intersection between different elements in the same nodes, while for the simplified two-dimensional models, it is possible to reproduce the effect of the foundations, floor systems and other walls (e.g., orthogonal walls) constraining the nodes.

For each node in the model, the results of the *FEM* analysis is represented by a list containing the 6 components of the spatial stress tensor and the 6 components of the spatial displacement. Starting from the nodal components of the spatial stress tensor it is possible to obtain the stresses on all the faces of a generic shell element in order to perform the safety checks explained in the section 3.3.4.

### 3.3.2 Statics and hydrogeological-induced actions

A generic configuration of the loads patterns is represented in Fig. 3-11. The load on the generic wall can be applied to the front surface, to the side sections or to the upper and lower sections. As shown in the figure, each load can be schematically represented by a mathematical function described as function of space and time.

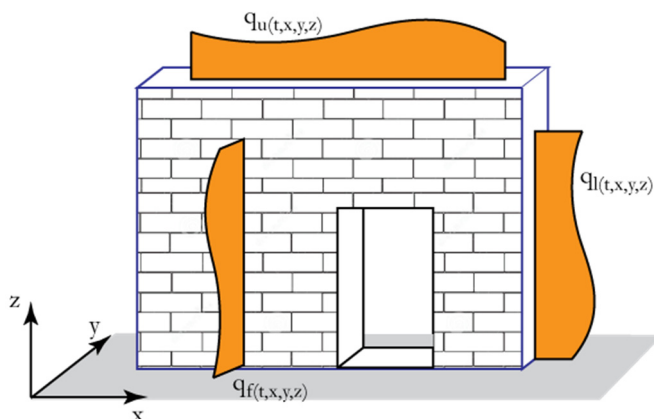


*Fig. 3-11: A representation of generic loads applied to a wall.*

The characterization of loading is one of the most important stages in the analysis. In general, the loads applied to the structure as a consequence of rainfall-induced hydrogeological phenomena can be classified into two main categories:

- *dead loads and self weight*, loading of a non-hydrogeological nature, applied to the

structure contemporary with hydrogeological phenomena (e.g., self-weights, floor loads, structural- and non-structural- fixed loads, etc.);

- *hydrogeologically-induced actions*, loading produced by the hydrogeological phenomena on the structure (e.g., pressures, impacts, etc.).

The characterization of the static loads is performed through preliminary structural analysis considering the structural type, the specific weights and all other loads applied to the structure. The uncertainties in the estimation of the static loads are considered in the procedure (as explained in the section 3.2.2.3).

The hydrogeologically-induced actions, as reported by [Kelman and Spence \(2004\)](#), should take in to account all the effects due to both the immediate impact and also due to the exposure of the materials to mud/debris and water. The hydrogeologically-induced actions can be classified as follows.

1. *Hydrostatic actions*. The hydrostatic pressure produced by the fluid that submerges the structure totally or partially (up to a certain height).
2. *Hydrodynamic actions*. The hydrodynamic pressure produced by the fluid that makes an impact against the structure with a velocity greater than zero.
3. *Debris actions*. Actions incurred by the impact of flow-borne debris against the structure.
4. *Erosion actions*. Scouring of structural and non-structural material due to elongated contact with the flow.
5. *Buoyancy actions*. The buoyancy forces (function of the submerged volume of the building) create an uplift effect which could result in the floating of the entire building or a part of it.
6. *Non-physical actions*. Degradation of the structure induced by elongated contact with the flow or exposure to active environmental agents.

Given the focus of this work on assessment of the structural vulnerability, the effects of hydrostatic, hydrodynamic and debris impact are taken into account.

The hydrostatic pressure  $p_{hs}(z)$  is governed by Stevin's law, and can be calculated through the Eq. 3-35:

$$p_{hs}(z) = \gamma_f \cdot (b - z) \tag{3-35}$$

where  $\gamma_f$  is the specific weight of the flow,  $z$  is the abscissa measured from the bottom of the structure and  $b$  is the flow height.

The hydrodynamic actions can be induced due to both flow velocity and also due to transient water level (i.e., waves). However, in an urban context, the hydrodynamic actions due to velocity of the flow seems to be more critical, as also shown in [Roos et al. \(2003\)](#). The hydro-dynamic pressure  $p_{hd}(z)$  can be derived as reported in Eq. 3-36:

$$p_{hd}(z) = C_d \cdot \rho_f \cdot v^2(z)$$

where  $C_d$  is the drag coefficient (typically ranging between 1.2 and 2.0 ([FEMA 2000](#)));  $\rho_f$  is the mass density of the water ( $\rho_f = \gamma_f/g$ ,  $g$  is the gravity acceleration);  $v(z)$  is the flow velocity vector at height  $z$ . It can be observed that the hydrodynamic pressure distribution is directly proportional to the square root of the velocity along the height. In lieu of detailed hydraulic calculations, the distribution of velocity along the height can be obtained based on simplified assumptions. Fig. 3-12 illustrates a typical representation of the velocity profile along a vertical surface.

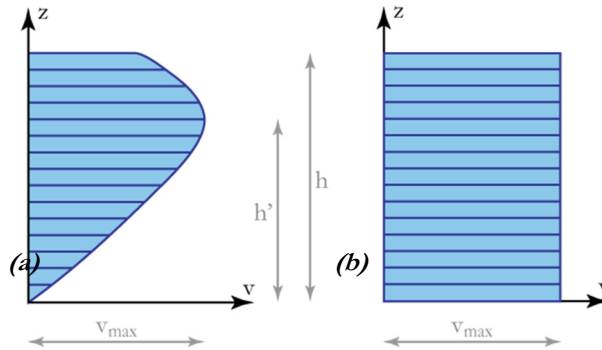


Fig. 3-12: (a) Velocity profile along the height. (b) Approximate velocity profile.

It can be observed that the maximum velocity is reached somewhere below the water surface. In this work, an approximate velocity profile along the structural height is assumed as illustrated in Fig. 3-12(b) ([Jalayer et al. 2016](#)). This consists in adopting a constant velocity profile equal to the maximum velocity.

The approximate hydrodynamic profile adopted herein, divided into normal and tangential orthogonal components, is demonstrated in Fig. 3-13 together with the hydrostatic profile.

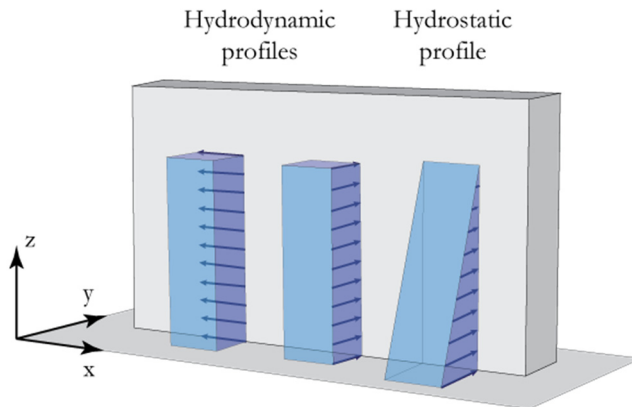


Fig. 3-13: hydrostatic and hydrodynamic pressure profiles.



Regarding the actions due to debris impact, alternative formulations in the literature for calculation of the impact forces, for instance, the impulse-momentum ([FEMA 1995](#)), the work-energy ([NAASRA 1990](#)) and the contact stiffness ([AASHTO 1998](#)), lead to substantially equivalent results. The two latter approaches require information about the kind of debris that hits the structure, the stopping distance and the contact stiffness of the debris impact against the structure. Thus, in this work the impulse-momentum formulation has been adopted to calculate the debris impact. The debris impact ( $F_{DI}$ ) can be calculated through the Eq. 3-37:

$$F_{DI} = \frac{W_D \cdot v_D}{g \cdot t} \quad 3-37$$

where  $W_D$  is the debris weight;  $v_D$  is the debris velocity (assuming that the debris is flow-borne,  $v_D = v_{max}$ );  $g$  is the gravity acceleration; and  $t$  is the impact duration, typically considered equal to 1 second ([Authority of Po River Basin 2007](#)).

### 3.3.3 Material models

The masonry walls are realized by putting together in a “system” different structural materials with different assembly techniques. This make the “masonry material” one of the most challenging from the point of view of characterization of material mechanical properties ([Augenti 2004](#)). The “masonry material” is composed of:

- stone (or brick) elements that represent the structure of the system;
- mortar made up of different binder-base material (e.g., cement, lime, etc.);

The resulting “masonry material” ends up having different characteristics compared with its two main constituting parts (brick and mortar). Since the *FEM* model is defined by considering the shell element as a representative masonry volume composed of stone (or brick) and mortar, the material assigned to the shell element is an idealized homogeneous material, characterized by the behaviour of the masonry system material.

Many researchers have studied the behaviour of the masonry material ([Arya and Hegemier 1978](#); [Calvi and Magenes 1991](#); [Capozucca 2004](#); [Chuxian 1984](#); [Kaushik et al. 2007](#); [Sawko 1982](#); [Turnšek and Čačovič 1971](#)). A comparison of experimental constitutive laws for masonry in terms of axial deformation versus axial stress is reported in Fig. 3-14 for 8 specimens of tuff masonry with mortar based on natural sand and pozzolana-like reactive aggregates ([Augenti and Parisi 2010](#)). Neglecting the specific numerical values, the behaviour shape-wise is representative of a generic masonry-based material. It is characterized by a quasi-linear elastic range followed by a short highly-non-linear elastic range up to the maximum compressive stress. The post-peak behaviour is characterized by a non-linear inelastic range with variable length.

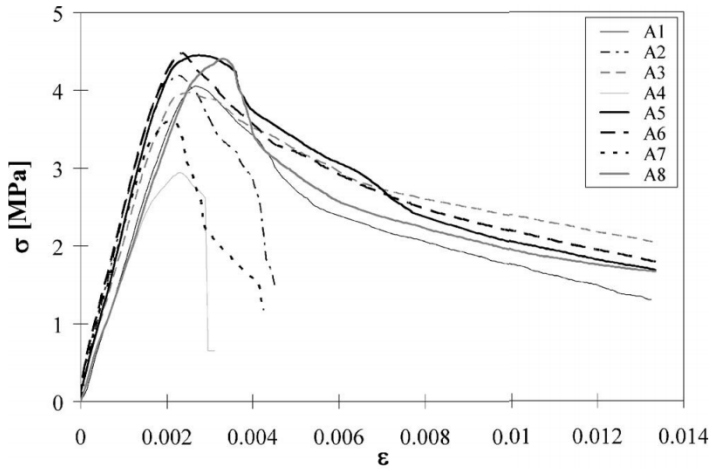


Fig. 3-14: Experimental constitutive laws for 8 tuff masonry specimens (Augenti and Parisi 2010).

Fig. 3-15 shows a comparison between alternative constitutive laws (normalized to corresponding peak stress and strain values for facilitating comparison) for masonry material. As shown in Fig. 3-15, an average predictive model of the masonry constitutive law would be more precise in the elastic part (where the dispersion between the alternative models is low) than in the post-elastic part (where the dispersion is much higher). This can be justified by fact that the compression behaviour in the elastic range is dictated only by the materials' mechanical behaviour. However, in the post-elastic range also the quality and the laying-in-place play a fundamental role in the resistance mechanism.

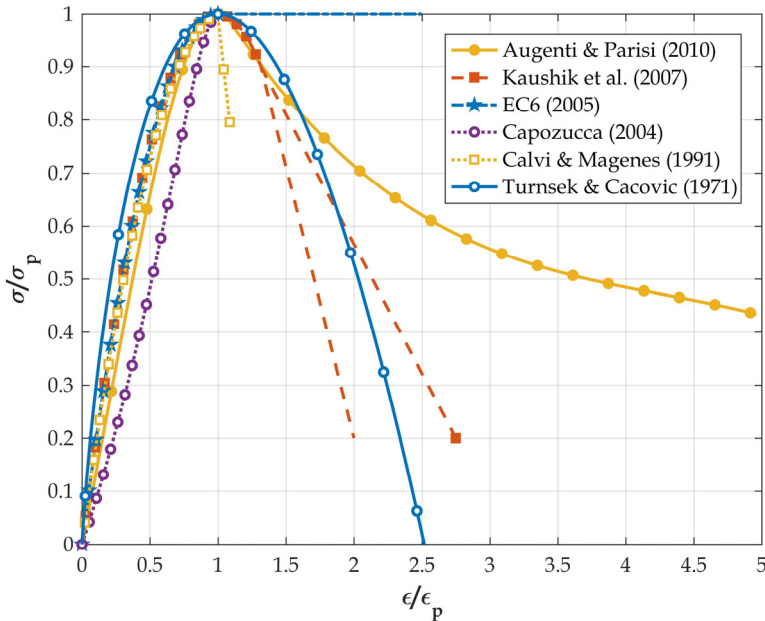


Fig. 3-15: Comparison between different predictive constitutive models.

The following considerations have been made in order to select the suitable predictive constitutive model for masonry material in the context of this work:

- Portfolio risk assessment is usually performed in lieu of site-specific laboratory tests. It is usually based on visual surveys and relevant literature;
- Adopting a general literature-based predictive model for masonry material constitutive behaviour is more justifiable in the elastic range;
- Due to the impulsive (non-cyclic) nature of the debris flow impact, it is expected that the global structural behaviour is more governed by strength-based criteria rather than deformation-based ones.

For the above-mentioned reasons, and for the sake of simplicity, an elastic constitutive behaviour up to the point of maximum peak strength has been assumed herein. It is important to mention that this assumption does not lead to any loss of generality in the methodology and it can be relaxed by adopting a non-elastic constitutive material. The characteristic parameters of the implemented masonry material model are reported in Tab. 3-4.

Symbol	Parameter	Description
$E$	<i>Young's modulus</i>	the elastic modulus of the linear elastic material in the pure compressive state.
$G$	<i>Shear modulus</i>	shear elastic modulus.
$\nu$	<i>Poisson's ratio</i>	the ratio of transverse to axial strain.
$\gamma_m$	<i>Material specific weight</i>	weight per unit of volume of the masonry material.
$f_c$	<i>Compressive resistance</i>	compressive resistant stress of the masonry material.
$f_t$	<i>Tensile resistance</i>	tensile resistant stress of the masonry material.
$\tau_0$	<i>Pure shear resistance</i>	pure shear resistant stress of the material in absence of normal stress.

*Tab. 3-4: Material characteristic parameters.*

The parameters  $E$ ,  $G$ ,  $\nu$  and  $\gamma_m$ , described in Tab. 3-4, are implemented in the *FEM* model to perform the structural analysis while the parameters  $f_c$ ,  $f_t$  and  $\tau_0$  are used to make the safety checks described in the next section.

### 3.3.4 Safety checks

As it was mentioned in the section 3.2.4, the critical *IM* for a given realization of vector  $\Theta$  can be calculated from the incremental analysis curve as the *IM* value that corresponds to  $DCR = 1$  (demand to capacity ratio, see Fig. 3-5). The performance variable *DCR* is defined, according to a “weakest-link” concept, as the critical demand to capacity ratio throughout the structure. In other words, *DCR* is calculated as the largest demand to

capacity ratio throughout all the structural elements and all the possible failure mechanisms.

Given the importance of the walls as the front elements physically exposed to the flow, particular attention has been given to considering all the potential wall failure mechanisms. In Fig. 3-16, the wall failure mechanisms considered are illustrated.

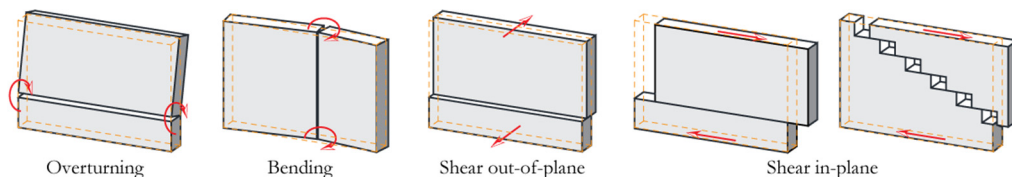


Fig. 3-16: Walls failure mechanisms.

These failure mechanisms consist of:

- *overturning (OVE)* rotation of the wall (or of a part of it) around a horizontal axis due to loads applied orthogonal to the wall plan or due to a vertical resultant force eccentric respect to the centre of gravity;
- *bending (BEN)* rotation of the wall (or a part of it) around a vertical axis due to loads applied orthogonal to the wall plan;
- *shear out-of-plane (SOP)* cracking of the wall along a horizontal section with a consequent relative displacement of the parts along an axis orthogonal to the wall due to loads applied orthogonal to the wall plan;
- *shear in-plane (SIP)* cracking of the wall along a horizontal (sliding shear) or oblique (diagonal shear) section with a consequent relative in-plane displacement of the parts due to loads applied in the longitudinal direction of the wall.

For each element, considering a weakest-link criteria for identifying the critical demand to capacity ratio, the *DCR* is defined as:

$$DCR^{(i,j)} = \max\{DCR_{OVE}^{(i,j)}, DCR_{BEN}^{(i,j)}, DCR_{SOP}^{(i,j)}, DCR_{SIP}^{(i,j)}\} \quad 3-38$$

where:  $i$  and  $j$  are the element indexes defined in the Fig. 3-9.

Herein, a stress-based approach is adopted for finding the critical DCR for a given element. Therefore, it is important that the stress components considered for safety-checking are consistent with the potential failure mechanisms described right before. Considering an infinitesimal wall element and a Cartesian reference system, it is possible to identify the different components of the stress tensor involved in the various mechanisms (Fig. 3-17).

Considering the different stress components that each failure mechanism involves, Eq. 3-38 can be rewritten as following:

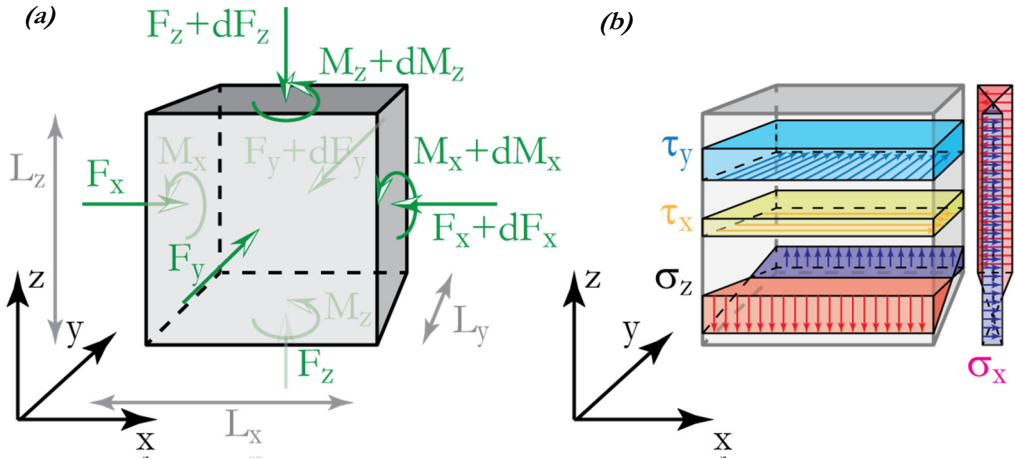


Fig. 3-17: Forces (a) and stresses (b) that govern the considered failure mechanisms.

$$DCR_{OVE}^{(i,j)} = \left( \frac{\sigma_{z,D}}{\sigma_{z,C}} \right)_{(i,j)} \quad 3-39$$

$$DCR_{BEN}^{(i,j)} = \left( \frac{\sigma_{x,D}}{\sigma_{x,C}} \right)_{(i,j)} \quad 3-40$$

$$DCR_{SOP}^{(i,j)} = \left( \frac{\tau_{y,D}}{\tau_{y,C}} \right)_{(i,j)} \quad 3-41$$

$$DCR_{SIP}^{(i,j)} = \left( \frac{\tau_{x,D}}{\tau_{x,C}} \right)_{(i,j)} \quad 3-42$$

where:  $\sigma_{z,D}$  and  $\sigma_{z,C}$  are normal stress demand and capacity, respectively, in the direction  $z$ ;  $\sigma_{x,D}$  and  $\sigma_{x,C}$  are the normal stress demand and capacity, respectively, in the direction  $x$ ;  $\tau_{y,D}$  and  $\tau_{y,C}$  are the tangential shear demand and capacity, respectively, in the direction  $y$ ;  $\tau_{x,D}$  and  $\tau_{x,C}$  are the tangential shear demand and capacity, respectively, in the direction  $x$ . All the stress demand values herein are calculated through structural analysis; while, the stress capacities are evaluated as described in the following .

The normal stress capacities (for overturning and bending failure mechanisms) are directly represented by the compressive ( $f_c$ ) and tensile resistance of the material ( $f_t$ ) already explained in section 3.3.3. In case of overturning (OVE) stress demand, the interaction between the axial load and moment is taken into account through the Navier's formula reported in Eq. 3-43:

$$\sigma_{x,D} = \frac{N_x}{A} \pm \frac{M_x}{W_x} \quad 3-43$$

In the case of horizontal bending (BEN) demand the axial load is neglected. The out-of-plane tangential stress capacity,  $\tau_{y,C}$ , has been evaluated taking into account the interaction between the axial load and tangential resistance based on the Mohr-Coulomb friction law ([Parisi et al. 2011](#)):

$$\tau_{x,C} = \frac{1}{p} \cdot (\tau_0 + \mu_a \cdot \sigma_x) \quad 3-44$$

where:  $\tau_0$  is the pure shear resistant stress of the material in absence of normal stress;  $\sigma_x$  is the normal stress acting on the element;  $p$  is the shear stress distribution factor related to the aspect ratio of the section;  $\mu_a$  is the fictitious friction coefficient of the entire masonry, which is assumed equal to 0.4 by Eurocode 6 ([CEN 2004](#)) and ([IBC 2008](#)). In order to consider also the nominal lateral strength corresponding to bed-joint sliding, it is possible to assume the term  $\mu_a$  as proposed by [Tassios \(1987\)](#) and reported in Eq. 3-45:

$$\mu_a = \frac{0.17}{\sqrt[3]{\left(\frac{\sigma_x}{f_c}\right)^2}} \quad 3-45$$

Considering both the friction coefficients, the out-of-plane tangential stress capacity can be calculated as the minimum between the bed-joint sliding shear and the masonry material sliding shear:

$$\tau_{x,C} = \min\left\{\frac{1}{p} \cdot (\tau_0 + 0.4 \cdot \sigma_x), \frac{1}{p} \cdot \left(\tau_0 + \frac{0.17}{\sqrt[3]{\left(\frac{\sigma_x}{f_c}\right)^2}} \cdot \sigma_x\right)\right\} \quad 3-46$$

The in-plane tangential capacity,  $\tau_{y,C}$ , is calculated by also considering the in-plane sliding bed joint and the in-plane sliding masonry material (as in Eq. 3-46 for the out-of-plane) with the addition of the yield criterion reported in Eq. 3-47 proposed by [Turnšek and Čačovič \(1971\)](#) in order to account the for the diagonal cracking in masonry material:

$$\tau_{y,C} = \sqrt{1 + \frac{\sigma_x}{p \cdot \tau_0}} \quad 3-47$$

where:  $\tau_0$  is shear resistant stress of the material in absence of normal stresses;  $\sigma_x$  is the normal stress acting on the element;  $p$  is the shear stress distribution factor related to the

aspect ratio of the section. Finally, the in-plane tangential stress capacity can be evaluated as reported in Eq. 3-48:

$$\tau_{y,c} = \min \left\{ \frac{1}{p} \cdot (\tau_0 + 0.4 \cdot \sigma_\tau), \frac{1}{p} \cdot \left( \tau_0 + \frac{0.17}{\sqrt{\left( \frac{\sigma_\tau}{f_c} \right)^2}} \cdot \sigma_\tau \right), \sqrt{1 + \frac{\sigma_\tau}{p \cdot \tau_0}} \right\} \quad 3-48$$

### 3.3.5 Limit states definition

The incremental analysis procedure, explained in section 3.2.4, consists in executing a certain number of structural analyses (by increasing the chosen *IM*; e.g., *flow height*) up to the reaching of a critical *IM* value corresponding to  $DCR_{LS} = 1$  for a prescribed limit state *LS*. In this work, three limit states have been considered, based on the performance levels proposed by [FEMA \(2000\)](#). In Tab. 3-5, a list of the limit states considered is reported with a description of the damage and the downtime associated.

Performance level	Damage description	Downtime
Damage control ( <i>DLS</i> )	Minor cracking; essential systems operational; minor overall damage.	Few days
Life safety ( <i>LLS</i> )	Extensive cracking and some crushing but wall remains in place.	Days/Months
Collapse prevention ( <i>CLS</i> )	Extensive cracking; noticeable in-plane and out-of-plane offsets.	Months

*Tab. 3-5: Limit states definition for structural/non-structural walls.*

The considered limit states are defined analytically herein through two limit state functions: (1) the damage control limit state function; (2) the two ultimate limit states' function (life safety and collapse prevention).

The damage control limit state function is proposed in Eq. 3-49. It is a representation of the *DCR* for the entire building based on the assumption that the damage limit state is reached when the first micro-element in the entire structure fails for one of the considered failure mechanisms:

$$DCR_{DLS} = \max_{w=1}^{N_w} \max_{i=1}^{N_i} \max_{j=1}^{N_j} \max_{m=\{O/E, B/E, S/O, S/P\}} (DCR_m^{(i,j)}) \quad 3-49$$

Where: *w* is the index identifying the walls in the building; *i* and *j* are the indexes of the elements in a given wall. The  $DCR_{DLS}$  is equal to the maximum demand to capacity ratio over all the walls, all the elements and all the considered mechanisms. When  $DCR_{DLS}$  exceeds the value 1, the damage control limit state has been reached.

Regarding the two considered ultimate limit states (denoted generically as *ULS*), the limit state function  $DCR_{ULS}$  is designed to normalize the number of failed elements (for the

entire structure) to a defined “acceptable” threshold indicated as  $p_{ULS}$  (e.g.,  $p_{ULS}=0.50$  indicates that limit state threshold is reached when half of the total number of elements in the structure have failed):

$$DCR_{ULS} = \frac{1}{p_{ULS} \cdot N_w \cdot N_i \cdot N_j} \cdot \sum_{w=1}^{N_w} \sum_{i=1}^{N_i} \sum_{j=1}^{N_j} I \left[ \max_{m=\{OVT,REN,SOP,SIP\}} (DCR_m^{(i,j)}) \right] \quad 3-50$$

Where:  $w$  is the index identifying the walls in the building;  $i$  and  $j$  are the element indices of in a wall;  $I$  is an indicator function (defined in Eq. 3-51) used to count the number of failed elements:

$$I[f] = \begin{cases} 0 & \text{if } f < 1 \\ 1 & \text{otherwise} \end{cases} \quad 3-51$$

It is to note that the two considered ultimate limit states (Life Safety and Collapse Prevention) are distinguished based on the numerical values (in terms of percentage values) adopted for the acceptable thresholds  $p_{ULS}$ . The definition of  $p_{ULS}$  thresholds for each ultimate limit state is performed on a case-specific basis in this work, as described later in the description of the case studies.



---

# Chapter 4

## HydRA: a new software for Hydrogeological Risk Analysis

*In this Chapter the software HydRA is presented. In the first part a brief introduction about the programming design and the implementation options is outlined. This is followed by a description of the implemented commands, the output elaboration and the complete user manual.*

### 4.1 Introduction

Computer programming aims at producing an executable computer process for implementing mathematical formulations and procedures (Hoare 1969). Communication of information to a computer, in a way that it can be processed and executed, becomes a reality thanks to a programming language. Programming languages can be *low-level* if they correspond closely to machine code, or *high-level* if they correspond closely to a human language. The high-level programming languages need to be compiled to be translated in machine code.

The description of a programming language is divided in two main components: the *syntax* that is the form of the language and the *semantic* that regards the meaning of the sentence. The languages can have substantial differences in terms of semantic. However, in terms of syntax, they can have only two possible formats: (1) the *imperative format*; all the procedure and functionality must be implemented as a complete sequence of operations to be performed; for instance, C++, C#, Java, Delphi, etc. (2) the *declarative format*; only the desired result, not how to achieve it, is specified; for instance, database programming using a SQL-based language.

In computer programming, the choice of a specific language is less crucial than the choice of the style of computer programming that is represented by *programming paradigm*.

There are two main programming paradigms: (1) the *procedural* one that describes, in a step-by-step manner, the exact procedure that should be followed to solve a specific problem; (2) the *object oriented* a rather unconventional and revolutionary way to program which is described in detail below.

Object oriented programming (OOP) is a programming paradigm based on the concept of *objects*, which can contain data --in the form of fields-- often known as *attributes*; and *codes* --in the form of procedures-- often known as *methods*. A feature of these *objects* is that an object procedure can access and often modify the data fields associated to the specific object. In OOP, the programs are designed to manage the relationships and the interactions between objects, in the most abstract manner possible and not in a procedure-specific manner (Pokkunuri 1989; Rumbaugh et al. 1991). This paradigm is founded on few principles that have made it successful. They are explained below and specified in brackets for a general example of a computer program used for the management of a bank.

1. *Abstraction*. A general element of a real problem to be solved with a computer program becomes a *class* that is an abstraction of the specific element. The specific element is called *object* and it is defined as an instance of its class (in a bank program: Employee, Bank, Director, Account, Client are all classes. The specific employee Mario Rossi is an instance of the class Employee).
2. *Composition and aggregation*. The objects can contain other objects in their instance variables or can have a mutual relation (i.e., the class Bank contains all the instances of the class Employees) together with their specific attributes (the class Employee can have as attributes: first name, last name, etc..) and methods (within the class Employee, possible procedures are: open an account, close an account, etc.).
3. *Encapsulation*. This principle consists in binding together the data and the functions that manipulate the data in order to keep both safe from external interferences and misuses (class Employee may modify attributes of class Account only with specific and safe methods).
4. *Inheritance*. A class can descend from a parent class inheriting all or part of the attributes and methods (Employee can descend from the class Person inheriting some attributes like first and last name).
5. *Polymorphism*. The methods or the attributes of an object can be called without considering if the specific object belongs to a class or its parent, maintaining the specificity of the attributes or methods (for the object Mario Rossi it is possible to call the method *work* and the program will automatically execute the specific function based on the fact that Mario Rossi is an instance of Director, Employee or Person).

Among various object-oriented-based languages, the Java language (Gosling 2000) has been chosen in this work for the implementation of the hydrogeological risk assessment framework. The reason of this choice is that Java language is specifically designed so that

the implementation dependencies in the application development are as few as possible. Using this language, the compiled Java code can run on all platforms that support a Java Virtual Machine (JVM) that is a simple library to be installed on the computer. This is possible because the code is not compiled in the machine code but in an intermediate bytecode interpreted by the JVM. Java is defined as a cross-platform language just because, as saying by Java developers, you can “*write once, run anywhere*”.

Java OOP seems to be perfectly suitable for a systematic implementation of the proposed framework for hydrogeological risk analysis. As result, the software HydRA for “**H**ydrogeological **R**isk **A**nalysis” has been developed. In the following sections, HydRA is presented in detail and its implementation is described through an example application.

## 4.2 HydRA description

All the theoretical concepts explained in Chapter 3, have been implemented in HydRA. All the classes, the functions and the dependencies are included in a Java archive (JAR) that is a unique package which provides the end user with the possibility of managing the fewest possible number of files.

In the current release, HydRA does not support a Graphical User Interface (GUI) and it can be executed by the shell (e.g., the command prompt in Windows, the terminal in Linux-based systems, etc.). For more advanced users, it may be interfaced with other development environments (e.g. Matlab). The choice of not having a graphical interface is motivated by the following considerations:

- *The target.* HydRA is a software addressed to researchers or expert engineers in the field of hydrogeological risk analysis. Hence, the users are particularly interested in the applicability, data control and the implementation flexibility. These goals cannot be ensured by a graphical interface that inherently limits and over-simplifies the implementation.
- *Flexibility in adding features.* Without a graphical interface, for each new implemented feature, nothing changes for the user front end; this allows a higher rapidity and flexibility in software updating and improvement.
- *Server implementation.* As written in the previous section, one of the main advantages of using Java language is to “*write once, run anywhere*” so that HydRA may be installed on a server and used from anywhere in the world through internet access to a web page. In such cases, the graphical user interface is redundant because the interface with user is provided by the web page.
- *Use as a middleware.* HydRA is not only a final destination type of software since it can be also re-arranged for analogous problem-solving purposes and included in custom-made platforms. The intended framework for HydRA allows its utilization --with the same efficiency-- both as a final-destination software or as a middleware.



Fig. 4-1: Infographic on HydRA workflow.

The key features of HydRA workflow are described in the infographic shown in Fig. 4-1: (1) The uncertainties in the parameters involved in the problem are defined through user-defined probability distributions. All the uncertain parameters are grouped in the vector  $\theta$ ; (2) For each simulation, a realization of vector  $\theta$  is generated based on the joint probability distribution of the uncertain parameters  $f_{\theta}$ ; (3) Each realization of the vector  $\theta$  represents a completely deterministic problem that can be solved by means of a structural analysis software; (4) The process is repeated up to when the desired number of simulations has reached. Finally, the analysis results are processed in the desired output format.

It is important to mention that the purpose of HydRA is not only to perform structural analyses but also to implement a complete framework for hydrogeological risk analysis. Hence, it does not aim at replacing the available structural analysis programs. In fact, HydRA does not have its own solver for the structural analysis; it rather offers an Application Programming Interface (API) for the open source interpreter OpenSees ([McKenna et al. 2006](#)). This creates independence between the solver and HydRA and provides the possibility to implement (in the future) different APIs for alternative solvers of choice. The current version of HydRA implements OpenSees because of its versatility and reliability performing structural engineering analysis (moreover, it can be used free of charge).

The required input for hydrogeological risk analysis has been accurately defined in Chapter 3, from the scientific point of view. Nevertheless, the required input for HydRA is going to be described in Section 4.3 with reference to the corresponding implementation commands. This section, which constitutes a complete user manual for HydRA platform, also provides an overview of the output and an illustrative example .

## 4.3 Command manual

### 4.3.1 Input description

All the required definitions and settings for the analysis need to included in an input file as explained in the present section. The HydRA commands have been conceived in a are defined in a simple and intuitive manner and no knowledge of programming languages is needed in order to use HydRA.

The HydRA input is divided in six sections: analysis, materials, geometry, loads, constraints, and other parameters.

In the following subsections, the HydRA commands are reported in appropriate snippets with a light grey background. To help the readers in the comprehension of the commands, 4 colours are used to highlight the different parts of the command: the comment lines (that always begin with the character #) are reported in **green** colour; the commands are reported in black colour; all the options or the types needed for each specific command are reported in **brown** colour; the numerical and the textual inputs for each command are reported in **orange** colour.

All the described commands are needed unless specific notes are provided (i.e., the commands included in angle brackets <...> are optional; the commands included in curly brackets {...} are alternative).

#### 4.3.1.1 Analysis

```
analysis $type $mode $Nsim $solverPath $outPath;
```

<code>\$type</code>	It represents the structural model type. It can be: <code>-wall</code> if the buildings vulnerability is investigated through the behaviour of two-dimensional walls; <code>-building</code> suitable for creating a three-dimensional model of the entire building. <i>N.B. the three-dimensional is more demanding in terms of computer time. Currently is under development.</i>
<code>\$mode</code>	It is a parameter that states if the uncertainty propagation is going to be performed. Currently it has only one possible string <code>-uncertainties</code> .
<code>\$Nsim</code>	Integer number of the simulations to perform.
<code>\$solverPath</code>	The complete path (without spaces) of the folder in which the solver <i>OpenSees.exe</i> is located and the temporary files will be stored during the analysis. (E.g., <i>C:\Data\Analysis\</i> ).
<code>\$outPath</code>	The complete path (without spaces) of the folder in which the results will be saved. (E.g., <i>C:\Data\Results\</i> ).

```
load -hydro -IM $imtype $a;
load -hydro -step $d;
```

<code>\$imtype</code>	This parameter defines the intensity measure used in the analysis. The options are: <code>-height</code> intensity measure is the flow height ( <code>\$a</code> is not necessary in this case); <code>-velocity</code> intensity measure is the flow velocity ( <code>\$a</code> is not necessary in this case); <code>-H V</code> intensity measure is the vector [H,V] and the flow height conditioned to the specified <code>\$a</code> value of velocity;
<code>\$d</code>	the increment of the chosen intensity measure in the incremental analysis. <i>N.B. the second command line should not be entered if the in the load definition section the time history analysis is chosen.</i>

```
limitstates $remove $pULS1 $pULS2;
```

<code>\$remove</code>	Integer number that defines if the failed elements must be removed from the model during the analysis (parameter equal to <code>1</code> ) or if they must remain in place also after their failure (parameter equal to <code>0</code> ).
<code>\$pULS</code>	It defines the “acceptable” percentage of failed elements which corresponds to the exceeding of ultimate limit states (ULS). The two possible and sequential ultimate limit state are life safety (ULS1) and collapse prevention (ULS2).

#### 4.3.1.2 Materials

```
masonry $param $dist $a1 $a2;
```

`$param` It is a qualifier for the specific mechanical property to define. The options are:

- E for the Young's modulus [N/mm<sup>2</sup>];
- gamma for the specific weight of the material [N/mm<sup>3</sup>];
- fc for the compressive strength [N/mm<sup>2</sup>];
- ft for the tensile strength [N/mm<sup>2</sup>];
- tau0 for the pure shear strength [N/mm<sup>2</sup>].

`$dist` It is a qualifier for the probability distribution which characterizes the assumed uncertain parameter in the definition of material mechanical properties. The options are:

- uniform to model a uniformly distributed parameter defined in the interval between `$a1` and `$a2` values;
- normal to model a normally distributed parameter with mean `$a1` and standard deviation `$a2`;
- lognormal to model a log-normally distributed parameter with median `$a1` and logarithmic standard deviation `$a2`;
- fixed to fix the parameter to the specific value `$a1` (deterministic).

```
<masonry -correlation $r1 $r2 $r3 $r4 $r5 $r6;>
```

`$ri` In the optional case in which a correlation structure is considered between the material mechanical properties, the parameters `$ri` represent the correlation coefficients of the symmetric correlation matrix:

$$\begin{matrix} & E & f_c & f_t & \tau_0 \\ E & \begin{bmatrix} 1 & r_1 & r_2 & r_3 \\ r_1 & 1 & r_4 & r_5 \\ r_2 & r_4 & 1 & r_6 \\ r_3 & r_5 & r_6 & 1 \end{bmatrix} & & & \\ f_c & & & & \\ f_t & & & & \\ \tau_0 & & & & \end{matrix} \quad 4-1$$

#### 4.3.1.3 Geometry

```
geometry $param $dist $a1 $a2;
```

`$param` It is a qualifiator for the specific geometrical property to define. The options are:

- length to define the wall length [mm];
- height to define the wall height [mm] (this command must be repeated for each floor);
- thickness to define the wall thickness [mm];
- <-internalspan> (optional) to define the distance between the orthogonal walls [mm] (if they are defined in the model).

`$dist` It is a qualifier for the probability distribution which characterizes the

assumed uncertain parameter in the definition of the geometry. It need to be:

- uniform to model a uniformly distributed parameter between \$a1 and \$a2;
- normal to model a normally distributed parameter with mean \$a1 and standard deviation \$a2;
- lognormal to model a log-normally distributed parameter with median \$a1 and logarithmic standard deviation \$a2;
- fixed to fix the parameter to the specific value \$a1.

```
<opening $param $dist $a1 $a2;>
```

- \$param** It is a qualifier for the specific property to define concerning the openings of the wall. It need to be:
- doorwidth to define the door width[mm];
  - doorheight to define the door height [mm],
  - windwidth to define the window width [mm];
  - windheightfb to define the distance between the bottom of the windows and the corresponding floor [mm];
  - openrate to define the number of openings rate per unit length [ $n_{\text{doors}}/m$ ];
  - doorsrate to define number of doors with respect to the number of openings [ $n_{\text{doors}}/n_{\text{openings}}$ ];
- \$dist** It is a qualifier for the probability distribution which characterizes the uncertainty in qualifier adopted for the definition of openings. The options are:
- uniform to model a uniformly distributed parameter between \$a1 and \$a2;
  - normal to model a normally distributed parameter with mean \$a1 and standard deviation \$a2;
  - lognormal to model a log-normally distributed parameter with median \$a1 and logarithmic standard deviation \$a2;
  - fixed to fix the parameter to the specific value \$a1.

#### 4.3.1.4 Loads

```
# STATIC LOADS
load $param $dist $a1 $a2;
```

- \$param** It is a qualifier for the specific load property to define. It consists of:
- floor to define the unitary load applied to the floor [N/mm] (this command should be repeated for each floor);
  - floorSpan to specify the span of the floor system [mm];
  - floorRate to specify the ratio of load-bearing walls to those that are not load-bearing [-];
- \$dist** It is a qualifier for the probability distribution which characterizes the uncertainty in the definition of the static loads. The options are:
- uniform to model a uniformly distributed parameter between \$a1 and \$a2;
  - normal to model a normally distributed parameter with mean \$a1 and



standard deviation `$a2`;  
`-lognormal` to model a log-normally distributed parameter with median `$a1`  
and logarithmic standard deviation `$a2`;  
`-fixed` to fix the parameter to the specific value `$a1`.

```
# FLOW SPECIFIC WEIGHT [N/mm³]
load -gammaflow $dist $a1 $a2;
```

`$dist` It is a qualifier for the probability distribution which characterizes the uncertainty in the definition of the flow specific weight. The options are:  
`-uniform` to model a uniformly distributed parameter between `$a1` and `$a2`;  
`-normal` to model a normally distributed parameter with mean `$a1` and standard deviation `$a2`;  
`-lognormal` to model a log-normally distributed parameter with median `$a1` and logarithmic standard deviation `$a2`;  
`-fixed` to fix the parameter to the specific value `$a1`.

```
# HYDRAULIC COMPONENTS DEFINITIONS
load -hydro -rate $stat $dyna;
```

`$stat` It is a coefficient between 0 and 1 to define the percentage of the hydrostatic component to consider in the analysis.  
`$dyna` It is a coefficient between 0 and 1 to define the percentage of the hydrodynamic component to consider in the analysis.

```
# HYDRODYNAMIC LOADS DEFINITION: CASE OF INCREMENTAL ANALYSIS
load -hydrodynamic $param $dist $a1 $a2;
```

`$param` It is a qualifier for the specific hydrodynamic load property to define. It should be:  
`-drag` to define the hydraulic drag coefficient;  
`-azimuth` to specify the angle between the North direction and the flow direction (it is measured in clockwise radiant);  
`-friction` to specify the transfer percentage of the tangential components of hydraulic loads on the walls.

`$dist` It is a qualifier for the probability distribution which characterizes the assumed uncertain parameter in the definition of the hydrodynamic load. It need to be:  
`-uniform` to model a uniformly distributed parameter between `$a1` and `$a2`;  
`-normal` to model a normally distributed parameter with mean `$a1` and standard deviation `$a2`;  
`-lognormal` to model a log-normally distributed parameter with median `$a1` and logarithmic standard deviation `$a2`;  
`-fixed` to fix the parameter to the specific value `$a1`.

```
# HYDRODYNAMIC LOADS DEFINITION: ADD THIS COMMANDS IN CASE OF INCREMENTAL
ANALYSIS WITH -IM EQUALS TO -height or -velocity
load -hydrodynamic -a $dist $a1 $a2;
load -hydrodynamic -b $dist $a1 $a2;
OR
load -hydrodynamic -normBivariateAB $muLogA $stdLogA $muB $stdB $ro;
```

- `-a, -b` The two parameters which define the power law relation that binds the velocity to the height. If the chosen intensity measure is the flow height, the power law is  $v=a \cdot h^b$ , otherwise it is  $h=a \cdot v^b$ .
- `$dist` Is a qualifier for the probability distribution which characterizes the uncertainty in the definition of the velocity-to-height power law. The options are:
- `-uniform` to model a uniformly distributed parameter between `$a1` and `$a2`;
  - `-normal` to model a normally distributed parameter with mean `$a1` and standard deviation `$a2`;
  - `-lognormal` to model a log-normally distributed parameter with median `$a1` and logarithmic standard deviation `$a2`;
  - `-fixed` to fix the parameter to the specific value `$a1`.
- `-normBivariateAB` It is used to specify a normal bivariate distribution that characterizes the jointly normal distribution for the two parameters *a* and *b* of the previously defined power law. `$muLogA` is the logarithmic mean of the parameter *a*; `$stdLogA` is the logarithmic standard deviation of the parameter *a*; `$muB` is the mean of the parameter *b*, `$stdB` is the standard deviation of the parameter *b*, `$ro` is the correlation coefficient between *a* and *b* (Note that if *a* and *b* are jointly Lognormally distributed, the same command can be used substituting *a* and *b* with their natural logarithms).

```
# HYDRODYNAMIC LOADS DEFINITION: CASE OF TIME HISTORY ANALYSIS
load -timehistory $file;
```

- `$file` It is the complete path to a text file that describes the time history of the hydrogeological load. The file must be organized in three columns separated by semicolon (;); the first one represents the height of the flow; the second one is the velocity of the flow; the third one is the azimuth of the flow. Each line of the file is a step of the time history analysis.

```
# WATERBORNE DEBRIS IMPACT
load -impact $param $dist $a1 $a2;
```

- `$param` It is a qualifier for the specific impact load property to define. It needs to be:
- `-mass` to define the mass of the flow-borne debris [kg];
  - `-time` to specify the duration of the impact necessary to evaluate the impact force [seconds].
- `$dist` It is a qualifier for the probability distribution that characterizes the

uncertainty in the definition of the impact load. It needs to be:

- uniform to model a uniformly distributed parameter between \$a1 and \$a2;
- normal to model a normally distributed parameter with mean \$a1 and standard deviation \$a2;
- lognormal to model a log-normally distributed parameter with median \$a1 and logarithmic standard deviation \$a2;
- fixed to fix the parameter to the specific value \$a1.

#### 4.3.1.5 Constraints definition

```
constraint $param $a1 $a2;
```

- \$param It is a qualifier for the specific constraint property to define. It can be:
- lateral to define the lateral constraint condition of the walls. \$a1 is the probability that the sides of the walls are constrained and \$a2 is the wall limit form ratio (wall length divided by wall thickness): for form ratio values lower than \$a2 the section is clamped, for higher values the section is hinged.
  - floors to define the constraint produced by the floor. \$a1 is the probability that the floor provides constraint.

#### 4.3.1.6 Other definitions

```
mesh $a1 $a2;
```

- \$a1 The horizontal mean dimension of the shell element which is used to build the wall [mm].
- \$a2 The vertical mean dimension of the shell element which is used to build the wall [mm].

```
<dxfr -save;>
```

This command creates a dxf output file of the 3d model of the wall for each simulation in order to check the geometry. It is very useful in three-dimensional analysis.

```
<hazard -k $k0value $kvalue;>
```

This command defines the hazard curve assuming that it depends only on the \$k0value and \$kvalue values (see the section 3.2.5).

### 4.3.2 Outputs description

The output provided by HydRA can be classified into *global results* and *simulation results*.

The global results are stored in two different formats: a *results.mat* file (ready to be used

in Matlab) and a text file *results.txt*. The content of the two files is described in the Tab. 4-1. All the variables can refer to the different limit states by replacing the symbol \$ by dls, uls1 and uls2 for Damage Limit State and the two possible Ultimate Limit States, respectively.

Variable name	Description
eta_\$_	The median of the robust fragility curve. It is expressed in meters if the chosen intensity measure is the flow height or in meters/second if the chosen intensity measure is the velocity.
beta_\$_	The logarithmic standard deviation of the robust fragility curve.
FC_\$_	The factored capacity based on the fragility curve and a defined hazard curve. It is expressed in meters if the chosen intensity measure is the flow height or in meters/second if the chosen intensity measure is the velocity.
FCu_\$_	The factored capacity (that considers also the epistemic uncertainties in the estimation of the fragility curve parameters) based on the fragility curve and a defined hazard curve. It is expressed in meters if the chosen intensity measure is the flow height or in meters/second if the chosen intensity measure is the velocity.
FC_beta_\$_	The logarithmic standard deviation of the fragility curve obtained using the 16 <sup>th</sup> and 84 <sup>th</sup> percentiles.
FC_betaU_\$_	The logarithmic standard deviation of the fragility curve obtained using based on the logarithmic (horizontal) distance between the plus/minus one standard deviation fragility curves evaluated at the median of the robust fragility
IMcr_\$_	It is a one-dimensional array with its number of elements equal to the number of simulations. Each element represents the value of the critical intensity measure for that simulation.
criticalMech	It is a one-dimensional array with its number of elements equal to the number of simulations. Each element represents the type of the critical mechanism for that simulation.
FRAG_\$_	It is a bi-dimensional array with 4 columns and 10000 rows. The first column contains an increasing abscissa in terms of chosen intensity measure. The third column contains the ordinate of the mean fragility curve. The second and the fourth column contain the mean fragility curve plus and minus one logarithmic standard deviation, respectively.

*Tab. 4-1: Global results description.*

The simulations results, instead, are reported in two files created for each simulation. The first one is stored as *sim\_i.mat* where *i* is the reference simulation; the second one is stored as *sim\_i.dxf* only if required by user in the input file and it contains a complete three-dimensional model of the structure which is analysed in the reference simulation *i*. The files *sim\_i.mat* contain a data structure and an array of data structures for each wall of the analysed structure. The description of all the fields stored in the simulation results is reported in Tab. 4-2 and Tab. 4-3.

Structure	Field	Description
W#_IAC	Ydls	The bi-dimensional array of the incremental analysis curve. It is

(# is the wall number)	Ydls_ove	composed of two columns and a variable number of rows. The first column contains the increasing abscissa in terms of intensity measure used during the analysis and the second column contains the corresponding maximum demand on capacity ratio for the wall # at the Damage Limit State (Ydls) and also for the four considered mechanisms separately (Ydls_ove, Ydls_ben, Ydls_sip, Ydls_sop).
	Ydls_ben	
	Ydls_sip	
	Ydls_sop	
	Yuls1	The bi-dimensional array of the incremental analysis curve. It is composed of two columns and a variable number of rows. The first column contains the increasing abscissa in terms of intensity measure used during the analysis and the second column contains the corresponding maximum demand on capacity ratio for the wall # at the two Ultimate Limit States (Yuls1, Yuls2) and also for the four considered mechanisms separately (Yuls1_ove, Yuls1_ben, Yuls1_sip, Yuls1_sop, Yuls2_ove, Yuls2_ben, Yuls2_sip, Yuls2_sop).
	Yuls1_ove	
	Yuls1_ben	
	Yuls1_sip	
	Yuls1_sop	
	Yuls2	
	Yuls2_ove	
	Yuls2_ben	
	Yuls2_sip	
	Yuls2_sop	

Tab. 4-2: Description of simulations results: the incremental analysis curve.

Array	Structure	Field	Description
W#_RES (# is the wall number)	A group of fields for each shell element of the wall	id	Identification number of the considered shell element.
		x	An array containing the X coordinate of the shell element vertices.
		z	An array containing the Z coordinate of the shell element vertices.
		sz	An array containing the mean normal vertical stress (along the Z axis) on the shell element for each load step valued as $N/A$ where $N$ is the normal vertical resultant on the shell element and $A$ is the area.
		sz_min	Arrays containing the minimum and maximum vertical (along the Z axis) stresses on the shell element for each load step value in combined compression and bending state.
		sz_max	
		sx_min	Arrays containing the minimum and maximum normal stress on the shell element for each load step in the horizontal wall direction valued in combined compression and bending state.
		sx_max	
		ty	Array containing the shear stress of the shell element for each load step in the horizontal orthogonal direction of the wall.
		tx	Array containing the shear stress on the shell element for each load step in the horizontal tangential direction of the wall.
		Mx	Array containing the bending moment on the shell element for each load step around the wall longitudinal direction.
		Mz	Array containing the bending moment on the shell element for each load step around the vertical direction.
		sz_minR	Arrays containing the minimum and the maximum normal resistant stress for each load step in the vertical direction (along the Z axis).
		sz_maxR	
sx_minR	Arrays containing the minimum and the maximum normal resistant stress for each load step in the horizontal direction of the wall.		
sx_maxR			

	<code>t<sub>yR</sub></code>	Array containing the shear resistant stress of the shell element for each load step in the horizontal orthogonal direction of the wall.
	<code>t<sub>xR</sub></code>	Array containing the shear resistant stress on the shell element for each load step in the horizontal direction of the wall.
	<code>Y<sub>sz</sub></code>	Array containing the demand to capacity ratio of the shell element for each load step in terms of combined axial and bending state in vertical direction (along the Z axis).
	<code>Y<sub>sx</sub></code>	Array containing the demand to capacity ratio of the shell element for each load step in terms of combined compression and bending state in the horizontal wall direction.
	<code>Y<sub>ty</sub></code>	Array containing the demand to capacity ratio of the shell element for each load step in terms of shear in the horizontal orthogonal direction of the wall.
	<code>Y<sub>tx</sub></code>	Array containing the demand to capacity ratio of the shell element for each load step in terms of shear in the horizontal direction of the wall.

*Tab. 4-3: Simulations results description: stresses and safety checks.*

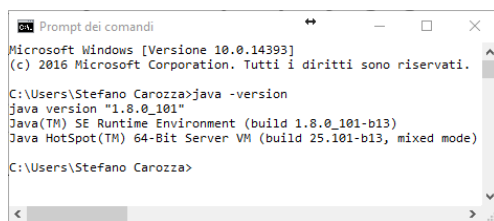
### 4.3.3 Example of usage

#### 4.3.3.1 HydRA setup

In this section, an example of how to run HydRA is illustrated. The procedure is described for a Windows operative system; however, it can be considered valid also for other operative systems with some appropriate modifications. HydRA needs two software dependencies to run (Java SE Runtime Environment and the TCL/TK language ) and in the following procedure it is explained how to check if they are already present on the system or they have to be installed.

Step 1. *Check the presence of the Java SE Runtime Environment or install it.*

Open the command prompt and type `java -version`. If the version of Java is returned it is possible to go to the next step. Otherwise, download the last version for your operative system of the Java SE Runtime Environment from the Oracle web site (<http://www.oracle.com/technetwork/java/javase/downloads/jre8-downloads-2133155.html>, last check on February 26<sup>th</sup>, 2017).



```

Microsoft Windows [Versione 10.0.14393]
(c) 2016 Microsoft Corporation. Tutti i diritti sono riservati.

C:\Users\Stefano Carozza>java -version
java version "1.8.0_101"
Java(TM) SE Runtime Environment (build 1.8.0_101-b13)
Java HotSpot(TM) 64-Bit Server VM (build 25.101-b13, mixed mode)

C:\Users\Stefano Carozza>

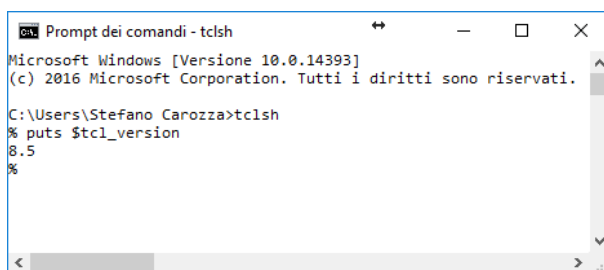
```

*Fig. 4-2: Check the version of Java SE Runtime Environment.*

Step 2. *Check the presence of the TCL/TK interpreter.*

Open the command prompt and type in sequence this two command: `tclsh` and

then `puts $tcl_version`. If the version of TCL is returned it is possible to go to the next step. Otherwise, you can download the TCL/TK interpreter from the Download section of the OpenSees web site (<http://opensees.berkeley.edu/>), last check on February 26<sup>th</sup>, 2017).



```
Prompt dei comandi - tclsh
Microsoft Windows [Versione 10.0.14393]
(c) 2016 Microsoft Corporation. Tutti i diritti sono riservati.

C:\Users\Stefano Carozza>tclsh
% puts $tcl_version
8.5
%
```

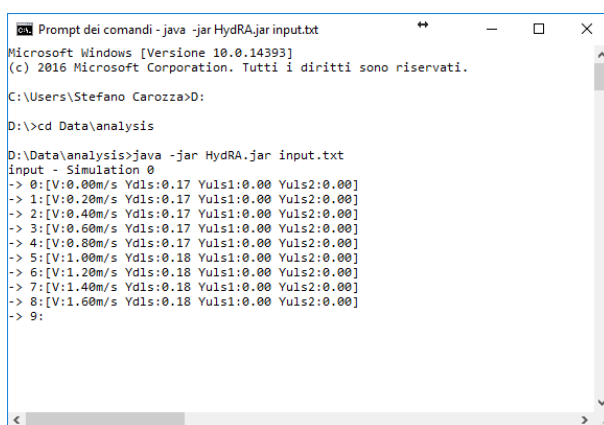
Fig. 4-3: Check the version of TCL/TK interpreter.

Step 3. *File and folders preparation.*

Create two folders, in example `D:\Data\analysis\` and `D:\Data\output\`. Put the Java archive `HydRA.jar`, the input file of the analysis (e.g., the ones named `input.txt` proposed in the section 4.3.3.2) and the OpenSees executable file `OpenSees.exe` (it is possible to download it from the same website reported in the Step 2) inside the folder `analysis`.

Step 4. *Run the analysis.*

Open the command prompt, move to the `analysis` folder and type `java -jar HydRA.jar input.txt` and see the analysis progress. At the end of the analysis, it is possible to open the output files in the `output` folders.



```
Prompt dei comandi - java -jar HydRA.jar input.txt
Microsoft Windows [Versione 10.0.14393]
(c) 2016 Microsoft Corporation. Tutti i diritti sono riservati.

C:\Users\Stefano Carozza>D:
D:\>cd Data\analysis
D:\Data\analysis>java -jar HydRA.jar input.txt
input - Simulation 0
-> 0:[V:0.00m/s Yd1s:0.17 Yuls1:0.00 Yuls2:0.00]
-> 1:[V:0.20m/s Yd1s:0.17 Yuls1:0.00 Yuls2:0.00]
-> 2:[V:0.40m/s Yd1s:0.17 Yuls1:0.00 Yuls2:0.00]
-> 3:[V:0.60m/s Yd1s:0.17 Yuls1:0.00 Yuls2:0.00]
-> 4:[V:0.80m/s Yd1s:0.17 Yuls1:0.00 Yuls2:0.00]
-> 5:[V:1.00m/s Yd1s:0.18 Yuls1:0.00 Yuls2:0.00]
-> 6:[V:1.20m/s Yd1s:0.18 Yuls1:0.00 Yuls2:0.00]
-> 7:[V:1.40m/s Yd1s:0.18 Yuls1:0.00 Yuls2:0.00]
-> 8:[V:1.60m/s Yd1s:0.18 Yuls1:0.00 Yuls2:0.00]
-> 9:
```

Fig. 4-4: Analysis progress.

#### 4.3.3.2 Example of implementation of a complete input file

The code proposed in the following example refers to a realistic analysis case. It is possible to copy and paste the code in a text file, save it as (for example) `input.txt` and use it as specified in the following section. It is worth noting that, before the use, it is necessary

to adjust the pathnames for the analysis and output folders.

```

# -----
# Object                : EXAMPLE OF IMPLEMENTATION
# Last modify           : November, 22th 2016
# Author                : Stefano Carozza (stefano.carozza@unina.it)
# Affiliation           : DiSt, University of Naples "Federico II"
# -----

# -----
# ANALYSIS DEFINITION
# -----
analysis -wall -uncertainties 50 D:\Data\analysis\ D:\Data\output\;
load -hydro -IM -V|H 1000;
load -hydro -step 500;
limitstates 1 0 0.9;

# -----
# MATERIAL DEFINITION
# -----
masonry -E -uniform 690 1220;
masonry -gamma -uniform 16.0E-6 19E-6;
masonry -fc -uniform 0.5 2.0;
masonry -ft -uniform 0.10 0.5;
masonry -tau0 -uniform 0.15 0.5;
masonry -correlation 0.4 0.4 0.4 0.4 0.4 0.4;

# -----
# GEOMETRY DEFINITION
# -----
geom -length -lognormal 5000 0.25;
geom -height -uniform 3300 4300;
geom -thickness -uniform 400 600;
geom -internalspan -uniform 4000 5000;
opening -doorwidth -uniform 1200 1400;
opening -doorheight -uniform 2000 2400;
opening -windwidth -uniform 900 1400;
opening -windheightfb -uniform 800 1100;
opening -openrate -fixed 0.25;
opening -doorsrate -fixed 0.50;

# -----
# LOADS DEFINITION
# -----
load -floor -lognormal 8.0 0.3;
load -floorSpan -uniform 4000 5000;
load -floorRate -lognormal 0.5 0.3;
load -gammaflow -lognormal 14E-6 0.1;
load -hydrodynamic -drag -uniform 1.0 1.2;
load -hydrodynamic -azimuth -uniform 0.0 1.57;
load -hydrodynamic -friction -fixed 0.5;
load -hydro -rate 1.0 1.0;

# -----
# CONSTRAINTS DEFINITION
# -----
constraint -lateral 0.5 8.0;
constraint -floors 0.5;

# -----
# OTHER DEFINITIONS
# -----
mesh 200 200;

```



#### 4.3.3.3 Analysis results

In this section, some outputs obtained running the input files specified in the section 4.3.3.2 are reported in order to show how to manage the data described in Tab. 4-2 and Tab. 4-3. The analysis results are only shown with the corresponding data output; all the scientific comments and the observations have been addressed in Chapter 3.

The analysis type is incremental, the chosen intensity measure is the flow velocity given a fixed value of the flow height equal to 1.0m and the considered limit states are the Damage Limit State (DLS) and the Collapse prevention Limit State (CLS).

The global results are reported in Tab. 4-4 for the two considered limit states.

Variable name	DLS	CLS
eta	4.958 m/s	6.526 m/s
beta	0.3582	0.3189
FC	3.755 m/s	5.257 m/s
FCu	3.754 m/s	5.230 m/s
FC_beta	0.3562	0.3172
FC_betaU	0.0492	0.0486

Tab. 4-4: The global results of the analysis.

The incremental analysis curves, reported in terms of Demand to Capacity Ratio (DCR) versus the flow velocity, resulting from the incremental analysis are plotted in Fig. 4-5 and Fig. 4-6 for the two considered limit states. Each curve is representative of a single simulation realization. The data contained the incremental curves illustrated in the figure are stored in variables denoted as  $y_{dls}$  (for Damage Limit State) and  $y_{uls2}$  (for Collapse prevention Limit State) contained in the data structure  $w0\_IAC$  (stored in simulation results' mat files).

The small circles in Fig. 4-5 and Fig. 4-6 represent the critical values of the intensity measure (stored in the variables  $im_{cr\_dls}$  and  $im_{cr\_uls2}$ ). To visualize the variability in the critical values obtained for each simulation realization, the probability density functions of the fragility curves for the two limit states are plotted.

Fig. 4-7, instead, shows the (robust) fragility curves for the two considered Limit States (in solid lines) and the robust fragility plus/minus one logarithmic standard deviation (in dashed lines) curves. The figure also reports the values of the factored capacity (with  $F_{cu}$  and without  $F_c$  consideration of epistemic uncertainties). In this example,  $F_c$  and  $F_{cu}$  are very close (because of the narrow confidence interval: the distance between the robust fragility and the dashed curves) so that in Fig. 4-7 the circles corresponding to  $F_c$  and  $F_{cu}$  for both limit states are almost overlapped.

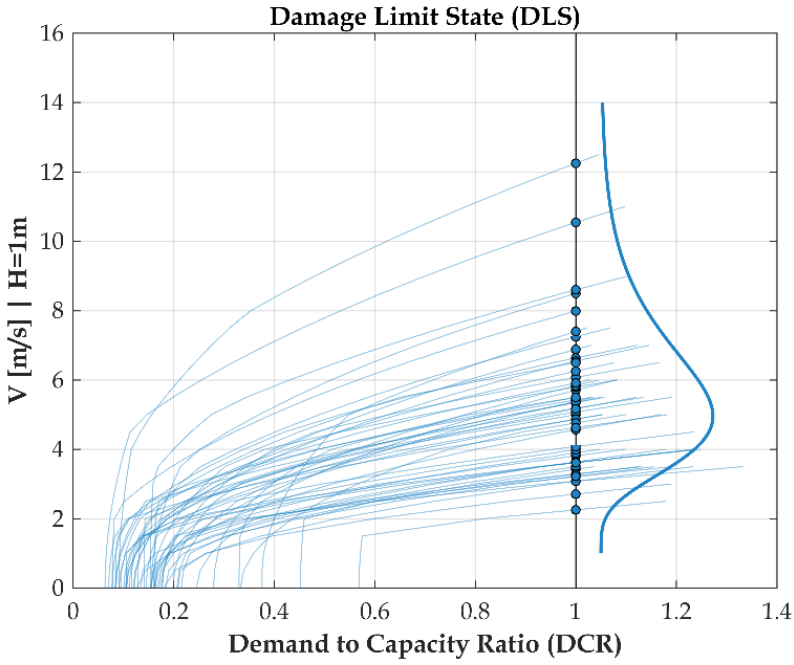


Fig. 4-5: Incremental analysis curves for the DLS.

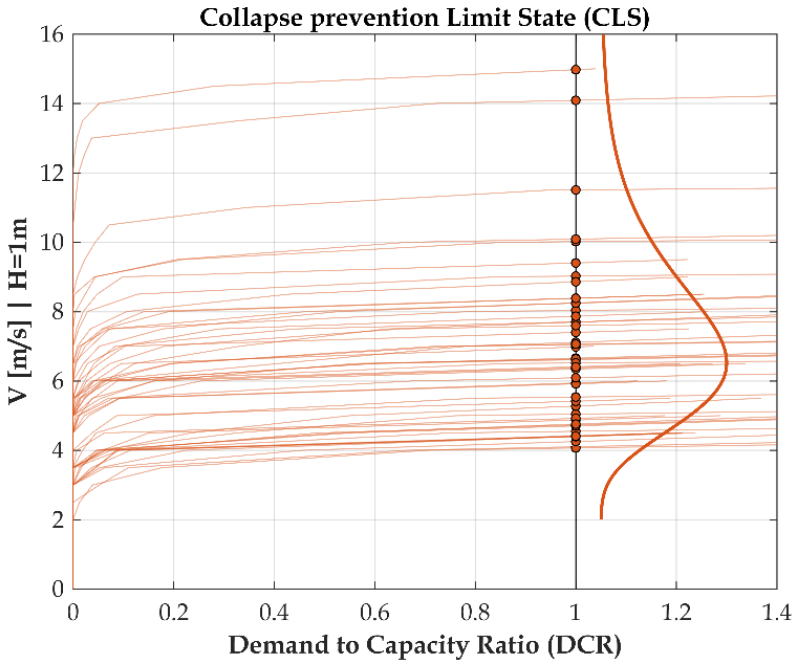


Fig. 4-6: Incremental analysis curves for CLS.

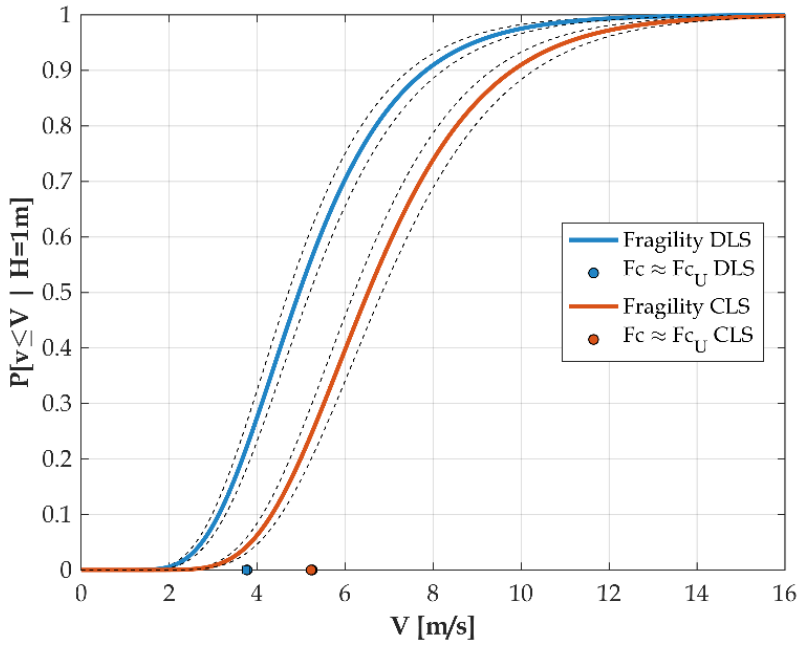


Fig. 4-7: Fragility curves for the two considered Limit States.

Using the data stored in the variable `w#_RES`, it is possible to plot at each analysis step and for each simulation realization, the demand stresses, the capacity stresses and the demand to capacity ratios. Just as an example, in Fig. 4-8 DCRs for the wall corresponding to the simulation #2 at the analysis step #1 are plotted.

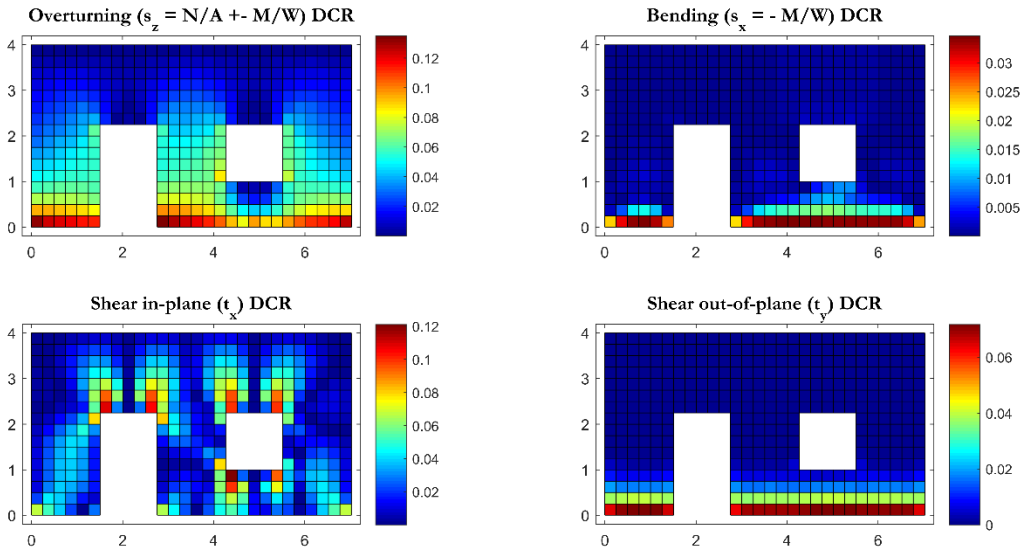


Fig. 4-8: Demand to Capacity Ratio (DCR) for the simulated wall #2 at step #1 of analysis ( $H = 1.0m - V = 0.0m/s$ ).



---

# Chapter 5

## Framework applications

*In this Chapter, the entire framework has been illustrated based on three case-study applications: (1) Structural analysis for a single masonry building in Scaletta Zanclea damaged in the debris flow event of 2009 where the results of the analysis are compared with the observed damage pattern; (2) Portfolio damage assessment for the Episcopio district (Sarno) that suffered severe destruction and damage in the debris flow event of 1998 where a visual comparison with the observed damage on the portfolio of buildings has been drawn; (3) An application of the proposed framework for risk assessment for Castellammare di Stabia in order to provide the risk maps as an instrument in the support of hydrogeological risk management.*

### 5.1 Debris flow damage incurred to a real building: an in situ back analysis

In an attempt to conduct a back analysis of the damage caused to a 19<sup>th</sup> century masonry structure due to the October 2009 flash flood/debris flow event in Scaletta Zanclea, a flood discharge hydrograph is reconstructed in the ungauged conditions. The hydrograph for the solid discharge is then estimated by scaling up the liquid volume to the estimated debris volume. The debris flow diffusion is simulated by solving the differential equations for a single-phase two-dimensional (2D) flow that employs triangular mesh elements, also taking into account the channelling of the flow through the buildings. The damage to the building is modelled using 2D finite shell elements implemented in the platform HydRA and is based on the maximum hydraulic action caused by the debris flow. The boundary conditions provided by the openings, floor slabs, orthogonal wall panels and the foundations are also modelled (see [Jalayer et al. \(2016\)](#), the analysis of the hydrographic basin, characterization of the hydrograph and the 2D diffusion of the flow has been performed by Prof. Giuseppe T. Aronica).

The event of the October 2009 has been described in Section 1.6.1 so that, in the following subsections, only the back analysis study has been addressed.

### 5.1.1 Debris flow actions reconstruction

Given the lack of discharge measurements (as no flow gauge was located within the Racinazzi catchment area for the reconstruction of the flood hydrograph), a simple lumped rainfall-runoff model based on a Kinematic Instantaneous Unit Hydrograph (IUH) has been used for flood routing and the Soil Conservation Service-Curve Number (SCS-CN) method implemented on the basis of the ‘time dependent’ formulation (Chow et al. 1988) for runoff generation (Aronica et al. 2012). The Kinematic IUH was calculated using the time–area curve derived for the catchment based on the digital elevation model and a value of the concentration time equal to 40 min from the Wooding formula for a single plane. Land use maps from the Corine project and soil type maps were available, allowing us to derive a lumped value of  $CN = 80$  for the highly saturated conditions ( $AMC = III$ ) used for the simulations.

The solid discharge hydrograph was simply derived by rescaling the liquid volume to the estimated debris volume using the Takahashi amplification coefficient (Takahashi 1991).

Post-event analyses and a comparison with similar events in a catchment close to Racinazzi (Aronica et al. 2012) led to an estimation of the solid debris volume of around  $0.54 \text{ Mm}^3$ . Now, by considering an equilibrium solid concentration of 0.45, the resulting mixture volume was around  $1.2 \text{ Mm}^3$ , and the Takahashi amplification coefficient was equal to 4.5. The resulting hydrographs are reported in Fig. 5-1.

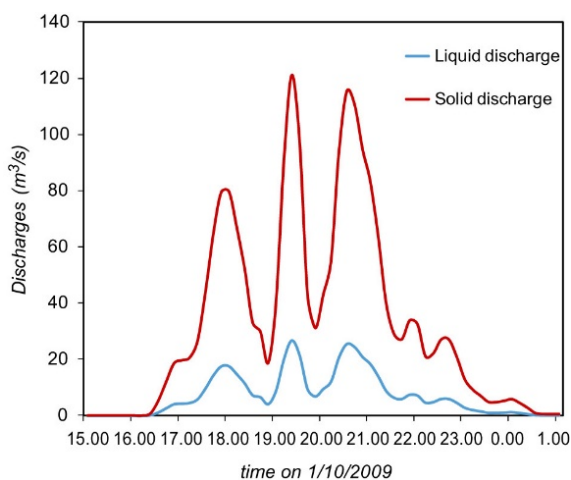
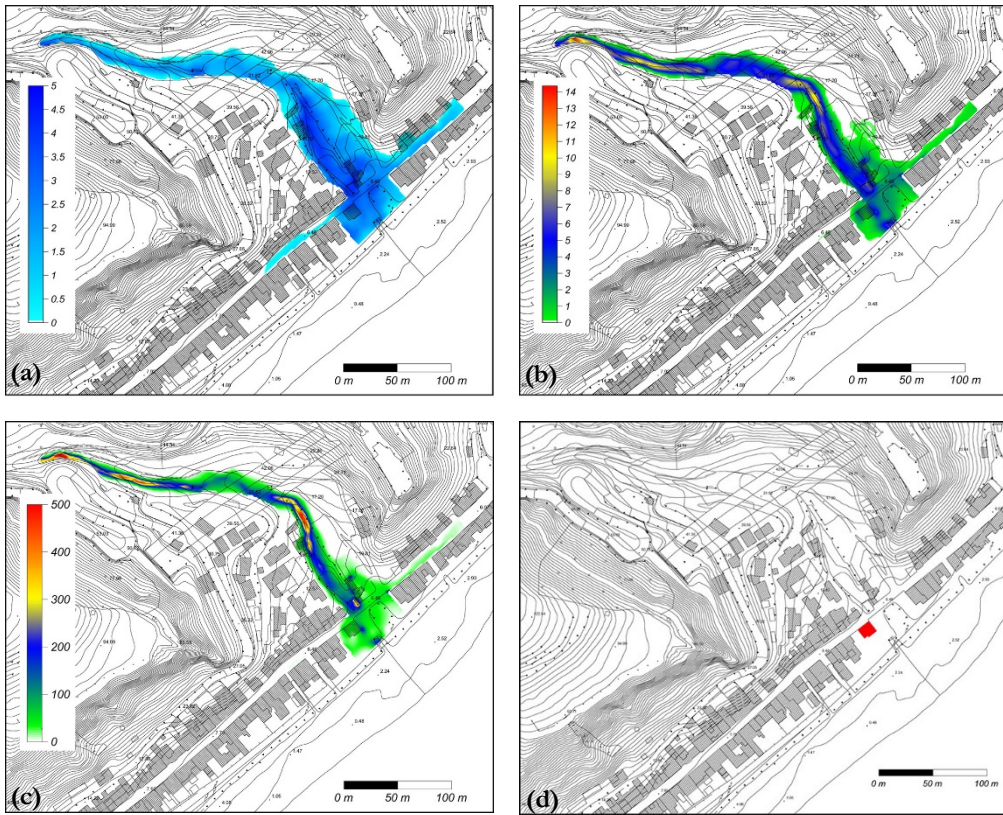


Fig. 5-1: Reconstructed liquid and solid flood hydrograph.

To simulate the propagation of the debris flow on the alluvial fan, a hyperbolic single-phase fluid model in 2D form was used (Aronica et al. 2012). This model is based on the De Saint Venant equations and is capable of simulating the 2D flow of a single-phase fluid by considering a different set of equations for modelling friction terms instead of the classic Chèzy formula. The detailed description of the propagation is not the scope of this section and it is addressed in Jalayer et al. (2016). Only the results are reported in Fig. 5-2.



*Fig. 5-2: Maps of: (a) maximum flow depths, colour scale in meters; (b) maximum flow velocity modules, colour scale in m/s; (c) maximum total hydrodynamic force for unit width, colour scale in kN/m; (d) identification of the case study building (Jalayer et al. 2016)*

### 5.1.2 Structural model and analysis

To characterise the mechanical parameters of the masonry, as used for calibrating the FEM structural model, the results of experimental tests made on analogous buildings built at the same time and with the same technology has been used. For the data that was not obtained by the experimental tests, the indications of the Italian National Standards and the literature have been considered. In particular, a compression test was carried out on a  $1.0\text{m}$  wide masonry panel. A series of steel elements were interposed in the middle of the panel and connected on both faces of the wall to two metallic plates, which were positioned over the RC beam on a bed of mortar by four dywidag bars. Two hydraulic jacks were interposed between the metallic plates (Fig. 5-3). Each side of the upper half of the panel was instrumented with three vertical transducers. A horizontal transducer was positioned at the centre line of both faces of the upper half of the panel. The test was destructive and consisted of several cycles of loading and unloading by increasing the maximum values of the vertical compression load (Spinella et al. 2014).



*Fig. 5-3: Test set-up for the panel in compression.*

The experimental tests provided the unit weight  $w = 20 \text{ kN/m}^3$  and the compression strength capacity  $\sigma_c = 0.89 \text{ MPa}$ . For the other parameters, the Italian National Technical Standards and Guidelines were utilised by using the classification for the compression strength capacity and the typological shape of the masonry. The shear strength is conservatively assumed to be equal to  $\tau_0 = 0.1 \text{ MPa}$  (according to [IBC \(2008\)](#), for masonry walls with  $\sigma_m < 7.5 \text{ MPa}$ ), the Young's modulus is equal to  $E = 690 \text{ MPa}$  and the shear modulus is equal to  $G = 230 \text{ MPa}$ .



*Fig. 5-4: Building before and after the event of October 2009.*

In order to model the damage to the building in question due to debris flow, the portion of the building that was more exposed to the flow was separated and modelled as a three-dimensional (3D) substructure using the software platform HyDRA (Fig. 5-5), with a rectangular mesh discretisation with (average) dimensions  $250 \times 250 \text{ mm}$ . The thickness of the wall is equal to  $750 \text{ mm}$ . Fig. 5-4 shows the damaged wing in the building, which is separated as a 3D substructure and modelled using elastic shell elements (Fig. 5-5(b)). As can be seen in Fig. 5-4, the intact structure shows a small dependence in correspondence



with the eastern wall. We have not modelled this small structure because it appears to have been built at a different time than the rest of the structure, and its connection to the primary structural system of the building was not guaranteed. It appears to have been swept away by the tangential component of the dynamic forces exerted by the flow. Fig. 5-5 (c) and (d) demonstrates the geometric configuration of the two exposed faces of the building analysed herein, with the exact position of the doors and the openings.

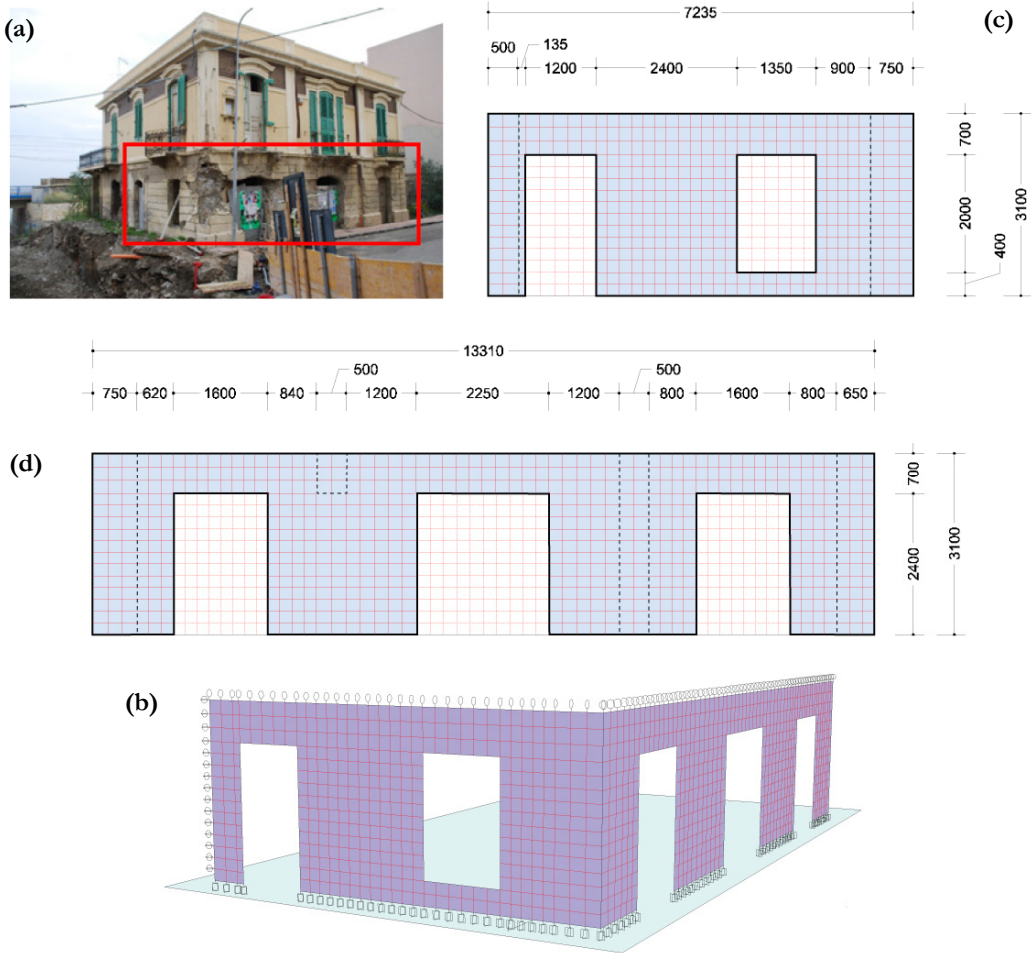


*Fig. 5-5: (a) the damaged wing modelled in HyDRA; (b) the three-dimensional substructure modelled in the fine elements; (c) the geometric configuration of the eastern wall; (d) the geometric configuration of the northern wall.*

As can be seen in Fig. 5-5(b), the nodes in the bottom base are fixed. The nodes in the upper part of the panel are blocked only against the out-of-plane rotation (in order to consider the effect of the RC floor). The 3D substructure shown in Fig. 5-5(b) is cut in correspondence with the internal orthogonal walls (cannot be seen in the figure). Therefore, considering the thickness of the walls (750 mm), it has been assumed that the orthogonal walls provide sufficient stiffness against in-plane (with respect to the orthogonal wall)

translation. This effect has been taken into account by modelling the internal wall thickness by finite elements (three lines of  $250 \times 250$  mm shell elements) and locking the in-plane translation of the nodes for the interested shell elements.

It should be noted that, in general, the nodes that draw the foot-print of the orthogonal walls on the considered wall panel (shown by the dashed thick line in Fig. 5-5 (c) and (d)) are locked against the translation of the direction of the orthogonal walls. For the northern face, it can be seen that one of the dashed lines is discontinuous. This signals the presence of a door in correspondence with the intersection with the northern face. In this case, the shell elements are interrupted, and the stiffness provided by the orthogonal door is not considered. It should be noted that the stiffness provided by the orthogonal walls against out-of-plane displacement is neglected herein. It is also worth mentioning that this model depicts the local damage caused by the flow. Generally speaking, the consequences of an eventual local reduction/loss in load-bearing capacity (in correspondence with the damaged wall panel) for the overall stability of the building should also be evaluated. The structural analyses are based on the hypothesis that the openings (doors and windows) have remained closed during the flow. The reactions due to the debris flow are applied as forces to the sides of the door and windows (assuming that the door is infinitely rigid and that the connections to the wall panel are not going to fail). This hypothesis is only partially true; that is, the openings were probably closed at the beginning (given that the event took place after midnight), but the evidence suggests that they were washed away during the event. It is noteworthy that this hypothesis is conservative with respect to the alternative hypothesis that the doors and windows were left open. In the latter case, the hydrostatic forces will be applied to both sides of the wall due to the fact that the flow will infiltrate and fill the building's interior space. The analyses are conducted by (conservatively) considering the hydrodynamic forces exerted parallel to the wall panel. On the other hand, the effect of the accidental impact of the flow-borne large objects (i.e. cars, big stones and trees) is not considered (see the related paper by [Soleimankhani et al. \(2016\)](#) where the accidental impact of the flow-borne debris has been modelled on the three-dimensional SAP model of the entire structure).

The load conditions considered for the case study wall are composed of two main load categories: dead loads and debris flow loads. Along with self-weight being considered distributed for each shell element, the following distributed loads are taken into account:  $15 \text{ kN/m}$  of floor weight (that includes structural, non-structural and live loads);  $36 \text{ kN/m}$  in order to consider the weight of the upper wall panel; and  $8 \text{ kN/m}$  in order to consider the weight of the roof.

The maximum debris-flow actions are obtained through the analysis procedure described in the previous section. In fact, as depicted in Fig. 5-2, the propagation of the debris flow by means of finite elements provides the depths, velocity modules and phases for each element in the mesh. Assuming a linear profile for the hydrostatic component and

a constant (over height) hydrodynamic profile, the total forces exerted on the exposed walls can be evaluated from Eq. 5-1 where:  $u$  and  $v$  are the two orthogonal horizontal components of the debris flow velocity vector;  $h$  is the depth of the flow; and  $\rho_m$  is the density of the solid-liquid mixture, in this case, about  $1742.5 \text{ kg/m}^3$ .

$$S_{tot} = \rho_m \cdot h \cdot (u^2 + v^2) + \frac{1}{2} \cdot \rho_m \cdot g \cdot h^2 \tag{5-1}$$

Fig. 5-6(a) and (b) demonstrates the footprint of the flow depth envelope on both of the exposed walls in the building. Fig. 5-6(c) shows the graphical scheme of the hydrostatic and hydrodynamic debris load profiles on an exposed wall.

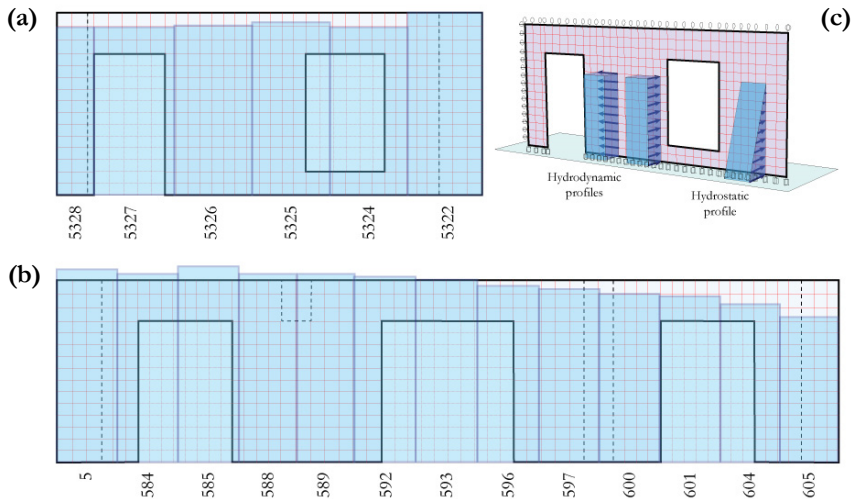


Fig. 5-6: (a) the footprint of the debris flow (the maximum depth) on the eastern wall (W2); (b) the footprint of the debris flow on the northern wall (W1); (c) hydrostatic and hydrodynamic force component profiles over the height of the wall

### 5.1.3 Structural response and damage pattern comparison with analysis results

Based on the geometric and mechanical model described in the previous section, a linear incremental analysis is performed with the presented software HyDRA to evaluate the stress distributions in the wall panel. The response parameter used for monitoring the damage to the wall panel is the demand to capacity ratio DCR as explained in Chapter 3.

The analysis is performed considering the flow height as the intensity measure (IM) of the problem (which is incremented during the analysis) and the velocity modulus is assumed constant and equal to  $5 \text{ m/s}$  (as it shown in Fig. 5-5b). The velocity direction has been calculated for several points of the building and a mean value, equal to  $60^\circ$ , is assumed in order to define the inclination of the hydrodynamic actions. In Fig. 5-7, a schematization of the analysed substructure and the footprint of the velocity profile is reported.

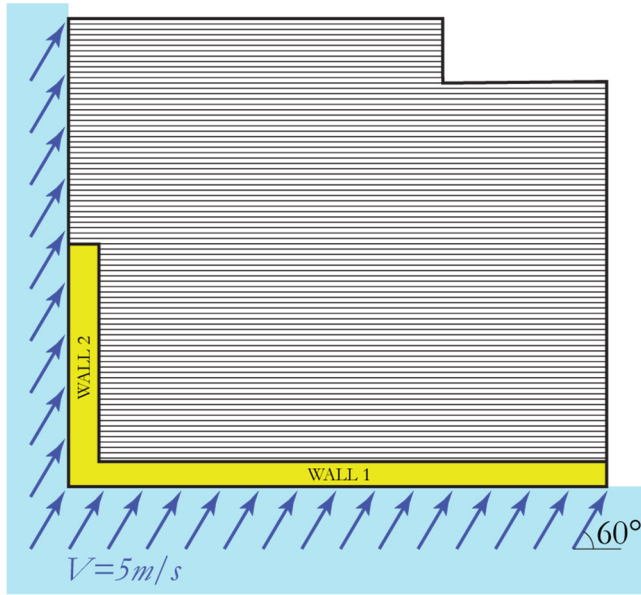


Fig. 5-7: Footprint of the velocity distribution on the modelled walls.

The results of the incremental structural analysis performed over the substructure are reported in Fig.5-8; where each incremental analysis curve represents the critical demand to capacity ratio DCR with respect to the incremental height  $H$  for the wall 1 (in dashed line) and the wall 2 (in continuous line), separately. Four different colours are used to distinguish between the different mechanisms: yellow for overturning; orange for bending; blue for in-plane shear and violet for out-of-plane shear.

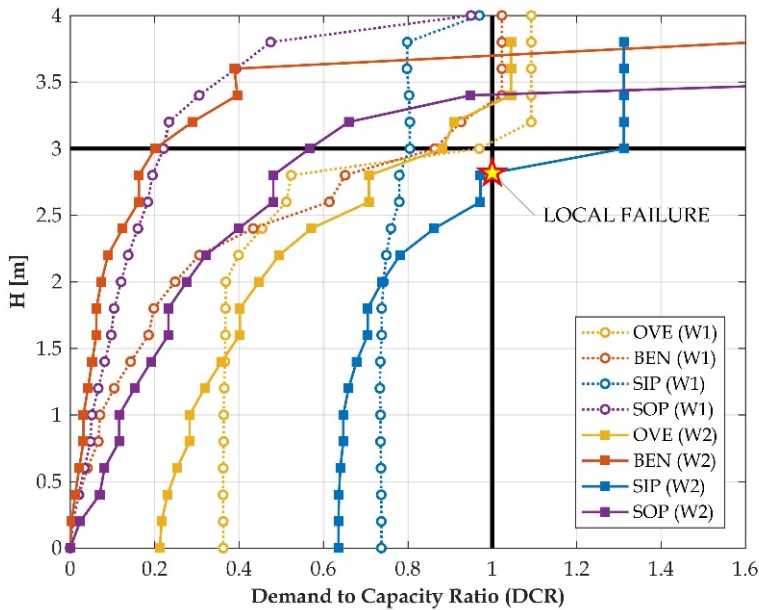


Fig. 5-8: Incremental analysis curves for the modelled substructure ( $V_{low}=5m/s$ ).

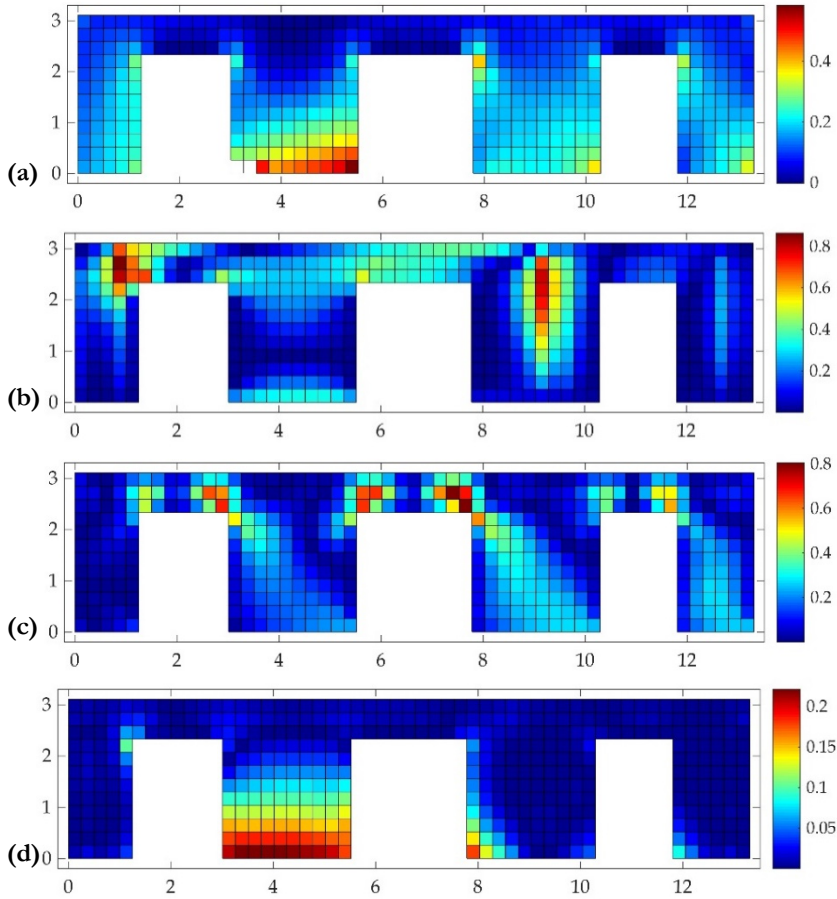


Fig. 5-9: DCR of the wall W1 ( $H_{flow}=3m$  and  $V_{flow}=5m/s$ ) for the mechanisms: (a) overturning; (b) bending; (c) shear in-plane; (d) shear out-of-plane.

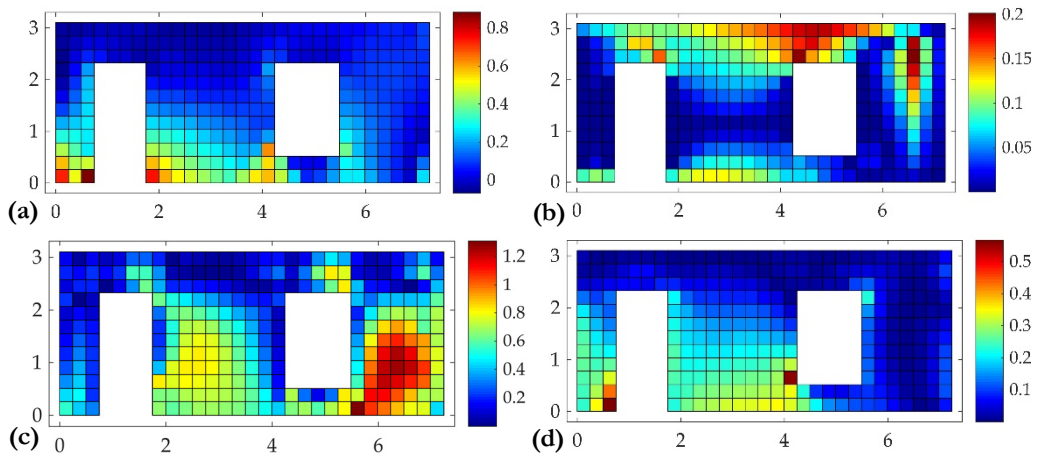


Fig. 5-10: DCR of the wall W2 ( $H_{flow}=3m$  and  $V_{flow}=5m/s$ ) for the mechanisms: (a) overturning; (b) bending; (c) shear in-plane; (d) shear out-of-plane.

In Fig. 5-8, the height of 3 meters is highlighted because it represents (on average) the

maximum observed height of the flow. As it is shown in the figure, the only curve that exceeds the threshold  $DCR=1$  before the maximum height of  $3m$  is the in-plane shear mechanism for wall 2.

The  $DCR$  distribution distinguished per mechanism is reported in Fig. 5-9 (for wall 1) and in Fig. 5-10 (for wall 2) for the analysis step corresponding to a flow height of  $3m$ .

It can be observed that the wall 1 remains in the safe zone, although some parts are close to the failure surface (bending mechanisms  $DCR = 0.96$ , Fig. 5-9b). However, the wall 2 shows that the panel to the right of the window crosses the failure surface for in-plane bending. It can be observed that the model is reasonably capable of indicating where and how the walls starts to have problems due to stress concentrations.

The results in terms of the in-plane shear (wall 2) and bending (wall 1)  $DCR$  are visually compared with the damage observed after the debris flow. Fig. 5-11 highlights the visual signs of damage with the damage pattern in the finite-element model. It can be seen that this model manages to capture the in-plane shear failure in the rightmost panel of the wall 2 and also the damage signs in correspondence with the door corner of the wall 1. The figure demonstrate that the observed damage state is congruent with the results of the FEM analysis (as much as the approximated model can be). The damage pattern observed in the walls, apart from being a direct result of the exceptional hydraulic forces exerted by the flow and the poor mechanical properties of the masonry, is also dictated by the configuration of the openings (as the weak points) in the walls.

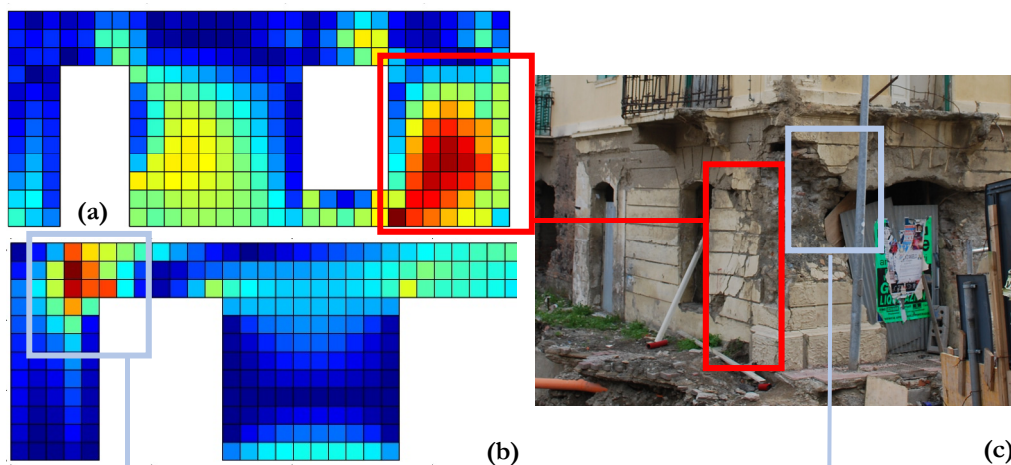


*Fig. 5-11: Comparison between the analysis results in terms of shear in-plane  $DCR$  of wall 2 (a) and bending  $DCR$  of wall 1 (b) with respect to the observed damage (c).*

The reasonable agreement between the observed damage pattern and the one obtained based on the structural analysis provides evidence in favour of both the physical model(s) used for the propagation of the flow and the finite element model (and mechanical material properties) used to depict the exposed substructure. It is particularly interesting to observe

that the analytical model and the estimated material properties manage to provide an accurate picture of the local damage incurred to the building.

The observed results also underline the importance of the accurate prediction of the hydrogeological induced loads (e.g. depth, velocity, direction of the flow) in guaranteeing appropriate damage prediction. Furthermore, methods and procedures like the ones presented herein for rapid and complex phenomena, like debris flow events, underline the importance of a fully integrated physical vulnerability assessment that provides an interface between hydraulic/hydrological/geotechnical models for the characterisation of the flow and mechanical models for the characterisation of the built environment.

## 5.2 Sarno: Portfolio damage analysis due to the 1998 debris flow disaster

### 5.2.1 Debris flow actions modelling

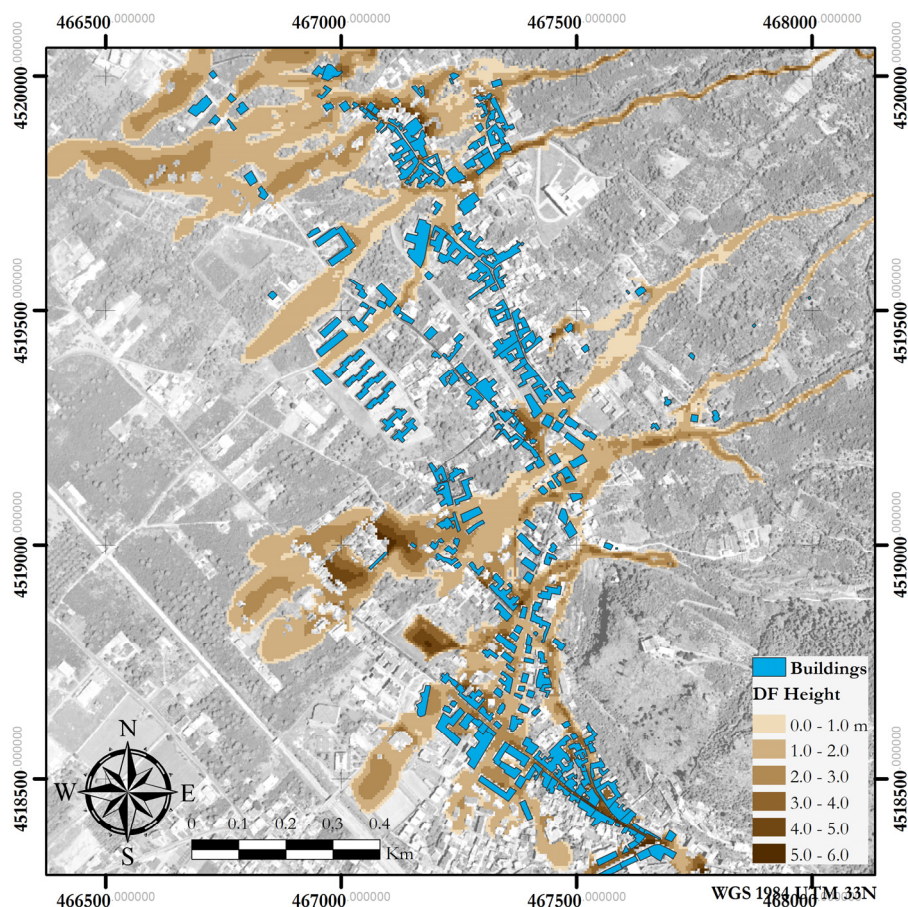
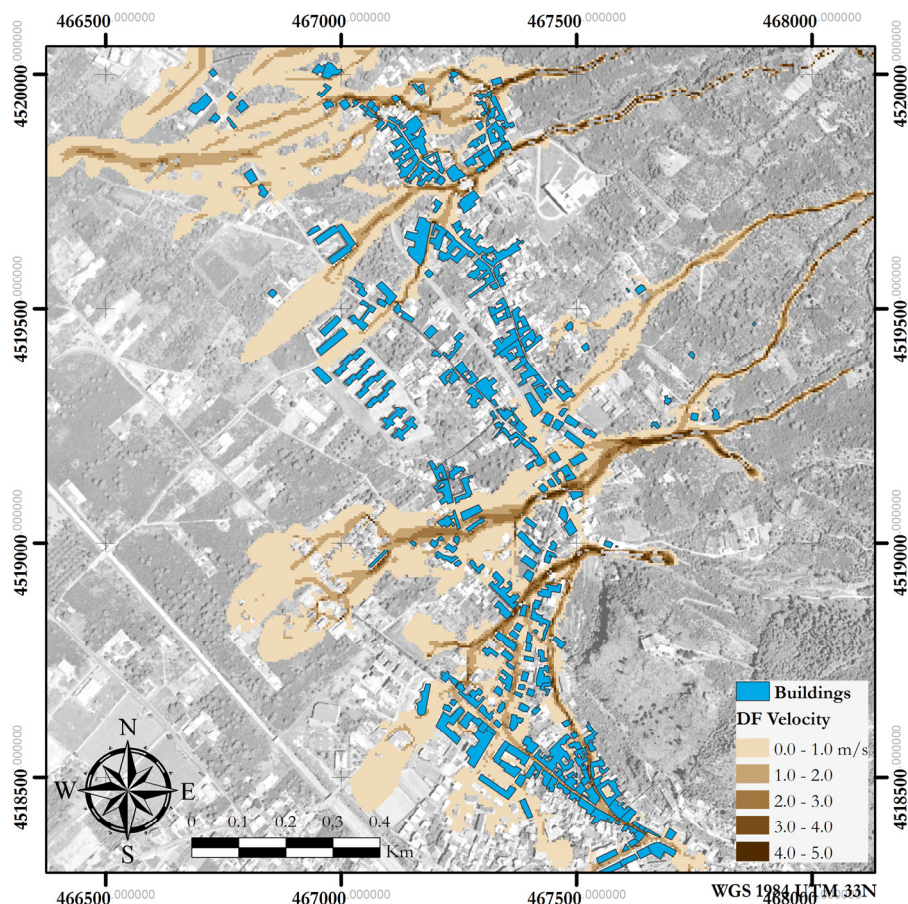


Fig. 5-12: The simulated Debris flow scenario in term of flow height (courtesy of G. Speranza, L. Martino and F. De Paola)



*Fig. 5-13: Debris flow scenarios map in term of flow velocity (courtesy of G. Speranza, L. Martino and F. De Paola)*

To reproduce the actions produced by the debris flow, the methodology described in Chapter 2 has been adopted using the software FLO2D in order to solve the bi-dimensional flow propagation. The details for the characterization of the hydrographic basin, flow characterization and two dimensional propagation are reported elsewhere ([Martino 2015](#)).

In Fig. 5-12 and Fig. 5-13, the debris flow event occurred in 1998 is simulated analytically in terms of debris flow height and velocity, respectively. The numerical propagation has been performed considering a digital elevation model (DEM) antecedent to the event and the buildings (considered as obstacles in the flow propagation) are those existing before the event.

A visual comparison between the analytically simulated debris flow scenario the actual footprint of the event (produced by aerial photos taken after the event, courtesy of prof. Antonio Santo) can be made by comparing Fig. 5-12 with Fig. 1-9. As it can be seen, the numerical propagation captures very well the occurred scenario which, however, in some areas appears to be more diffused. This aspect is due to the fact that the footprint of the



event has been reproduced from aerial photos taken some days after the event.

### 5.2.2 Structural portfolio characterization

In order to characterize the portfolio of structures build in Sarno municipality, an expeditious survey has been made on 40 buildings (Martino 2015). The survey sheet adopted for the field operation is a preliminary version of the one proposed in the research project METROPOLIS described in section 5.3.2. Given the many years passed from the event of 1998, the following criteria has been chosen for the selection of buildings to investigate:

- surveyed buildings should be constructed before 1998. Clearly the preference goes to those that were damaged in the event of 1998;
- surveyed buildings should be located along public roads to allow the survey operations without the need to access the private properties.

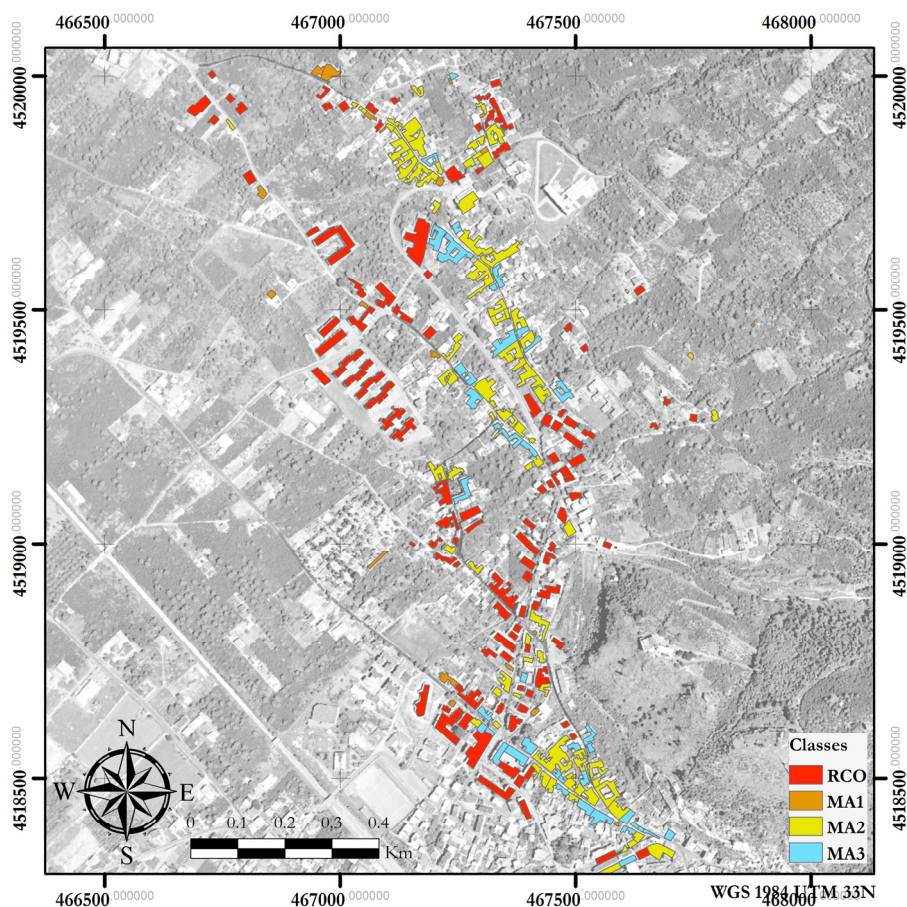


Fig. 5-14: The portfolio of buildings located in the Episcopio district, Sarno

As reported in Fig. 5-14, four structural classes have been identified (a class for the reinforced concrete buildings named RCO and three classes for the masonry buildings

named MA1, MA2, MA3 where the number represents the number of storeys); where 5 surveys per structural class have been performed.

The information collected in the survey sheets has been grouped based on the class of reference. A statistics analysis has been performed for each investigated parameter in order to characterize corresponding probability distributions. The probability distributions characterizing the geometrical uncertainties (defined previously in the Section 3.2.2, assuming independence between the parameters) are reported in Tab. 5-1 for the different classes.

$\Theta_{\text{geo}}$	MA1	MA2	MA3	RCO
$L$	LN [7.20; 0.38]	LN [9.23; 0.43]	LN [10.84; 0.31]	LN [4.00; 6.00]
$H_l$	U [3.30; 4.30]	U [3.00; 4.50]	U [3.10; 5.00]	U [2.90; 3.20]
$H_{i,th}$	-	U [3.00; 3.5]	U [3.00; 3.50]	-
$T$	U [0.40; 0.60]	U [0.40; 0.80]	U [0.50; 0.80]	U [0.25; 0.30]
$i$	U [4.00; 5.00]	U [4.00; 5.00]	U [4.00; 5.00]	-
$d_w$	U [1.20; 2.40]	U [1.20; 2.60]	U [0.70; 2.40]	U [1.00; 1.60]
$d_b$	U [1.90; 2.20]	U [1.90; 2.60]	U [2.00; 2.60]	U [1.90; 2.30]
$w_w$	U [0.90; 1.20]	U [1.00; 1.20]	U [0.50; 1.00]	U [0.90; 1.35]
$w_{jfb}$	U [1.00; 1.20]	U [0.85; 1.60]	U [0.80; 1.60]	U [0.80; 1.10]
$o_R$	F 0.30	F 0.26	F 0.32	F 0.23
$d_R$	F 0.60	F 0.38	F 0.41	F 0.50

Tab. 5-1: Geometrical uncertainties. Distributions: uniform U [min; max]; log-normal LN [median; logarithmic standard deviation]; fixed F [fixed value].

It is worth mentioning that the fast visual survey does not provide material mechanical properties (which can be obtained through tests). Hence, a literature study has been performed to characterize the uncertainties in material mechanical properties. The structural materials, recognized through the survey, are intersected with MADA database (Augenti et al. 2012) and several literature studies on masonry structures (Arya and Hegemier 1978; Augenti 2004; Calvi and Magenes 1991; Capozucca 2004; Chuxian 1984; Kaushik et al. 2007; Sawko 1982) and on infill walls of reinforced concrete buildings (Furtado et al. 2015; Griffith et al. 2007; Guidi et al. 2013; Pereira et al. 2011). In Tab. 5-2, the characterized material uncertainties have been listed.

$\Theta_{\text{mat}}$	MA1	MA2	MA3	RCO
$E$	U [690; 1220]	U [690; 1220]	U [690; 1220]	LN [5000; 0.39]
$\gamma_m$	U [16.0; 19.0]	U [16.0; 19.0]	U [16.0; 19.0]	U [7.0; 8.0]

$f_c$	$U$ [0.50; 2.00]	$U$ [0.50; 2.00]	$U$ [0.50; 2.00]	$LN$ [2.05; 0.68]
$f_t$	$U$ [0.10; 0.50]	$U$ [0.10; 0.50]	$U$ [0.10; 0.50]	$LN$ [0.16; 0.33]
$\tau_0$	$U$ [0.15; 0.50]	$U$ [0.15; 0.50]	$U$ [0.15; 0.50]	$LN$ [0.24; 0.33]

Tab. 5-2: Materials uncertainties. Distributions: uniform  $U$  [min; max]; log-normal  $LN$  [median; logarithmic standard deviation]; fixed  $F$  [fixed value].

Regarding the characterization of uncertainties for loading parameters: the possibility to that the floor slab is made up of wooden or reinforced concrete slabs is randomized; the specific weight of the flow and the impact azimuth distributions are characterized based on the analytical hydraulic propagation results; the drag coefficient  $D_c$  is assumed to belong to the interval [1.0;1.2] according to [FEMA \(2000\)](#); the friction coefficient  $\varphi$  (in the absence of more precise information) has been assumed to be log-normally distributed with median equal to 0.5 and a logarithmic standard error equal to 25%. In Tab. 5-3, the probability distributions used to describe the uncertainties in loading parameters have been listed.

$\Theta_{loa}$	MA1	MA2	MA3	RCO
$Q_{floor}$	-	$LN$ [8.09; 0.27]	$LN$ [8.09; 0.27]	$F$ 0.00
$Q_{ref}$	$LN$ [6.83; 0.07]	$LN$ [6.83; 0.27]	$LN$ [6.83; 0.27]	$F$ 0.00
$\gamma_{debr,flow}$	$LN$ [15.78; 0.2]	$LN$ [15.78; 0.2]	$LN$ [15.78; 0.2]	$LN$ [15.78; 0.2]
$D_c$	$U$ [1.0; 1.2]	$U$ [1.0; 1.2]	$U$ [1.0; 1.2]	$U$ [1.0; 1.2]
$\Omega$	$U$ [- $\pi/2$ ; $\pi/2$ ]	$U$ [- $\pi/2$ ; $\pi/2$ ]	$U$ [- $\pi/2$ ; $\pi/2$ ]	$U$ [- $\pi/2$ ; $\pi/2$ ]
$\varphi$	$LN$ [0.50; 0.25]	$LN$ [0.50; 0.25]	$LN$ [0.50; 0.25]	$LN$ [0.50; 0.25]

Tab. 5-3: The uncertainties in loading parameters. Distributions: uniform  $U$  [min; max]; log-normal  $LN$  [median; logarithmic standard deviation]; fixed  $F$  [fixed value].

A discrete probability distribution has been considered in order to model the uncertainty in the floor systems. It has been assumed a probability of 0.5 to have a reinforced concrete floor and a probability of 0.5 to have a wooden floor system.

### 5.2.3 Vulnerability and risk assessment

The structural fragility assessment for each class has been performed by creating 50 simulations of single wall models generated automatically based on the survey results by software HydRA. The intensity measure chosen for the analyses is the flow height  $H$  conditioned on six values of the flow velocity (0, 2, 5, 10, 15 and 20 m/s). The FEM model is based on a size mesh variable between 200x200mm up to 250x250mm. The constraint condition considered for the walls are: the base is considered as clamped; the lateral constraint with a probability of 0.5 and a limit form ratio (for clamped or hinged side) equal to 8; rigid diaphragm in correspondence of the floors with probability of 0.5. HydRA's option for removing the failed elements during the incremental analysis has been activated.

Two limit states have been considered: the damage limit state (*DLS*) and the collapse prevention limit state (*CLS*) defined in section 3.3.5. As it regards the ultimate limit states function  $DCR_{CLS}$  reported in Eq. 3-50, it is necessary to define threshold  $p_{CLS}$  of the proportion of failed elements which induce the *CLS*. It has been assumed as a conventional criterion that the collapse prevention limit state is reached when the 50% of the elements fail so that the threshold  $p_{CLS}$  is assumed equal to 0.5.

The results of the vulnerability assessment are reported in terms of fragility curves for each limit state and for each considered flow velocity, grouped based on the defined class (Fig. 5-15 up to Fig. 5-18). In the legend of the pictures, also the median and the logarithmic standard deviation of each curve is reported.

It can be observed that the fragility curves are lined (more-or-less) from right to left based on the increasing values of the velocity on which the fragility curves are conditioned. This is to be expected as the structural demand (in terms of stress) increases with respect to the increasing of the velocity.

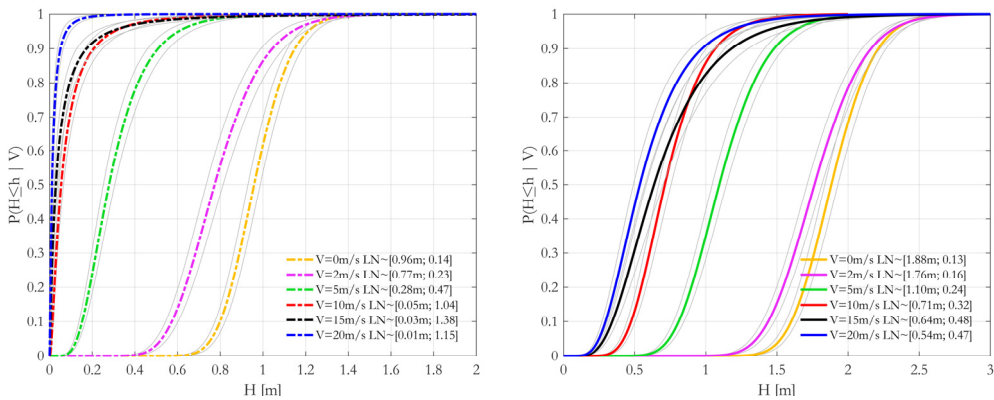


Fig. 5-15: Fragility curves for class “RCO” at DLS (dashed lines) and CLS (solid lines).

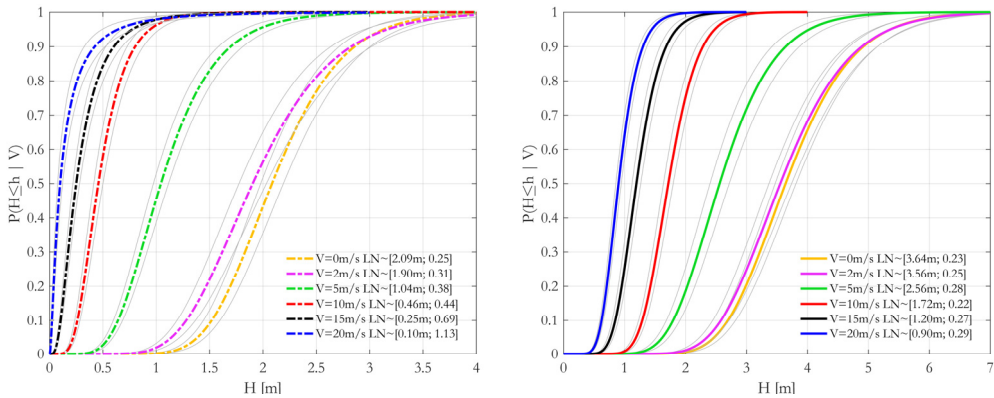


Fig. 5-16: Fragility curves for class “MA1” at DLS (dashed lines) and CLS (solid lines).

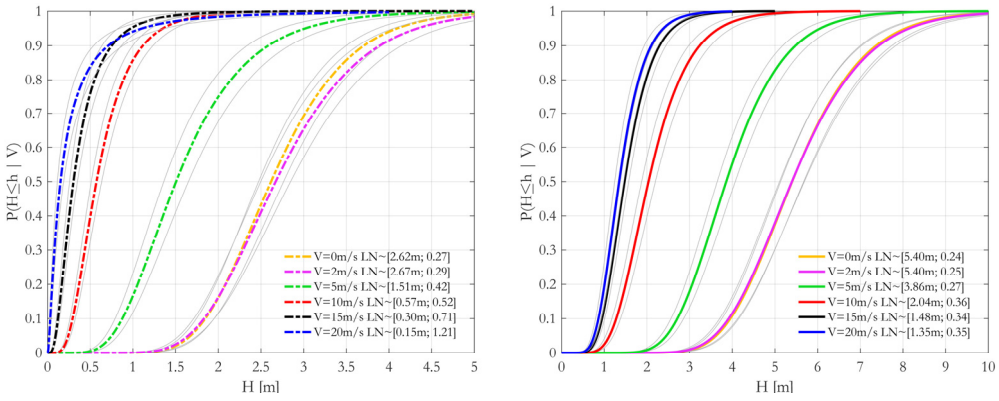


Fig. 5-17: Fragility curves for class “MA2” at DLS (dashed lines) and CLS (solid lines).

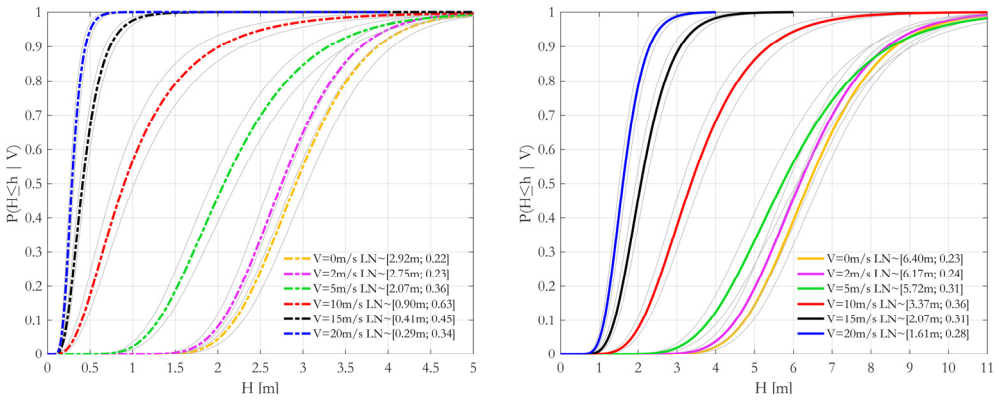


Fig. 5-18: Fragility curves for class “MA3” at DLS (dashed lines) and CLS (solid lines).

The vulnerability of the masonry structures decrease (fragility curves shifted to the right) as the number of storeys increase. This aspect is due to the fact the axial loads, which generally increase the resistance for overturning (Eq. 3-43, up to a certain value of axial load) and the shear mechanisms (Eqs. 3-46 and 3-48), increases with the number of storeys.

The reinforced concrete seems to be the most vulnerable class among those considered. This is to be expected since the infill walls are not bearing vertical loads apart from their own weight (the main reason behind their lowest resistance). Moreover, the collapse of the infill walls (which are not considered as primary structural elements) is not expected to lead to the global structural collapse (as opposed to the case of masonry buildings).

To compare the observed damages with the analytically simulated ones, the map of probability of exceeding the damage limit state has been represented in Fig. 5-19. The integration has been carried on in terms of flow height considering a fragility curve (for each building) representative of the structural class and the corresponding velocity. When the flow velocity on a building is not one of the considered values in the vulnerability estimation,

a fragility curve obtained by interpolation is employed (see Eq. 5-3 reported in the next section).

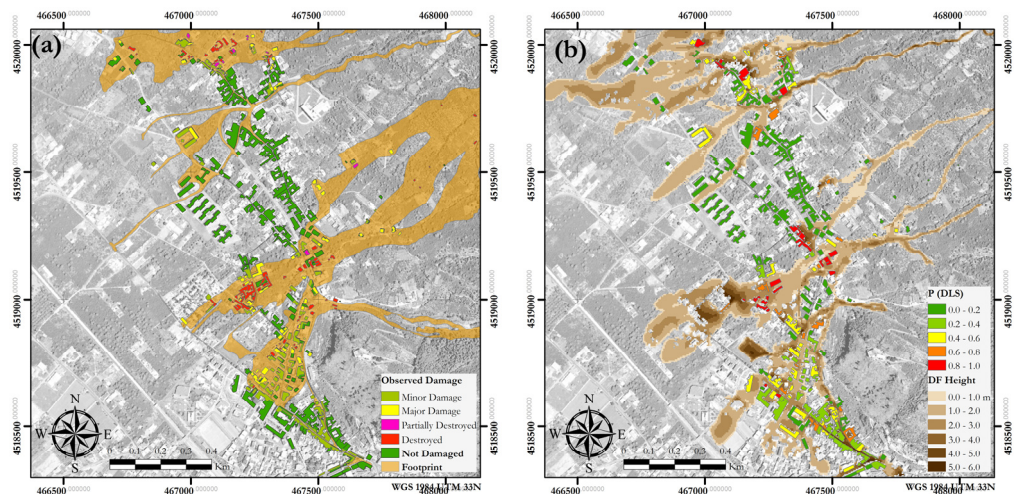


*Fig. 5-19: (a) observed damage after the event of 1998; (b) probability of exceeding the DLS in one year (analytic simulation of the event).*

A side-by-side comparison of the annual probability of exceeding DLS (Fig. 5-19b) and the observed damages (Fig. 5-19a) reveal satisfactory agreement --albeit notable differences at the single building level. The small observed difference at the building level is due to several factors. The first regards the assumptions made in the geological model and in the hydraulic propagation; the second regards the fact that the vulnerability assessment has been performed at the structural class level and not at the building level.

### 5.3 Castellammare di Stabia: risk analysis

Castellammare di Stabia is the city object of demonstration of all the hydrogeological studies made during METROPOLIS, that is the research project in which this thesis has been developed. Many research groups studied all the hydrogeological issues for Castellammare di Stabia, based on their own competences.

All the results are under publication on a WebGIS platform at the address: <http://151.1.25.219/metropolis/testwebsite2/defaultmapv2.html>, and all the aspects regarding the vulnerability and risk calculation are described in the following subsections.

#### 5.3.1 Characterizing debris flow and flooding actions

In order to assess the debris flow and flooding hazard in the case study area, six catchments have been considered according to the morphology of the area (five for debris

<sup>1</sup> This is a temporary link checked the last time on 28<sup>th</sup> of February 2017. If the definitive link will be available before the final submission of this thesis, it will be updated.

flow and one for flooding. A group of experts (Antonio Santo, Giovanni Forte, Melania De Falco, Francesco De Paola, Giuseppe Speranza) has performed the geological, hydrological and hydraulic analysis within the research project METROPOLIS (see Metropolis deliverable 2.1 for details).

As far as it regards the debris flow, three scenarios are considered based on the plausible minimum, medium and maximum mobilized volumes. The considered specific weight of the solid sediments is estimated equal to  $26.5 \text{ kN}/\text{m}^3$  and the volumetric concentration of the sediments is assumed to be equal to  $0.35$ . Thus, the specific weight of the debris flow is estimated to be  $15.75 \text{ kN}/\text{m}^3$  as reported in Eq. 5-2.

$$\gamma_f = \gamma_{water} + C_v \cdot (\gamma_{solid} - \gamma_{water}) = 10.0 + 0.35 \cdot (26.5 - 10.0) = 15.78 \text{ kN}/\text{m}^3 \quad 5-2$$

The results of the hydraulic propagation of the debris flow reported in terms of flow height and velocity are shown in Fig. 5-20, for the three above-mentioned scenarios.

As far as it regards the flooding, only one catchment has been considered. The corresponding hydrograph has been propagated considering five return periods of the rainfall events (10, 30, 50, 100 and 300 years). The results are reported in Fig. 5-21 in terms of flow height and flow velocity only for 10, 50 and 300 years of return periods.

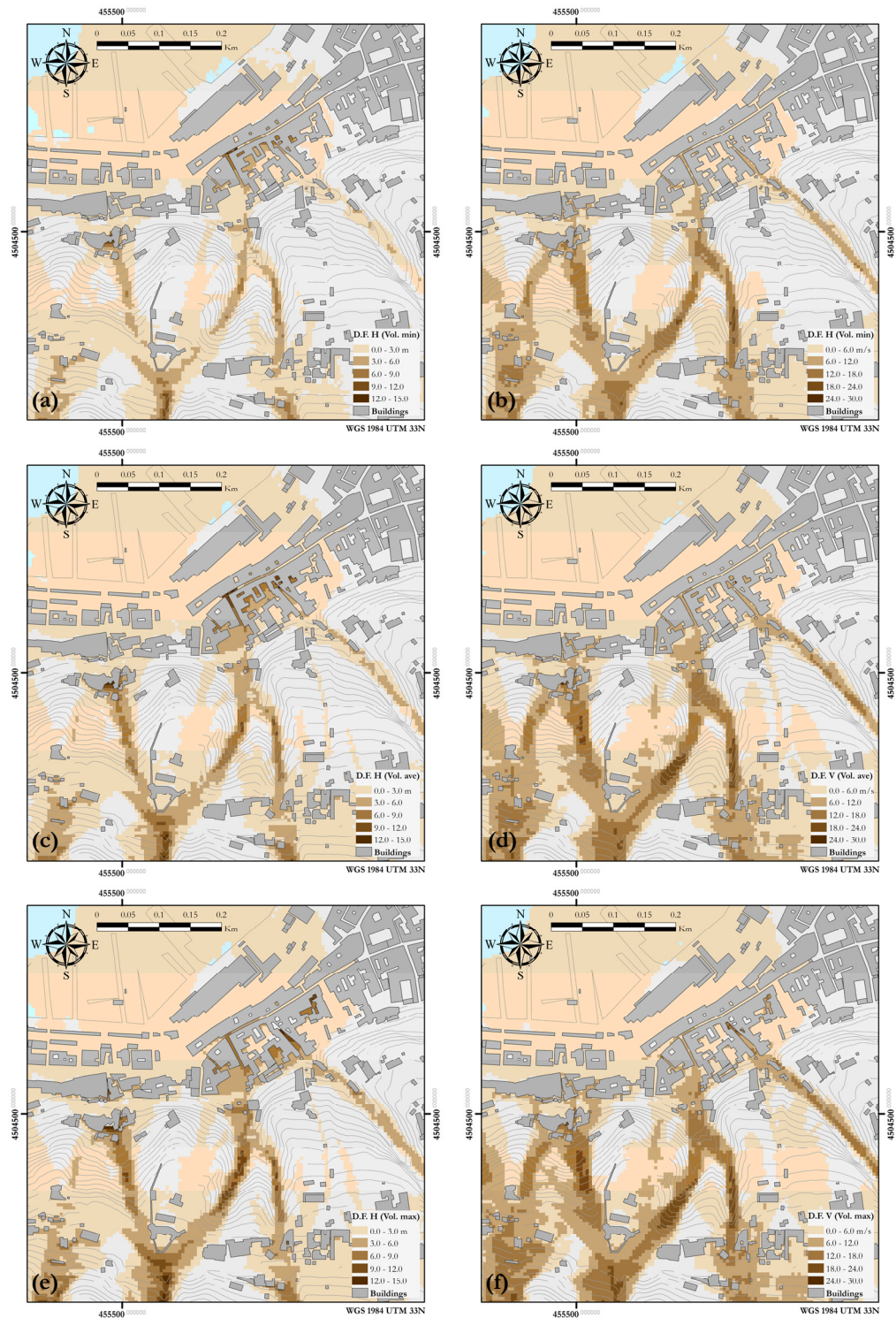


*Fig. 5-20: Maps of three debris flow scenarios. (a), (c) and (e) represent the flow height for the minimum, the average and the maximum volume scenarios, respectively. (b), (d) and (f) represent the flow velocity for the minimum, the average and the maximum volume scenarios, respectively.*



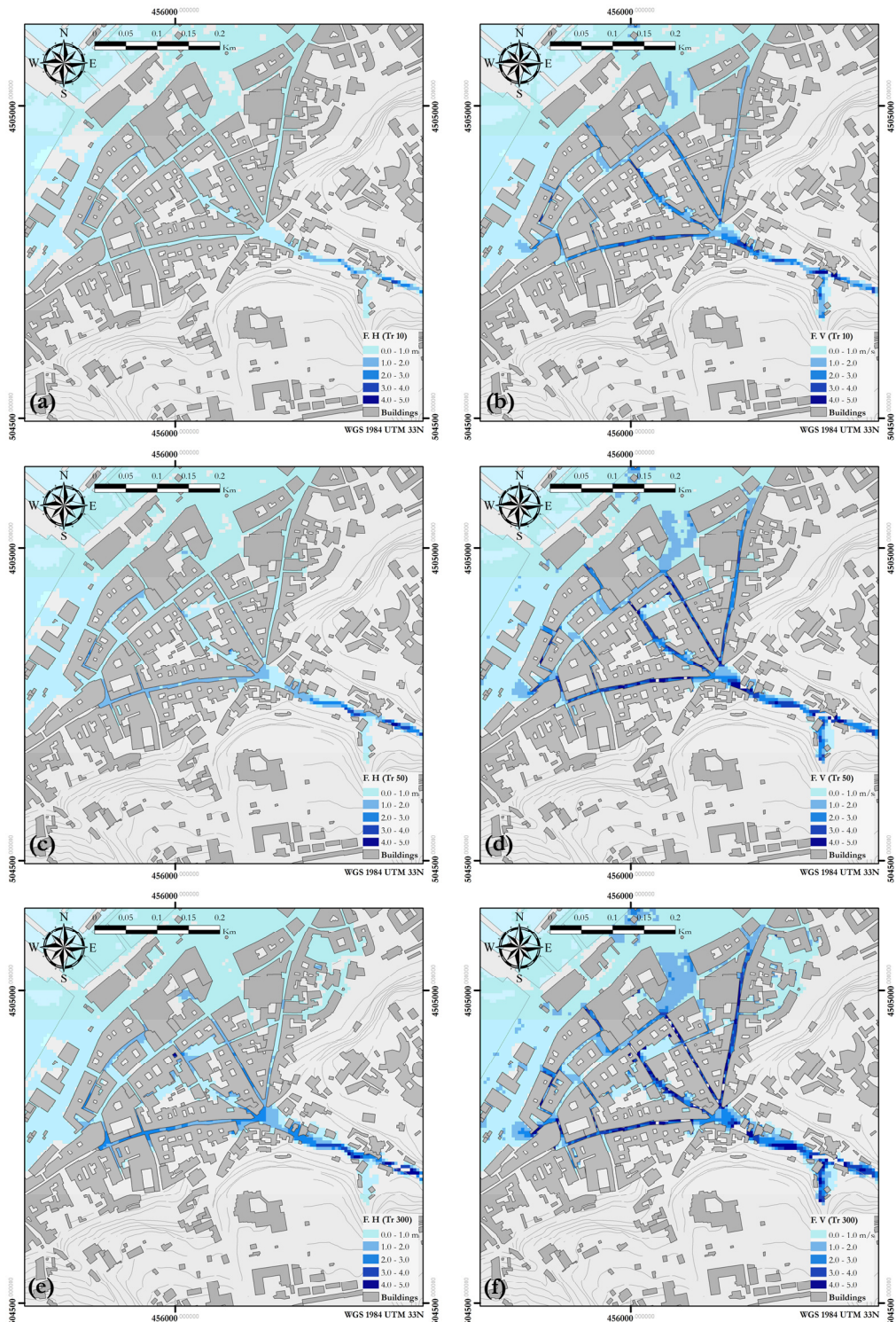


Fig. 5-21: Flooding hazard maps. (a), (c) and (e) represent the flooding height for return periods 10, 50 and 300 years, respectively. (b), (d) and (f) represent the flooding velocity for return periods 10, 50, and 300 years, respectively.

### 5.3.2 Structural portfolio characterization

In order to characterize the portfolio of structures in Castellammare municipality, a fast visual survey has been done on about 190 buildings by the ICIE Inc. in July 2016 as a part of activities for METROPOLIS research project. An integrated survey sheet has been developed during the project by all the involved research groups with the aim of reaching a sufficient knowledge level about the urban texture in Castellammare.

The following criteria have kept in mind for the selection of surveyed buildings:

- the surveyed buildings should be located in the foot print of the areas delineated as prone to debris flow and flooding;
- the surveyed buildings should be located along public roads in order to allow the survey operations without the need to access in the private properties.

The two building portfolios corresponding to two areas identified as prone to debris flow and flooding considered herein are shown in Fig. 5-22.

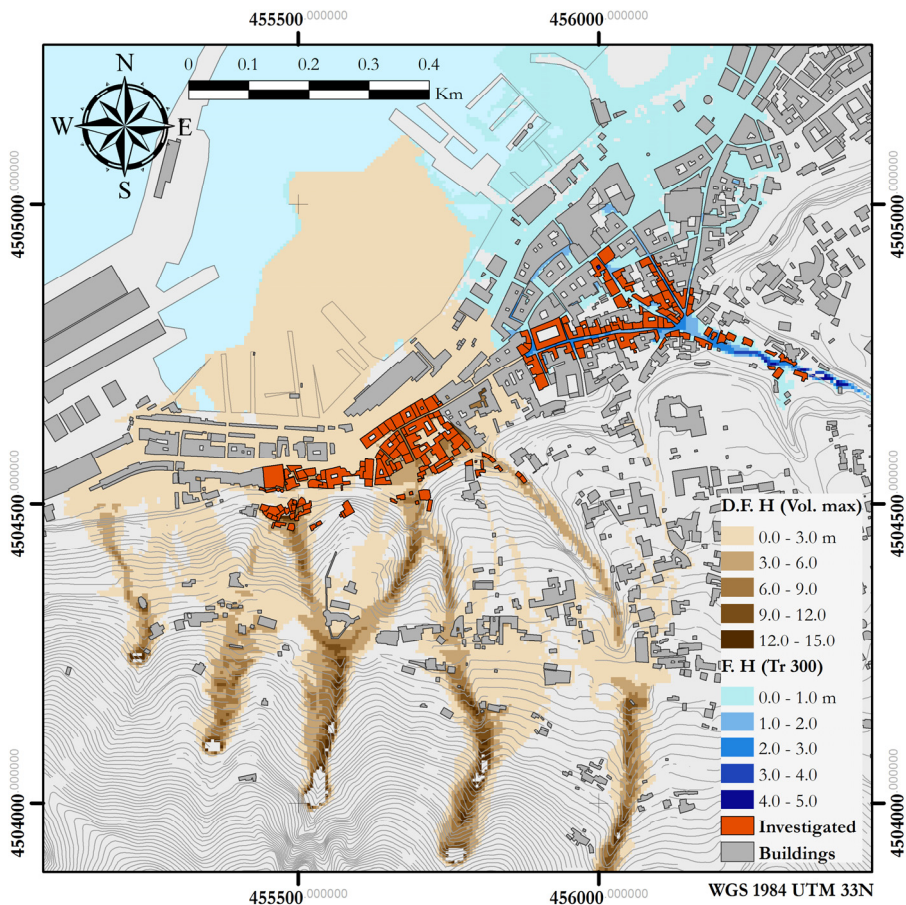


Fig. 5-22: the two building portfolios considered

The survey results have been studied in order to define the building classes. The pie charts illustrated in Fig. 5-23, report the breakdown of the surveyed buildings in terms of the structural type, the use and the number of storeys (only for the masonry buildings).

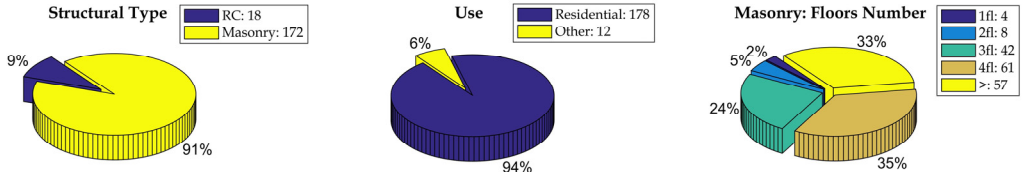


Fig. 5-23: Break-down of the main features of the surveyed buildings.

Six structural classes have been defined in order to classify the considered portfolio of buildings in terms of hydrogeological vulnerability: a class for the reinforced concrete buildings labelled *RCO* and five classes for the masonry buildings labelled *MA1*, *MA2*, *MA3*, *MA4*, *MAP*, where the number represents the number of storeys and *P* indicates the class of buildings with more than 4 floors. The map in Fig. 5-24 illustrates the composition of the portfolio of buildings in term of their class.

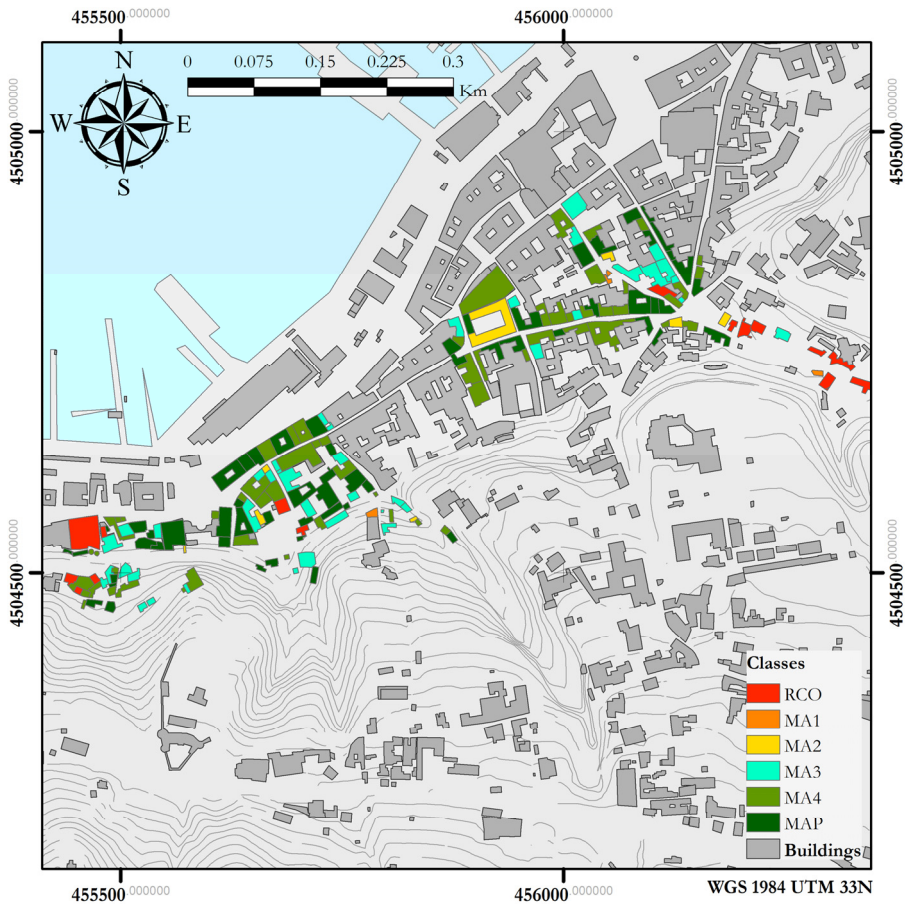


Fig. 5-24: Map of the structural classes.

All the information collected in the survey sheets has been grouped based on the assigned class. A statistics analysis has been performed for each investigated parameter in order to characterize the probability distributions. The probability distributions fitted for the geometrical uncertainties (defined previously in the Section 3.2.2, assuming independence between the parameters) are reported in Tab. 5-4 for the different classes.

$\Theta_{\text{geo}}$	MA1	MA2	MA3	MA4	MAP	RCO
$L$	$LN$ [8.40; 0.45]	$LN$ [10.04; 0.39]	$LN$ [11.18; 0.36]	$LN$ [9.68; 0.42]	$LN$ [10.25; 0.34]	$LN$ [4.00; 6.00]
$H_I$	$U$ [3.60; 5.10]	$U$ [3.85; 5.20]	$U$ [3.30; 4.90]	$U$ [3.50; 4.90]	$U$ [3.90; 5.10]	$U$ [2.90; 3.20]
$H_{i-th}$	-	$U$ [3.45; 5.85]	$U$ [2.90; 3.30]	$U$ [2.90; 3.50]	$U$ [2.90; 3.90]	-
$T$	$U$ [0.40; 0.60]	$U$ [0.40; 0.60]	$U$ [0.60; 0.80]	$U$ [0.80; 1.20]	$U$ [0.80; 1.20]	$U$ [0.25; 0.30]
$i$	$U$ [4.00; 5.00]	$U$ [4.00; 5.00]	$U$ [4.00; 5.00]	$U$ [4.00; 5.00]	$U$ [4.00; 5.00]	-
$d_n$	$U$ [1.20; 1.40]	$U$ [1.20; 1.60]	$U$ [1.00; 1.40]	$U$ [1.00; 1.40]	$U$ [1.00; 1.40]	$U$ [1.20; 1.80]
$d_b$	$U$ [2.00; 2.40]	$U$ [2.00; 2.40]	$U$ [2.00; 2.40]	$U$ [2.00; 2.40]	$U$ [2.00; 2.40]	$U$ [2.00; 2.40]
$w_n$	$U$ [0.90; 1.40]	$U$ [1.00; 1.20]	$U$ [0.90; 1.40]	$U$ [0.90; 1.40]	$U$ [0.90; 1.40]	$U$ [1.00; 1.35]
$w_{j\beta}$	$U$ [0.80; 1.10]	$U$ [0.80; 1.10]	$U$ [0.80; 1.10]	$U$ [0.80; 1.10]	$U$ [0.80; 1.10]	$U$ [0.80; 1.10]
$\theta_R$	$F$ 0.34	$F$ 0.31	$F$ 0.29	$F$ 0.28	$F$ 0.25	$F$ 0.25
$d_R$	$F$ 0.56	$F$ 0.42	$F$ 0.38	$F$ 0.38	$F$ 0.40	$F$ 0.50

Tab. 5-4: The uncertainties in the geometrical parameters. Distributions: uniform  $U$  [min; max]; log-normal  $LN$  [median; logarithmic standard deviation]; fixed  $F$  [fixed value].

This fast visual survey does not provide any characterization of the material mechanical properties (apart from a visual recognition of the material used predominantly for the construction of the building). In order to characterize the material uncertainties, a literature study has been performed. The MADA database ([Augenti et al. 2012](#)) and several literature works for masonry structures ([Arya and Hegemier 1978](#); [Augenti 2004](#); [Calvi and Magenes 1991](#); [Capozucca 2004](#); [Chuxian 1984](#); [Kaushik et al. 2007](#); [Sawko 1982](#)) and infill walls of reinforced concrete buildings ([Furtado et al. 2015](#); [Griffith et al. 2007](#); [Guidi et al. 2013](#); [Pereira et al. 2011](#)) have been consulted. In Tab. 5-5, the characterized material uncertainties have been reported.

$\Theta_{\text{mat}}$	MA1	MA2	MA3	MA4	MAP	RCO
$E$	$U$ [690; 1220]	$U$ [690; 1220]	$U$ [690; 1220]	$U$ [690; 1220]	$U$ [690; 1220]	$LN$ [5000; 0.39]
$\gamma_m$	$U$ [16.0; 19.0]	$U$ [16.0; 19.0]	$U$ [16.0; 19.0]	$U$ [16.0; 19.0]	$U$ [16.0; 19.0]	$U$ [7.0; 8.0]
$f_c$	$U$ [0.50; 2.00]	$U$ [0.50; 2.00]	$U$ [0.50; 2.00]	$U$ [0.50; 2.00]	$U$ [0.50; 2.00]	$LN$ [2.05; 0.68]
$f_t$	$U$ [0.10; 0.50]	$U$ [0.10; 0.50]	$U$ [0.10; 0.50]	$U$ [0.10; 0.50]	$U$ [0.10; 0.50]	$LN$ [0.16; 0.33]
$\tau_0$	$U$ [0.15; 0.50]	$U$ [0.15; 0.50]	$U$ [0.15; 0.50]	$U$ [0.15; 0.50]	$U$ [0.15; 0.50]	$LN$ [0.24; 0.33]

Tab. 5-5: The uncertainties in material mechanical properties. Distributions: uniform  $U$  [min; max]; log-normal LN [median; logarithmic standard deviation]; fixed  $F$  [fixed value].

Regarding the characterization of uncertainties for loading parameters: the possibility to that the floor slab is made up of wooden or reinforced concrete slabs is randomized; the specific weight of the flow and the impact azimuth distributions are characterized based on the analytical hydraulic propagation results; the drag coefficient  $D_c$  is assumed to belong to the interval [1.0;1.2] according to FEMA (2000); the friction coefficient  $\varphi$  (in the absence of more precise information) has been assumed to be log-normally distributed with median equal to 0.5 and a logarithmic standard error equal to 25%. In Tab. 5-3, the probability distributions used to describe the uncertainties in loading parameters have been listed.

$\Theta_{loa}$	MA1	MA2	MA3	MA4	MAP	RCO
$Q_{floor}$	-	LN [8.09; 0.27]	LN [8.09; 0.27]	LN [8.29; 0.27]	LN [8.09; 0.07]	$F$ 0.00
$Q_{roof}$	LN [6.83; 0.07]	LN [6.83; 0.27]	LN [6.83; 0.27]	LN [6.23; 0.27]	LN [6.83; 0.07]	$F$ 0.00
$\gamma_{flood}$	LN [11.0; 0.2]	LN [11.0; 0.2]	LN [11.0; 0.2]	LN [11.0; 0.2]	LN [11.0; 0.2]	LN [11.0; 0.2]
$\gamma_{debr,flow}$	LN [15.78; 0.2]	LN [15.78; 0.2]	LN [15.78; 0.2]	LN [15.78; 0.2]	LN [15.78; 0.2]	LN [15.78; 0.2]
$D_c$	$U$ [1.0; 1.2]	$U$ [1.0; 1.2]	$U$ [1.0; 1.2]	$U$ [1.0; 1.2]	$U$ [1.0; 1.2]	$U$ [1.0; 1.2]
$\Omega$	$U$ [- $\pi/2$ ; $\pi/2$ ]	$U$ [- $\pi/2$ ; $\pi/2$ ]	$U$ [- $\pi/2$ ; $\pi/2$ ]	$U$ [- $\pi/2$ ; $\pi/2$ ]	$U$ [- $\pi/2$ ; $\pi/2$ ]	$U$ [- $\pi/2$ ; $\pi/2$ ]
$\varphi$	LN [0.50; 0.25]	LN [0.50; 0.25]	LN [0.50; 0.25]	LN [0.50; 0.25]	LN [0.50; 0.25]	LN [0.50; 0.25]

Tab. 5-6: The uncertainties in loading parameters. Distributions: uniform  $U$  [min; max]; log-normal LN [median; logarithmic standard deviation]; fixed  $F$  [fixed value].

A discrete probability distribution has been considered in order to model the uncertainty in the floor systems. It has been assumed a probability of 0.5 to have a reinforced concrete floor and a probability of 0.5 to have a wooden floor system.

### 5.3.3 Vulnerability and risk assessment

The structural fragility assessment for each class has been performed through creation of 50 simulations of single-wall models generated automatically by HydRA. The intensity measure chosen for the analyses is the flow height  $H$  conditioned on six values of the flow velocity (0, 2, 5, 10, 15 and 20 m/s). The FEM model is based on a size mesh variable between 200x200mm and 250x250mm. The constraint condition considered for the walls are: the base is considered as clamped; the lateral constraint with a probability of 0.5 and a limit form ratio (for clamped or hinged side) equal to 8; rigid diaphragm in correspondence of the floors with probability of 0.5. HydRA's option for removing the failed elements during the incremental analysis has been activated.

Two limit states have been considered: the damage limit state ( $DL_S$ ) and the collapse prevention limit state ( $CL_S$ ) defined in section 3.3.5. As it regards the ultimate limit state

function  $DCR_{CLS}$  reported in Eq. 3-50, it is necessary to define the threshold  $p_{CLS}$  of the proportion of failed element for the  $CLS$ . It has been assumed as a conventional criterion that the collapse prevention limit state is reached when the 50% of the elements fail. Thus, the threshold  $p_{CLS}$  is set equal to 0.5.

The fragility curves for each limit state and prescribed flow velocity are illustrated in Fig. 5-25 up to Fig. 5-30, grouped based on the structural class. It should be noted that, for each structural class, the robust fragility and the robust plus/minus one logarithmic standard deviation curves are reported.

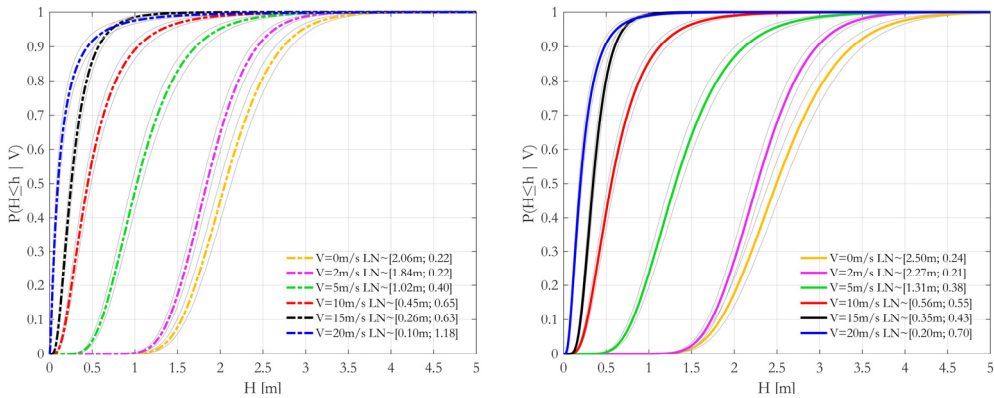


Fig. 5-25: Fragility curves for class "MA1" at DLS (dashed lines) and CLS (solid lines).

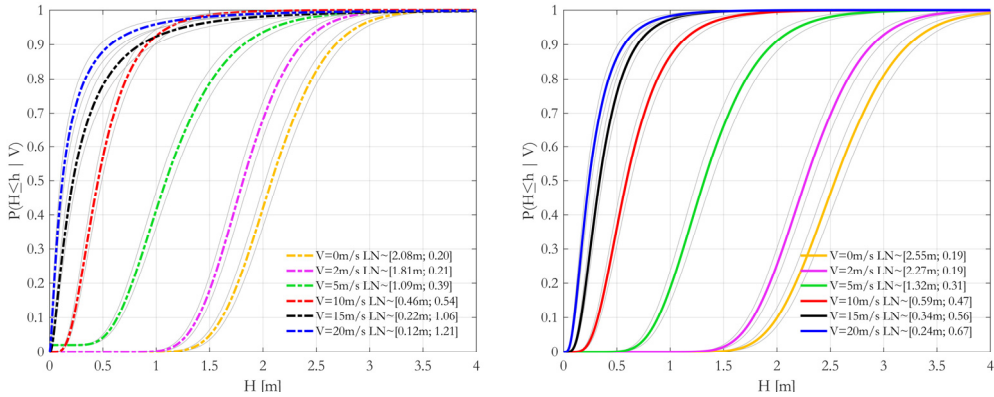


Fig. 5-26: Fragility curves for class "MA2" at DLS (dashed lines) and CLS (solid lines).

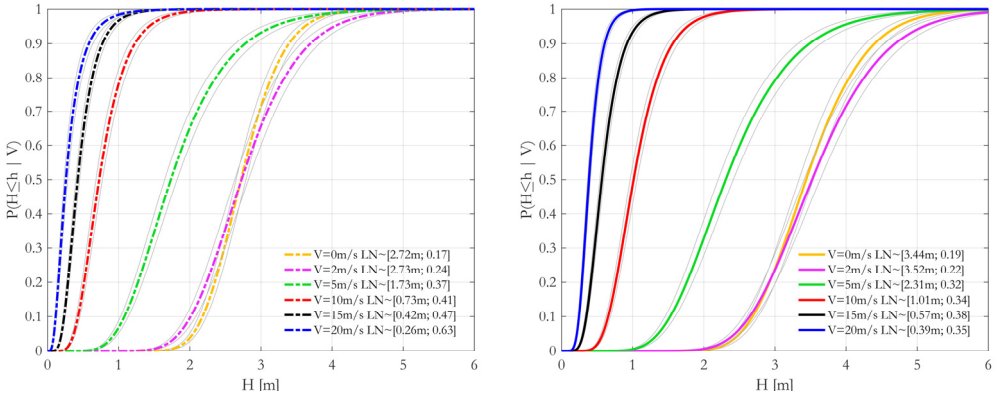


Fig. 5-27: Fragility curves for class “MA3” at DLS (dashed lines) and CLS (solid lines).

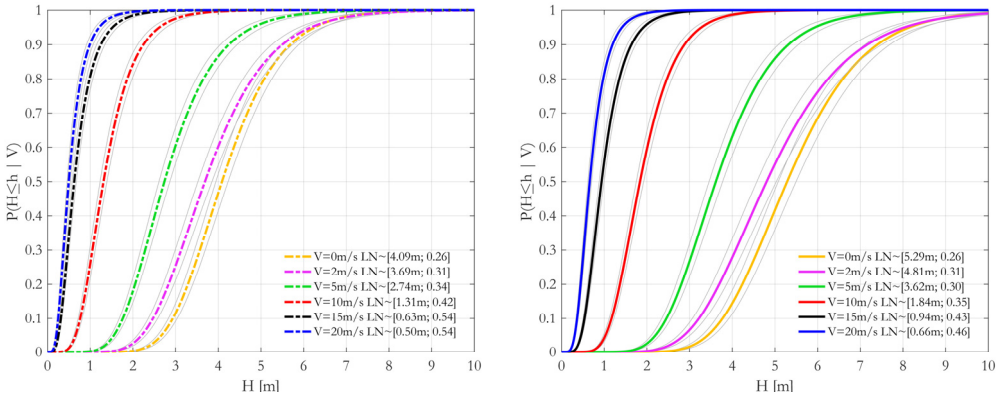


Fig. 5-28: Fragility curves for class “MA4” at DLS (dashed lines) and CLS (solid lines).

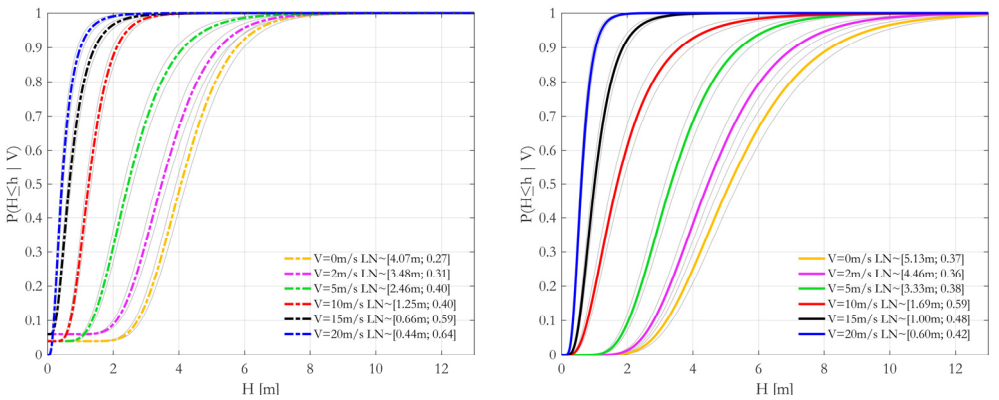


Fig. 5-29: Fragility curves for class “MAP” at DLS (dashed lines) and CLS (solid lines).

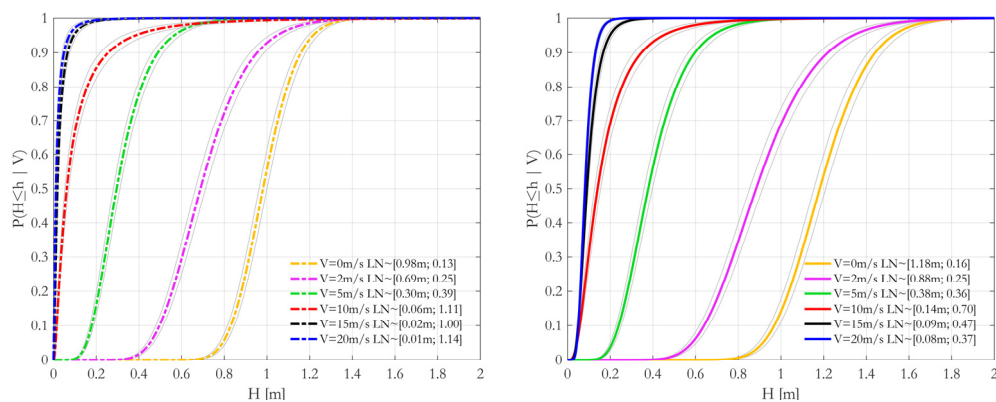


Fig. 5-30: Fragility curves for class “RCO” at DLS (dashed lines) and CLS (solid lines).

The following observations can be made by observing the fragility curves reported in Fig. 5-25 to Fig. 5-30:

- The fragility curves shift from right to left (more-or-less) based on the increasing value of the prescribed flow velocity values. This is to be expected since the structural demand increases as a result of increasing prescribed velocity values.
- The fragility curves for the DLS and the CLS get closer as the structures becomes more vulnerable (the fragilities shifting to the left). This is since the fragility curves (for the same structural class) with lower median values are representative of higher flow velocity values. In the incremental analysis with respect to flow height, for higher flow velocity values, the structural demand increases rapidly between two successive analysis steps. In such a situation, the structure can exceed the two consecutive limit states (DLS and CLS) with a small increase of the flow height and therefore the observed proximity of the two corresponding fragility curves. In other words, for small velocity values, a larger step in terms of flow height is necessary to produce the collapse of a wall (characterized herein by failure in 50% of the elements).
- The vulnerability of the masonry structures decreases (fragility curves shifted to the right) with respect to the increasing number of storeys. This is due to the fact that the axial load increases with the number of storeys. This generally leads to higher overturning (Eq. 3-43) and sliding shear (Eqs. 3-46 and 3-48) resistance.
- The most vulnerable class appears to be the reinforced concrete. It should be kept in mind that the infill walls bear only self-weight and are not considered as primary structural elements.

The hydrogeological risk assessment has been performed by numerical integration in terms of probability of exceeding the considered limit states for three debris flow scenarios according to Eq. 3-9 (Fig. 5-33) and in terms of probability of exceeding the considered limit states in 10, 50 and 300 years according to Eqs. 3-6 and 1-3 (Fig. 5-34). In both cases,



the integration has been calculated in terms of flow height considering the fragility curve (for each building) representative of the structural class and the corresponding velocity. When the flow velocity evaluated for a given building is not among one of the considered velocity values, an interpolated fragility curve is considered:

$$\Phi^{-1}[H \leq b | V = v_x] = \Phi^{-1}[H \leq b | V = v_{bigger}] + \alpha \cdot (v_{bigger} - v_x) \quad 5-3$$

where:  $\Phi^{-1}[H \leq b | V = v_x]$  is the log-normal inverse function of the desired fragility curve corresponding to velocity equal to  $v_x$ ;  $\Phi^{-1}[H \leq b | V = v_{bigger}]$  is the log-normal inverse function of the fragility curve corresponding to the velocity value  $v_{bigger}$  immediately higher than  $v_x$ ;  $\alpha$  is a coefficient calculated from Eq. 5-4 where  $v_{lower}$  is the velocity value immediately lower than  $v_x$ .

$$\alpha = \frac{\Phi^{-1}[H \leq b | V = v_{lower}] - \Phi^{-1}[H \leq b | V = v_{higher}]}{v_{lower} - v_{higher}} \cdot (v_{higher} - v_x) \quad 5-4$$

An example of interpolation of a fragility curve is reported in Fig. 5-31 for the limit state *CLS* and class *MA2*. The calculated fragility curves (by the analysis) are conditioned to flow velocity values equal to 5 and 10 m/s. Applying Eq. 5-31, it is possible to obtain the fragility curves for velocity values 7 and 9 m/s.

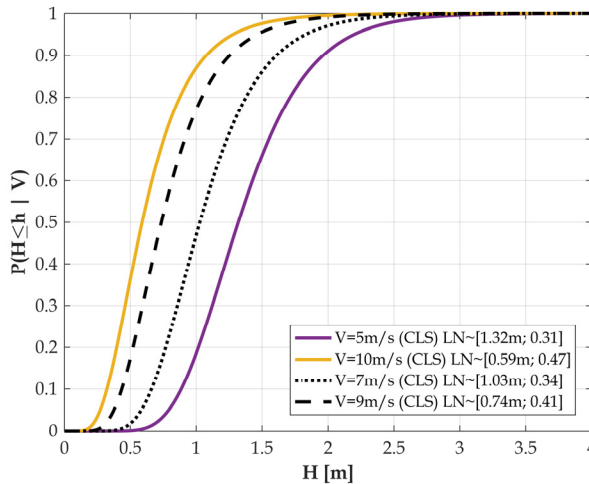


Fig. 5-31: Example of fragility curve interpolation for class “MA2”.

In Fig. 5-32(a), the results of the safety-checking based on DCFD format have been reported for the damage limit state for the portfolio of flood-prone buildings referring to an acceptable risk level characterized by 50 year return period (attention should be made that 50 years is not the return period of the rainfall event). This alternative representation

of the risk is particularly useful for decision-making purposes. In fact, by only looking at the map, it is possible to identify all the red buildings as those that have exceeded the DLS.

In Fig. 5-32(b), the return period capacities (for DLS) have been reported for the portfolio of flood-prone buildings. This representation is particularly useful for decision-making as far as it regards the suitable risk mitigation strategies to be adopted. Comparing Fig. 5-32(b) with Fig. 5-32(a), it is possible to appreciate the coherence between the two alternative risk representations. All the buildings with a return period capacity lower than or equal to 50 years are identified with a DCFD ratio greater than or equal to 1.

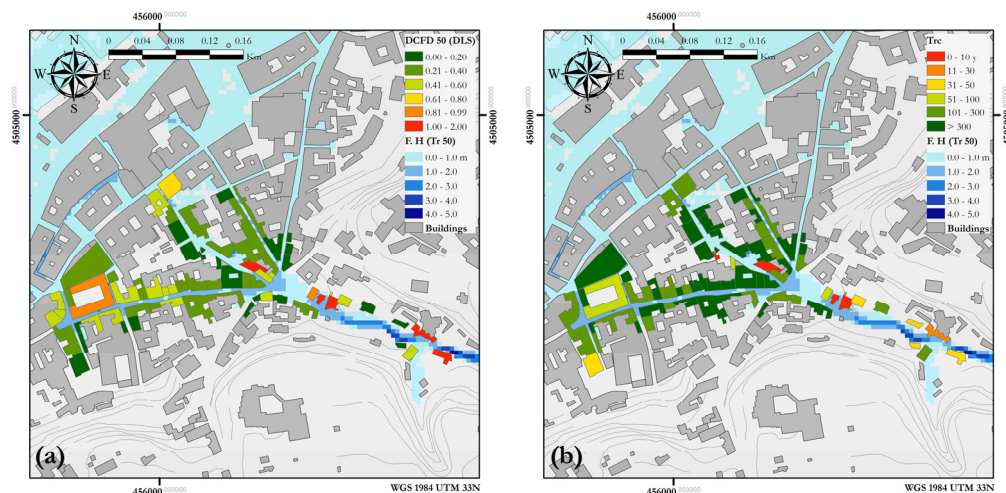
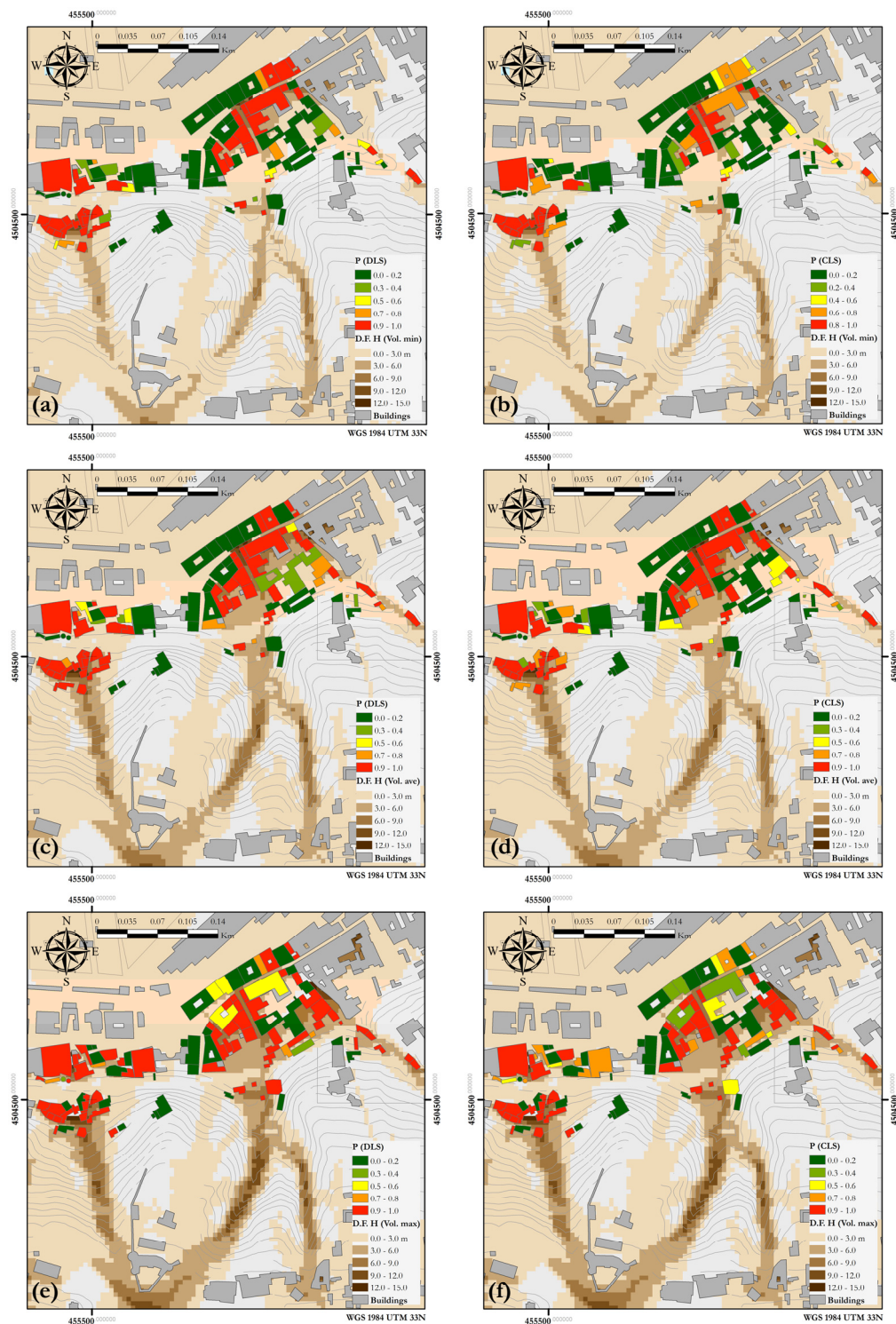


Fig. 5-32: (a) DCFD map for damage limit state (DLS) with acceptable risk corresponding to 50 years return period; (b) the map of return period capacities.

The results of the hydrogeological risk assessment are represented in the risk maps reported in the figures below. In Fig. 5-33, the probability of exceeding the damage and the collapse prevention limit states have been represented for debris flow for the three different considered volume-based scenarios; in Fig. 5-34, instead, the risk in terms of probability of exceeding the two limit states in 10, 50 and 300 years is reported for flooding.

As it is shown, the maximum-volume scenario for the debris flow and the maximum return period for the flooding do not necessarily correspond to the worst conditions. This can be justified by the fact that during its propagation the flow can find alternative ways based on the energy, the topography and the building influence.

Looking at the buildings, it can be observed that the knowledge of hydrogeological hazard alone is not sufficient for representing the risk. In fact, the buildings belonging to more vulnerable structural classes are risk-prone even if they are located in zones that are characterized as low-hazard. This consideration highlights the importance of a suitable definition of structural classes and also the importance of accurate structural vulnerability assessment.



*Fig. 5-33: (a), (c) and (e): probability of exceeding the DLS for the minimum, the average and the maximum volume scenarios, respectively. (b), (d) and (f): probability of exceeding the CLS for the minimum, the average and the maximum volume scenarios, respectively.*

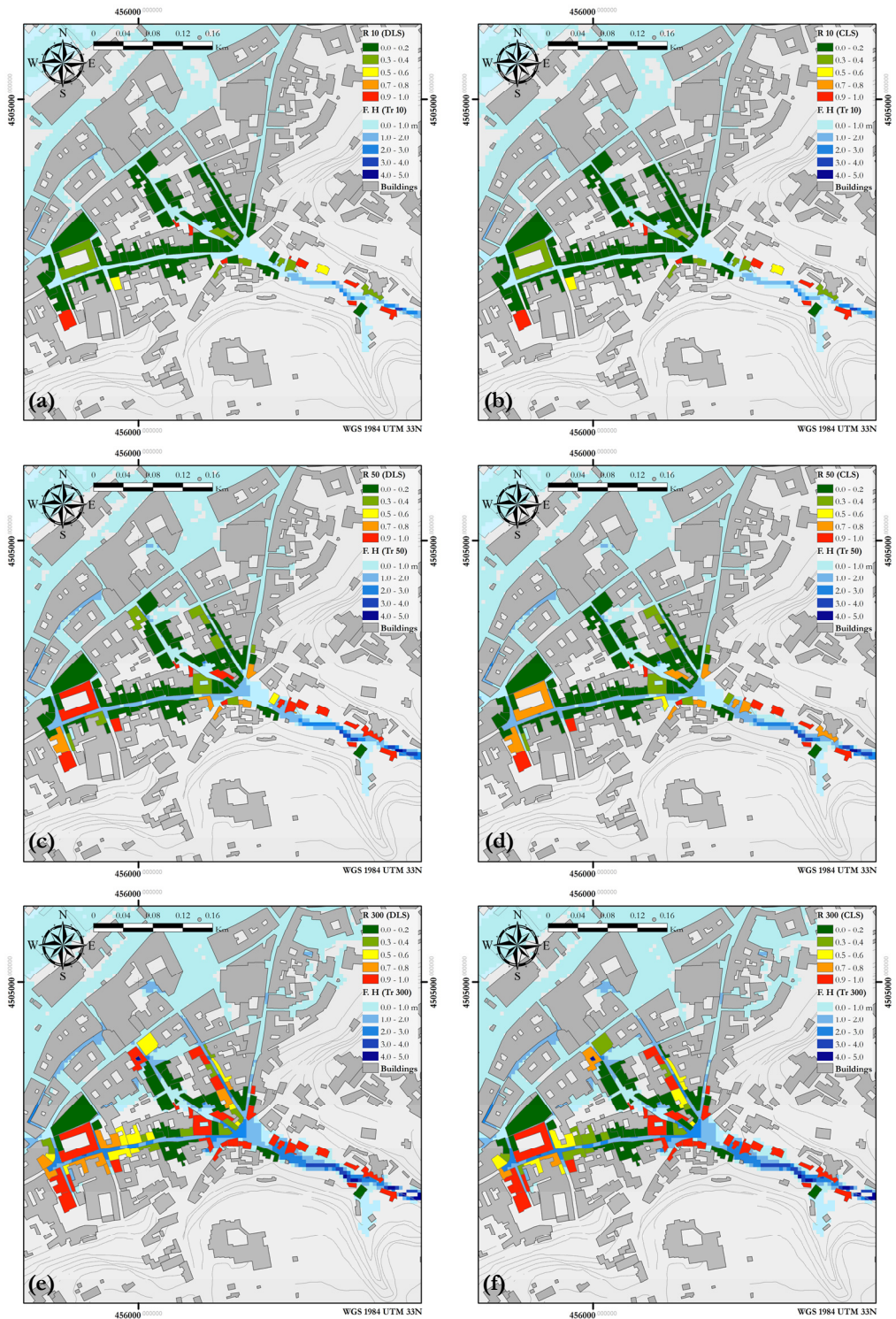


Fig. 5-34: (a), (c) and (e): The probability of exceeding the DLS in 10, 50 and 300 years, respectively. (b), (d) and (f): the probability of exceeding the CLS in 10, 50 and 300 years, respectively.

---

# Chapter 6

## Conclusions and final remarks

This thesis proposes a probabilistic framework for performance-based structural reliability assessment in case of rainfall-induced hydrogeological phenomena. The financial losses and casualties induced by natural disasters clearly indicate the necessity of a viable framework for analytical hydrogeological risk assessment. The thesis is mainly focused on debris flow and flooding. Two phenomena that are ranked at the second place (after earthquake) in the classification of the most catastrophic natural disasters. Due to its geological and geomorphological characteristics, Italy is almost completely prone to rainfall-induced natural hazards. Hence, all the three case-study applications are in Italy. Nevertheless, the developed framework, methods and tools are perfectly transferable to other locations and contexts.

In **Chapter 1**, a brief introduction of the motivations and the scope of this work is presented. To facilitate the reading of the thesis, some space is dedicated to the basic definitions and to a general overview on the performance-based approach. One of the main challenges of the work is to manage in a systematic way the interaction between the several expertises needed in this field (i.e., geological, geotechnical, hydrological, hydraulic, structural engineering, probabilistic and reliability assessment). In this sense, the performance-based framework also acts as a “glue” that helps in putting together the work and competence of the disciplines involved in a formal and structured manner.

In **Chapter 2**, the methodology adopted in this thesis for evaluating the rainfall-induced hydrogeological hazard is described. Even if this thesis focuses on analytic vulnerability assessment, a brief description of the adopted hazard assessment procedures has been reported in this chapter. Hazard assessment for the two main investigated phenomena (debris flow and flood) are described with particular attention on the fundamental differences that distinguish hazard assessment for floods from that of the

landslides. While for flooding it is possible to obtain a hazard curves described in terms of flood height and /or velocity versus return period; for debris flow phenomena, the question is much more complex. In case of debris flow, in fact, the event does not depend only on the return period of the rainfall that triggers the debris flow but it also depends on the boundary and initial conditions of the slope. The knowledge of these conditions is almost never available in un-gauged conditions. Therefore, a scenario-based approach has been adopted in this thesis for debris flow. The numerical procedure employed for propagating the flow on a bi-dimensional lattice, adopted both for flooding and debris flow, is also described in this chapter.

In **Chapter 3**, the proposed methodology for hydrogeological vulnerability assessment is outlined in detail. The procedure presented in this chapter aims at fragility assessment for a class of buildings and, without loss of generality, it can be applied to fragility assessment for a single building. A detailed literature review is reported in order to contextualize the work and to underline the current state of the art in the hydrogeological vulnerability assessment. The original performance-based framework has been implemented for the rainfall-induced hydrogeological phenomena by deriving the underlying risk formulation and by appropriately defining the intensity measure (flow height and/or velocity) and the performance variable (*DCR*, the Demand on Capacity Ratio).

The chapter presents a thorough examination of all the sources of uncertainty present in the problem (i.e., the uncertainties in definition of the structural geometry, the material mechanical properties and the loads). The uncertainties present in the problem are propagated by employing a Monte Carlo Simulation (MCS) scheme. A standard Monte Carlo simulation is executed by generating a finite number of random realizations of the vector of uncertain parameters based on their joint probability distribution. Each realization of the vector of uncertain parameters can be used in order to perfectly define a structural model which is going to be analysed by following an incremental analysis procedure in order to find the structural capacity (expressed in terms of critical flow height or velocity) for a given limit state. Finally, an efficient Bayesian procedure has been employed to calculate the fragility curves considering also the uncertainties in the estimation of the parameters of the adopted fragility model.

The adopted structural model consists of bi-dimensional Finite-Element-based models of the building walls –the element that is directly subjected to hydrogeological-induced actions. The wall masonry material is considered linear-elastic up to failure. The hydrogeological actions are classified into static, dynamic and impact actions. These actions are considered in combination with the gravity loads acting on the structure. The safety checks are performed in a step-by-step manner in order to verify the performance of the elements with respect to potential in-plane and out-of-plane mechanisms (i.e., overturning, bending, shear out-of-plane, shear in-plane) in a step-by-step manner during the incremental analyses.

In **Chapter 4**, the new software platform HydRA is presented. This Object Oriented Java tool implements the proposed framework for vulnerability (and risk) assessment, with particular attention to the simplicity of its use and to the representation of the output. A specific declarative commands language has been developed (similar to tcl for Opensees) in order to define all the input data needed for the hydrogeological risk assessment. The main advantages of HydRA are: the flexibility in adding new features, the possibility to use it on any kind of operating system; the possibility to install it on a server and to access it from a web page; the opportunity to use it both as an independent software or as a middleware (e.g., it can be interfaced via Matlab). An exhaustive description of all the commands and the input and output parameters is reported. Finally, a complete illustrative example of Hydra execution is presented.

In **Chapter 5**, the proposed risk framework has been applied to three different case studies. In order to validate the structural model and the analysis procedure, the first application example is focused on a single masonry building in Scaletta Zanclea (Messina, Italy) affected by the debris flow event of 2009. This is a fully deterministic example application and the results of the structural analysis are compared with the structure's observed damage. In the next example application, with the objective of validating the fragility assessment procedure, the damages incurred by the debris flow event of 1998 to the buildings located in the Episcopio district (Sarno) have been analytically simulated. Finally, an application of the risk assessment framework has been presented in order to evaluate the risk to both flooding and debris flow for a portfolio of buildings located in the Castellammare di Stabia (Naples, Italy).

The main achievements of this thesis can be summarized in two points. In the first place, the proposed framework lays out a viable methodology for performance-based reliability assessment with respect to rainfall-induced phenomena. This is done with specific attention to the hydrogeological context and the structural analysis necessary to achieve the vulnerability assessment. This framework can represent the basis for an operational decision support system applicable to urban areas prone to rainfall-induced hazards. In the second place, HydRA is developed as a software instrument that helps in realizing the capabilities of the proposed risk assessment framework. In fact, HydRA makes it possible to apply the methodological framework efficiently, based on few instructions, and with the maximum possible control of the output.

The presented risk assessment framework can be viewed as a mosaic composed of several aspects; each one of these aspects can be improved in the near future. Moreover, in order to validate and improve the assumed numerical models, it is very important to experimentally test (and to characterize) the local response of the single structural elements (and also the global response of the whole structure) subjected to hydrostatic and hydrodynamic actions. This could be achieved by devising specific test setup capable of simulate the hydrogeological-induced actions on the structures.

Another important consideration with regard to future developments regards the possibility of characterizing the debris flow triggering analytically and by careful characterization of the sources of uncertainty involved in the problem. This would fill in one of the fundamental voids in the procedure of debris flow risk assessment for a certain rainfall scenario.

Finally, HydRA can be improved by not only including the methodological advances in the analytical vulnerability assessment, but also by implementing the hazard assessment procedure for rainfall-induced hydrogeological phenomena.



---

## References

- AASHTO, A. A. o. S. H. a. T. O. (1998). *LRFD Bridge Design Specifications, 2nd edn. American Association of State Highways and Transportation Officials.*, Washington, DC., USA.
- Akbas, S., Blahut, J., and Sterlacchini, S. (2009). "Critical assessment of existing physical vulnerability estimation approaches for debris flows." *Landslide processes: from geomorphological mapping to dynamic modelling. CERG Editions, Strasbourg*, 229-233.
- Alcoverro, J., Corominas, J., and Gómez, M. (1999). "The Barranco de Arás flood of 7 August 1996 (Biescas, Central Pyrenees, Spain)." *Engineering Geology*, 51(4), 237-255.
- Ancey, C. (2001). "21 Debris Flows and Related Phenomena." *Geomorphological fluid mechanics*, Springer, 528-547.
- Aronica, G., Brigandi, G., Marletta, C., and Manfrè, B. (2009). "Hydrological and hydraulic analysis of the flash flood event on 25 October 2007 in North-Eastern part of Sicily, Italy."
- Aronica, G., Brigandi, G., and Morey, N. "Flash floods and debris flow in the city area of Messina, north-east part of Sicily, Italy in October 2009: the case of the Giampilieri catchment." *Proc., 12th Plinius Conference on Mediterranean Storms, held September 1-4, 2010 in Corfu Island, Greece.*, 98.
- Aronica, G. T., Biondi, G., Brigandi, G., Cascone, E., Lanza, S., and Randazzo, G. (2012). "Assessment and mapping of debris-flow risk in a small catchment in eastern Sicily through integrated numerical simulations and GIS." *Physics and Chemistry of the Earth, Parts A/B/C*, 49, 52-63.
- Arya, S., and Hegemier, G. "On non-linear response predictions of concrete masonry assemblies." *Proc., Proceedings of the North American Masonry Conference*, 19.11-19.24.
- Augenti, N. (2004). *Il calcolo sismico degli edifici in muratura*, Utet.
- Augenti, N., and Parisi, F. (2010). "Constitutive models for tuff masonry under uniaxial compression." *Journal of Materials in Civil Engineering*, 22(11), 1102-1111.
- Augenti, N., Parisi, F., and Acconcia, E. (2011). "Il Codice RAN per l'analisi sismica non lineare di edifici in muratura." *Progettazione Sismica*, 1, 139-157.
- Augenti, N., Parisi, F., and Acconcia, E. "MADA: online experimental database for mechanical modelling of existing masonry assemblages." *Proc., Proceedings of the 15th world conference on earthquake engineering, Lisbon, Portugal*, 24-28.
- Autority of Po River Basin, A. (2007). "Edifici in aree a rischio di alluvione: come ridurre la vulnerabilità."
- Bell, R., and Glade, T. (2004). "Quantitative risk analysis for landslides? Examples from

- 
- Bíldudalur, NW-Iceland." *Natural Hazards and Earth System Science*, 4(1), 117-131.
- Borga, M., Boscolo, P., Zanon, F., and Sangati, M. (2007). "Hydrometeorological analysis of the 29 August 2003 flash flood in the Eastern Italian Alps." *Journal of Hydrometeorology*, 8(5), 1049-1067.
- Botija, M. d. C. L., de Batlle, J., Rigo, T., and Barriendos, M. (2001). "Las inundaciones del 10 junio del 2000 en Cataluña." *Ingeniería del agua*, 8(1).
- Bouchard, B. (2007). "Improving flood risk management in informal settlements of Cape Town."
- Box, G. E. P., and Tiao, G. C. (1992). *Bayesian Inference in Statistical Analysis*, John Wiley & Sons, Inc.
- Caine, N. (1980). "The rainfall intensity: duration control of shallow landslides and debris flows." *Geografiska Annaler. Series A. Physical Geography*, 23-27.
- Calcaterra, D., De Riso, R., Evangelista, A., Nicotera, M., Santo, A., and Scotto di Santolo, A. "Slope instabilities of the pyroclastic deposits in the Phlegraean district and in the carbonate Apennine (Campania, Italy)." *Proc., Proc. Intern. Workshop on Occurrence and Mechanisms of Flows in Natural Slopes and Earthfills, Sorrento, Italy*, 61-75.
- Calcaterra, D., Parise, M., Palma, B., and Pelella, L. (2000). "Multiple debris flows in volcanoclastic materials mantling carbonate slopes." *Debris-flow hazards mitigation: mechanics, prediction, and assessment. Balkema, Rotterdam*, 99-107.
- Calcaterra, D., and Santo, A. (2004). "The January 10, 1997 Pozzano landslide, Sorrento Peninsula, Italy." *Engineering Geology*, 75(2), 181-200.
- Caliò, I., Marletta, M., and Pantò, B. (2012). "A new discrete element model for the evaluation of the seismic behaviour of unreinforced masonry buildings." *Engineering Structures*, 40, 327-338.
- Calvi, G., and Magenes, G. (1991). "Experimental evaluation of seismic strength of old masonry structures." *Brick and Block Masonry*, 1, 490-497.
- Capozucca, R. "Masonry panels with different mortar joints under compression." *Proc., Proc., 13th Int. Brick and Block Masonry Conf*, 27-34.
- Carozza, S., De Risi, R., and Jalayer, F. (2013). "D2.5 - Guideline to Decreasing Physical Vulnerability in the Three Considered Cities." *CLUVA project - Climate Change and Urban Vulnerability in Africa*.
- Carozza, S., Jalayer, F., De Risi, R., Manfredi, G., and Mbuya, E. (2015). "Comparing alternative flood mitigation strategies for non-engineered masonry structures using Demand and Capacity Factored Design." *ICASP12, 12th International Conference on Application of Statistics and Probability in Civil Engineering* Vancouver.
- Cascini, L., Cuomo, S., and Guida, D. (2008). "Typical source areas of May 1998 flow-like mass movements in the Campania region, Southern Italy." *Engineering Geology*, 96(3), 107-125.
- CEN (2004). "Eurocode 6: Design of masonry structures—Part 1–1: Common rules for reinforced and unreinforced masonry structures." ENV 1996-1-1: 2004: E, CEN Brussels.
- Charvet, I., Ioannou, I., Rossetto, T., Suppasri, A., and Imamura, F. (2014). "Empirical fragility assessment of buildings affected by the 2011 Great East Japan tsunami using improved statistical models." *Natural Hazards*, 1-23.
- Chen, J., Shieh, C., and Lin, C. (2004). "Topographic properties of debris flow in Central Taiwan." *J Chin Soil Water Conserv*, 35(1), 25-34.
- Chow, V. T., Maidment, D. R., and Mays, L. W. (1988). *Applied hydrology*.
- Chuxian, S. "Analysis of the strength for compressive members of brick masonry under
-

- eccentric loads." *Proc., Proc., CIB 3rd Int. Symp. on Wall Structures*, CIB Warsaw, Poland.
- Connolly, R. D., Schirmer, J., and Dunn, P. K. (1998). "A daily rainfall disaggregation model." *Agricultural and Forest Meteorology*, 92, 105-117.
- Cornell, C. A., Jalayer, F., Hamburger, R. O., and Foutch, D. A. (2002). "Probabilistic basis for 2000 SAC Federal Emergency Management Agency steel moment frame guidelines." *Journal of Structural Engineering*, 128(4), 526-533.
- Cornell, C. A., and Krawinkler, H. (2000). "Progress and challenges in seismic performance assessment." *PEER Center News*, 3(2), 1-3.
- Coussot, P., and Meunier, M. (1996). "Recognition, classification and mechanical description of debris flows." *Earth-Science Reviews*, 40(3), 209-227.
- Cruden, D. M., and Varnes, D. J. (1996). "Landslides: investigation and mitigation. Chapter 3-Landslide types and processes." *Transportation research board special report*(247).
- Davis, S. A. (1985). "Business Depth-Damage Analysis Procedures." DTIC Document.
- Dawson, R., Hall, J., Sayers, P., Bates, P., and Rosu, C. (2005). "Sampling-based flood risk analysis for fluvial dike systems." *Stochastic Environmental Research and Risk Assessment*, 19(6), 388-402.
- de Felice, G. (2009). "Assessment of the load-carrying capacity of multi-span masonry arch bridges using fibre beam elements." *Engineering Structures*, 31(8), 1634-1647.
- De Paola, F., De Risi, R., Di Crescenzo, G., Giugni, M., Santo, A., and Speranza, G. (2015). "Probabilistic Assessment of Debris Flow Peak Discharge by Monte Carlo Simulation." *ASCE-ASME Journal of Risk and Uncertainty in Engineering Systems, Part A: Civil Engineering*, A4015002.
- De Risi, R., Jalayer, F., De Paola, F., Iervolino, I., Giugni, M., Topa, M., Mbuya, E., Kyessi, A., Manfredi, G., and Gasparini, P. (2013). "Flood risk assessment for informal settlements." *Natural hazards*, 69(1), 1003-1032.
- Deierlein, G., Krawinkler, H., and Cornell, C. "A framework for performance-based earthquake engineering." *Proc., Pacific conference on earthquake engineering*, Citeseer, 1-8.
- Di Crescenzo, G., and Santo, A. (1999). "Analisi geomorfologica delle frane da scorrimento-colta rapida in depositi piroclastici della Penisola Sorrentina."
- Di Crescenzo, G., and Santo, A. (2005). "Debris slides—rapid earth flows in the carbonate massifs of the Campania region (Southern Italy): morphological and morphometric data for evaluating triggering susceptibility." *Geomorphology*, 66(1), 255-276.
- Ditlevsen, O., and Madsen, H. O. (1996). *Structural reliability methods*, Citeseer.
- Dvorkin, E. N., and Bathe, K.-J. (1984). "A continuum mechanics based four-node shell element for general non-linear analysis." *Engineering computations*, 1(1), 77-88.
- EU (2007). "Directive 2007/60/EC of the European Parliament and of the council of 23 October 2007 on the assessment and management of flood risks.", E. P. a. C. o. t. E. U. (2007), ed., Off. J. Eur. Union Legis., 27–34.
- Faella, C., and Nigro, E. "Dynamic impact of the debris flows on the constructions during the hydrogeological disaster in Campania-1998: failure mechanical models and evaluation of the impact velocity." *Proc., Proceedings of the international conference on FSM, Naples, Italy*, 179-186.
- FEMA, F. E. M. A. (1995). *Report 259. Engineering principles and practices for retrofitting floodprone residential buildings*, Washington, D.C., USA.
- FEMA, F. E. M. A. (2000). "Manual Coastal Construction." Federal Emergency Management Agency, Washington, D.C., USA.
- FEMA, F. E. M. A. (2000). *Report 356. Prestandard and commentary for the seismic rehabilitation of*

- 
- buildings*, Washington, D.C., USA.
- Fuchs, S., Heiss, K., and Hübl, J. (2007). "Towards an empirical vulnerability function for use in debris flow risk assessment." *Natural Hazards and Earth System Science*, 7(5), 495-506.
- Furtado, A., Rodrigues, H., and Arêde, A. (2015). "Modelling of masonry infill walls participation in the seismic behaviour of RC buildings using OpenSees." *International Journal of Advanced Structural Engineering (IJASE)*, 7(2), 117-127.
- Gambarotta, L., and Lagomarsino, S. (1997). "Damage models for the seismic response of brick masonry shear walls. Part II: the continuum model and its applications." *Earthquake engineering & structural dynamics*, 26(4), 441-462.
- Gaume, E., Bain, V. and Bernardara, P. (2008). "Primary Flash flood Data." *Work Package 1 Report for HYDRATE*, EC Project No. GOCE-CT-2004-505420.
- Gaume, E., Livet, M., Desbordes, M., and Villeneuve, J.-P. (2004). "Hydrological analysis of the river Aude, France, flash flood on 12 and 13 November 1999." *Journal of Hydrology*, 286(1), 135-154.
- Georgakakos, K. P. (1986). "On the Design of National, Real-Time Warning Systems with Capability for Site-Specific, Flash-Flood Forecasts." *B Am Meteorol Soc*, 67(10), 1233-1239.
- Giandotti, M. (1934). "Previsione delle piene e delle magre dei corsi d'acqua, Memorie e studi idrografici, Pubbl. 2 del Servizio Idrografico Italiano: Rome, Italy, Vol." VIII, 107.
- Gosling, J. (2000). *The Java language specification*, Addison-Wesley Professional.
- Gregoretto, C., and Fontana, G. D. (2008). "The triggering of debris flow due to channel-bed failure in some alpine headwater basins of the Dolomites: Analyses of critical runoff." *Hydrological processes*, 22(13), 2248-2263.
- Griffith, M. C., Vaculik, J., Lam, N., Wilson, J., and Lumantarna, E. (2007). "Cyclic testing of unreinforced masonry walls in two-way bending." *Earthquake Engineering & Structural Dynamics*, 36(6), 801-821.
- Groenevelt, P. H., and Grunthal, P. E. (1998). "Utilisation of crumb rubber as a soil amendment for sports turf." *Soil Till Res*, 47(1-2), 169-172.
- Guadagno, F. "20. Debris flows in the Campanian volcanoclastic soils." *Proc., Slope Stability Engineering: Developments and Applications: Proceedings of the International Conference on Slope Stability*, Thomas Telford, 125.
- Guha-Sapir, D., and Hoyois, P. (2012). "Measuring the human and economic impact of disasters." UCL.
- Guidi, G., Da Porto, F., Dalla Benetta, M., Verlato, N., and Modena, C. (2013). "Comportamento sperimentale nel piano e fuori piano di tamponamenti in muratura armata e rinforzata." *Proceedings of the XV ANIDIS, L'Ingegneria Sismica in Italia, Padua, Italy*, 30.
- Güntner, A., Olsson, J., Calver, A., and Gannon, B. (2001). "Cascade-based disaggregation of continuous rainfall time series: the influence of climate." *Hydrology and Earth System Sciences Discussions*, 5(2), 145-164.
- Haugen, E. D., and Kaynia, A. M. (2008). "Vulnerability of structures impacted by debris flow." *Landslides and Engineered Slopes: From the Past to the Future, Vols 1 and 2*, 381-387.
- Highland, L. (2004). "Landslide types and processes."
- Hoare, C. A. R. (1969). "An axiomatic basis for computer programming." *Communications of*

- the ACM*, 12(10), 576-580.
- Huet, P., Martin, X., Prime, J.-L., Foin, P., Laurain, C., and Cannard, P. (2003). "Retour d'expérience des crues de septembre 2002 dans les départements du Gard, de l'Hérault, du Vaucluse, des Bouches-du-Rhône, de l'Ardèche et de la Drôme." *Rapport IGE (Inspection Générale de l'Environnement)*.
- IBC (2008). "Italian Building Code, DM 14.01. 2008: Norme tecnica per le costruzioni." *Italian Ministry of Infrastructures and Transportation, Rome*.
- Jakob, M. (2005). "A size classification for debris flows." *Engineering geology*, 79(3), 151-161.
- Jalayer, F., Aronica, G. T., Recupero, A., Carozza, S., and Manfredi, G. (2016). "Debris Flow Damage Incurred to Buildings: An In-Situ Back Analysis." *Journal of Flood Risk Management*.
- Jalayer, F., Carozza, S., De Risi, R., Manfredi, G., and Mbuya, E. (2016). "Performance-based flood safety-checking for non-engineered masonry structures." *Engineering Structures*, 106, 109-123.
- Jalayer, F., and Cornell, C. A. (2004). *A technical framework for probability-based demand and capacity factor design (DCFD) seismic formats*, Pacific Earthquake Engineering Research Center.
- Jalayer, F., De Risi, R., Elefante, L., and Manfredi, G. (2013). "Robust fragility assessment using Bayesian parameter estimation." *Vienna Congress on Recent Advances in Earthquake Engineering and Structural Dynamics 2013 (VEESD 2013)*, R. H. C. Adam, W. Lenhardt & C. Schranz, ed. Vienna, Austria.
- Jalayer, F., De Risi, R., and Manfredi, G. (2015). "Bayesian Cloud Analysis: efficient structural fragility assessment using linear regression." *Bulletin of Earthquake Engineering*, 13(4), 1183-1203.
- Jaynes, E. T. (2003). *Probability theory: The logic of science*, Cambridge university press.
- Jennrich, R. I., and Sampson, P. (1976). "Newton-Raphson and related algorithms for maximum likelihood variance component estimation." *Technometrics*, 18(1), 11-17.
- Jonkman, S. N., Vrijling, J. K., and Vrouwenvelder, A. C. W. M. (2008). "Methods for the estimation of loss of life due to floods: a literature review and a proposal for a new method." *Natural Hazards*, 46, 353-389.
- Kaushik, H. B., Rai, D. C., and Jain, S. K. (2007). "Stress-strain characteristics of clay brick masonry under uniaxial compression." *Journal of materials in Civil Engineering*, 19(9), 728-739.
- Kelman, I. (2002). "Ph.D Thesis: Physical flood vulnerability of residential properties in coastal, eastern England." University of Cambridge.
- Kelman, I., and Spence, R. (2004). "An overview of flood actions on buildings." *Engineering Geology*, 73(3), 297-309.
- Koutsoyiannis, D., Kozonis, D., and Manetas, A. (1998). "A mathematical framework for studying rainfall intensity-duration-frequency relationships." *Journal of Hydrology*, 206(1-2), 118-135.
- Kron, W. (2002). "Keynote lecture: Flood risk= hazard x exposure x vulnerability." *Flood Defence*, 82-97.
- Lagomarsino, S., Penna, A., Galasco, A., and Cattari, S. (2013). "TREMURI program: an equivalent frame model for the nonlinear seismic analysis of masonry buildings." *Engineering Structures*, 56, 1787-1799.
- Larsen, M., Wicczorek, G., Eaton, L., Morgan, B., and Torres-Sierra, H. (2002). "Natural hazards on alluvial fans; The Venezuela debris flow and flash flood disaster."
- Lemos, J. (1998). "Discrete element modelling of the seismic behaviour of stone masonry

- 
- arches." *Computer methods in structural masonry*, 4, 220-227.
- Lighthill, M. J. (1958). *An introduction to Fourier analysis and generalised functions*, Cambridge University Press.
- Lourenco, P. B. (1996). *Computational strategies for masonry structures*, TU Delft, Delft University of Technology.
- Luciano, R., and Sacco, E. (1998). "A damage model for masonry structures." *European Journal of Mechanics-A/Solids*, 17(2), 285-303.
- MacCormack, R., and Paullay, A. (1972). "Computational efficiency achieved by time splitting of finite difference operators."
- Magenes, G. "A method for pushover analysis in seismic assessment of masonry buildings." *Proc., Proceedings of the 12th world conference on earthquake engineering*.
- Maione, U., and Mosiello, U. (1993). *Elementi di statistica per l'idrologia*.
- Manning, R., Griffith, J. P., Pigot, T., and Vernon-Harcourt, L. F. (1890). *On the flow of water in open channels and pipes*.
- Martino, L. (2015). "Analisi dell'impatto delle colate rapide di fango in ambito urbano. Il caso studio di Sarno (SA) 1998.", University of Naples "Federico II".
- Marzocchi, W., Garcia-Aristizabal, A., Gasparini, P., Mastellone, M. L., and Di Ruocco, A. (2012). "Basic principles of multi-risk assessment: a case study in Italy." *Natural hazards*, 62(2), 551-573.
- Mavrouli, O., Fotopoulou, S., Ptilakis, K., Zuccaro, G., Corominas, J., Santo, A., Cacace, F., De Gregorio, D., Di Crescenzo, G., and Foerster, E. (2014). "Vulnerability assessment for reinforced concrete buildings exposed to landslides." *Bulletin of Engineering Geology and the Environment*, 73(2), 265-289.
- McKenna, F., Fenves, G. L., and Scott, M. H. (2006). "OpenSees: Open system for earthquake engineering simulation." *Pacific Earthquake Engineering Center, University of California, Berkeley, CA*.
- Metropolis, N. (1987). "The beginning of the Monte Carlo method." *Los Alamos Science*, 15(584), 125-130.
- NAASRA, N. A. o. A. S. R. A. (1990). *Highway Bridge Design Specification.*, Sydney, Australia.
- Nadal, N. C., Zapata, R. E., Pagán, I., López, R., and Agudelo, J. (2009). "Building damage due to riverine and coastal floods." *Journal of Water Resources Planning and Management*, 136(3), 327-336.
- Nigro, E., and Faella, C. "Landslides as a secondary event of earthquakes and eruptions." *Proc., Urban Habitat Constructions Under Catastrophic Events: Proceedings of the COST C26 Action Final Conference*, CRC Press, 153.
- NRC, N. R. C. (1982). "Selecting a methodology for delineating mudslide hazard areas for the National Flood Insurance Program." *National Academy Press, Washington, D.C.*, C. o. M. f. P. M. Areas, ed.
- O'Brien, J., Garcia, R., Rodruiguez, J., Nardi, F., and Jorgensen, C. (2009). "FLO-2D Reference Manual." *FLO-2D Inc.: Nutrioso, AZ, USA*.
- O'Brien, J., and Julien, P. (1985). "Physical properties and mechanics of hyperconcentrated sediment flows." *Proc. ASCE HD Delineation of landslides, flash flood and debris flow Hazards*.
- Olsson, J. (1998). "Evaluation of a scaling cascade model for temporal rain-fall disaggregation." *Hydrology and Earth System Sciences Discussions*, 2(1), 19-30.
- Pagano, L., Picarelli, L., Rianna, G., and Urciuoli, G. (2010). "A simple numerical procedure for timely prediction of precipitation-induced landslides in unsaturated pyroclastic soils." *Landslides*, 7(3), 273-289.
-

- Pagnoni, T. "Seismic analysis of masonry and block structures with the discrete element method." *Proc., Proc 10th European conference on earthquake engineering*, 1674-1694.
- Papathoma-Köhle, M., Zischg, A., Fuchs, S., Glade, T., and Keiler, M. (2015). "Loss estimation for landslides in mountain areas—An integrated toolbox for vulnerability assessment and damage documentation." *Environmental Modelling & Software*, 63, 156-169.
- Parisi, F., Lignola, G., Augenti, N., Prota, A., and Manfredi, G. (2011). "Nonlinear behavior of a masonry subassemblage before and after strengthening with inorganic matrix-grid composites." *Journal of Composites for Construction*, 15(5), 821-832.
- Pereira, M. F. P., Pereira, M., Ferreira, J., and Lourenço, P. B. "Behavior of masonry infill panels in RC frames subjected to in plane and out of plane loads." *Proc., 7th International Conference on Analytical Models and New Concepts in Concrete and Masonry Structures*.
- Picarelli, L., Olivares, L., Comegna, L., and Damiano, E. (2008). "Mechanical aspects of flow-like movements in granular and fine grained soils." *Rock Mechanics and Rock Engineering*, 41(1), 179-197.
- Picarelli, L., Olivares, L., Damiano, E., Comegna, L., Greco, R., Mercogliano, P., and Zeni, L. "Short-term prediction of rainfall-induced flow-like landslides in unsaturated granular soils." *Proc., IV Simposio Panamericano de Deslizamientos "Vulnerabilidad y Gestión del Riesgo en Centro y Sur America"*, Sociedad Colombiana de Geotecnia, 1-22.
- Pina-Henriques, J., and Lourenço, P. "Masonry micro-modelling adopting a discontinuous framework." *Proc., Proceedings of the 7th international conference on computational structures technology, Lisbon, Portugal, vol paper*.
- Pistrika, A. (2009). "Flood Damage Estimation based on Flood Simulation Scenarios and a GIS Platform." *EWRA 7th International Conference "Water Resources Conservancy and Risk Reduction Under Climatic Instability"* Limassol, Cyprus, 419-427.
- Pistrika, A., and Tsakiris, G. (2007). "Flood risk assessment: A methodological framework." *Water Resources Management: New Approaches and Technologies. European Water Resources Association, Chania, Crete-Greece*.
- Pokkunuri, B. P. (1989). "Object oriented programming." *ACM Sigplan Notices*, 24(11), 96-101.
- Quan Luna, B., Blahut, J., Van Westen, C., Sterlacchini, S., van Asch, T. W., and Akbas, S. (2011). "The application of numerical debris flow modelling for the generation of physical vulnerability curves." *Natural Hazards and Earth System Science*, 11(7), 2047-2060.
- Raka, E., Spacone, E., Sepe, V., and Camata, G. (2015). "Advanced frame element for seismic analysis of masonry structures: model formulation and validation." *Earthquake Engineering & Structural Dynamics*, 44(14), 2489-2506.
- Restrepo, P., Cannon, S., Laber, J., Jorgensen, D., and Werner, K. "NOAA/USGS demonstration flash-flood and debris-flow early-warning system for recently burned areas in Southern California, USA." *Proc., 7th International Conference on Geomorphology. Australia*.
- Roos, W., Waarts, P., and Vrouwenfelder, A. (2003). "Damage to buildings." *Delft Cluster paper*.
- Rossi, F., and Villani, P. (1994). "Regional flood estimation methods." *Coping with floods*, Springer, 135-169.
- Rumbaugh, J., Blaha, M., Premerlani, W., Eddy, F., and Lorensen, W. E. (1991). *Object-oriented modeling and design*, Prentice-hall Englewood Cliffs, NJ.

- 
- Sawko, F. "Numerical analysis of brick walls under compressive loading." *Proc., Proc. Br. Ceram. Soc.*, 213.
- Scawthorn, C., Blais, N., Seligson, H., Tate, E., Mifflin, E., Thomas, W., Murphy, J., and Jones, C. (2006). "HAZUS-MH flood loss estimation methodology. I: Overview and flood hazard characterization." *Natural Hazards Review*, 7(2), 60-71.
- Scawthorn, C., Flores, P., Blais, N., Seligson, H., Tate, E., Chang, S., Mifflin, E., Thomas, W., Murphy, J., and Jones, C. (2006). "HAZUS-MH flood loss estimation methodology. II. Damage and loss assessment." *Natural Hazards Review*, 7(2), 72-81.
- Schwarz, J., and Maiwald, H. (2008). "Damage and loss prediction model based on the vulnerability of building types." *4th International symposium of Flood Defence* Toronto, Canada.
- Schwarz, J., and Maiwald, H. (2012). "Empirical vulnerability assessment and damage for description natural hazards following the principles of modern macroseismic scales." *14th WCEE - World Conference of Earthquake Engineering* Lisboa, Portugal.
- SCS, U. S. S. C. S. (1972). *SCS national engineering handbook, section 4: hydrology*, The Service.
- Sincaian, G. E. (2001). "Seismic behaviour of blocky masonry structures. A discrete element method approach." *Civil Engineering PhD Thesis*.
- Smith, D. (1994). "Flood damage estimation- A review of urban stage-damage curves and loss functions." *Water S. A.*, 20(3), 231-238.
- Smith, D. I., and Greenaway, M. A. (1988). "The computer assessment of urban flood damage: ANUFLOOD." *Newton, R W., Sharpe, R., and Taylor, MA R (eds.), Desktop Planning, Advanced Microcomputer Applications for Physical and Social Infrastructure Planning, Hargreen, Melbourne*, 239-250.
- Soleimankhani, H., Carozza, S., Aronica, G. T., Jalayer, F., and Recupero, A. "Analytic Back Calculation of Debris Flow Damage Incurred to a Masonry Building: The Case of Scaletta Zanclea 2009 Event." *Proc., E3S Web of Conferences*, EDP Sciences, 201.
- Spinella, N., Colajanni, P., and Recupero, A. (2014). "Experimental in situ behaviour of unreinforced masonry elements retrofitted by pre-tensioned stainless steel ribbons." *Construction and Building Materials*, 73, 740-753.
- Sweeney, T. L. (1992). *Modernized areal flash flood guidance*, US Department of Commerce, National Oceanic and Atmospheric Administration, National Weather Service, Office of Hydrology.
- Takahashi, T. (1978). "Mechanical characteristics of debris flow." *Journal of the Hydraulics Division*, 104(8), 1153-1169.
- Takahashi, T. (1991). *Debris flow*, Balkema.
- Tapsell, S. M., Penning-Rowsell, E. C., Tunstall, S. M., and Wilson, T. L. (2002). "Vulnerability to flooding: health and social dimensions." *Philos T Roy Soc A*, 360(1796), 1511-1525.
- Tassios, T. (1987). "The mechanics of masonry." *Athens: Symmetria Publishing*.
- Torres, M. A., Jaimes, M. A., Reinoso, E., and Ordaz, M. (2013). "Event-based approach for probabilistic flood risk assessment." *International Journal of River Basin Management*(ahead-of-print), 1-13.
- Totschnig, R., and Fuchs, S. (2013). "Mountain torrents: quantifying vulnerability and assessing uncertainties." *Engineering Geology*, 155, 31-44.
- Trigila, A., Iadanza, C., Bussetini, M., Lastoria, B., and A, B. (2015). "Dissesto idrogeologico in Italia: pericolosità e indicatori di rischio. Rapporto 2015.", ISPRA, Istituto Superiore per la Protezione e la Ricerca Ambientale.
-



- Tubino, M., and Lanzoni, S. (1993). "Rheology of debris flows: experimental observations and modelling problems." *Excerpta of the Italian Contributions to the Field of Hydraulic Engineering*, 7, 201-236.
- Turazza, D. (1880). "Delle formule più appropriate per il calcolo degli scoli delle basse pianure del modo di valutare le portate massime." *Atti dell'Istituto Veneto*.
- Turnšek, V., and Čačovič, F. "Some experimental results on the strength of brick masonry walls." *Proc., Proceedings of the 2nd international brick-masonry conference. British Ceramic Society, Stoke-on-Trent*, 149-156.
- UNISDR (2009). "UNISDR Terminology for Disaster Risk Reduction." *United Nations International Strategy for Disaster Reduction (UNISDR) Geneva, Switzerland*.
- Viparelli, C. (1963). "Ricostruzione dell'idrogramma di piena." *L'Energia Elettrica*, 6, 421-428.
- Viparelli, M. (1961). "Air and water currents in vertical shafts." *La Huille Blanche*, 16(857869.8).
- Zanchetta, G., Sulpizio, R., Pareschi, M., Leoni, F., and Santacroce, R. (2004). "Characteristics of May 5–6, 1998 volcanoclastic debris flows in the Sarno area (Campania, southern Italy): relationships to structural damage and hazard zonation." *Journal of volcanology and geothermal research*, 133(1), 377-393.



---

# List of Figures

Fig. 1-1: Inhabitants of highly landslide prone areas in Italian regions (Trigila et al. 2015).	13
Fig. 1-2: Inhabitants of highly flood prone areas in Italian regions (Trigila et al. 2015).	13
Fig. 1-3: Contents flow chart.	15
Fig. 1-4: Relation between the four generic variables of performance based framework.	17
Fig. 1-5: Localization of the case studies.	19
Fig. 1-6: Localization of the case study building (Jalayer et al. 2016).	21
Fig. 1-7: Case-study building before and after the event of October 2009.	21
Fig. 1-8: Overview of the main flow-like mass movements in May 1998 (Cascini et al. 2008).	22
Fig. 1-9: Portfolio of affected buildings in Episcopio district (Zanchetta et al. 2004)	23
Fig. 1-10: Portfolio of buildings considered in Castellammare di Stabia.	24
Fig. 2-1: Types of landslides (Highland 2004)	26
Fig. 2-2: Landslide rate of movement (velocity) classification taken from Cruden and Varnes (1996).	26
Fig. 2-3: flow classification as a function of sediment concentration (NRC 1982).	27
Fig. 2-4: Main morphological parameters of a debris flow (Di Crescenzo and Santo 2005).	28
Fig. 2-5: Size classification for debris flow (Jakob 2005).	29
Fig. 2-6: Probability distribution of debris flow discharge.	33
Fig. 2-7: Physical processes simulated by FLO-2D (O'Brien et al. 2009).	36
Fig. 2-8: (a) discharge flow across the sections in FLO-2D; (b) eight considered flow directions. (O'Brien et al. 2009).	37
Fig. 2-9: Dynamic viscosity function of volumetric concentration (O'Brien et al. 2009).	38
Fig. 2-10: Yield stress function of volumetric concentration (O'Brien et al. 2009).	38
Fig. 3-1: Example of probability distributions fit. From the left to right: uniform, normal and log-normal distribution fit.	48
Fig. 3-2: Example of building shapes.	49

Fig. 3-3: MCS framework for structural fragility assessment. _____	52
Fig. 3-4: Sampling from a marginal cumulative distribution function (CDF) _____	52
Fig. 3-5: Incremental analysis curves. _____	53
Fig. 3-6: The schematic diagram: robust fragility and the plus/minus one standard deviation confidence interval, hazard curve and the DCFD safety checking format. ____	58
Fig. 3-7: Some cases of damage produced by the event of Sarno (SA, Italy) 1998. (Courtesy of Dr. Melania De Falco and Vigili del Fuoco). _____	59
Fig. 3-8: The Representative Volume Element (RVE) proposed by Pina-Henriques and Lourenço (2004). _____	61
Fig. 3-9: Example of mesh discretization of a wall for the FEM analysis. _____	61
Fig. 3-10: The four-nodes shell element proposed by Dvorkin and Bathe (1984). _____	61
Fig. 3-11: A representation of generic loads applied to a wall. _____	62
Fig. 3-12: (a) Velocity profile along the height. (b) Approximate velocity profile. _____	64
Fig. 3-13: hydrostatic and hydrodynamic pressure profiles. _____	64
Fig. 3-14: Experimental constitutive laws for 8 tuff masonry specimens (Augenti and Parisi 2010). _____	66
Fig. 3-15: Comparison between different predictive constitutive models. _____	66
Fig. 3-16: Walls failure mechanisms. _____	68
Fig. 3-17: Forces (a) and stresses (b) that govern the considered failure mechanisms. ____	69
Fig. 4-1: Infographic on HyDRA workflow. _____	76
Fig. 4-2: Check the version of Java SE Runtime Environment. _____	86
Fig. 4-3: Check the version of TCL/TK interpreter. _____	87
Fig. 4-4: Analysis progress. _____	87
Fig. 4-5: Incremental analysis curves for the DLS. _____	90
Fig. 4-6: Incremental analysis curves for CLS. _____	90
Fig. 4-7: Fragility curves for the two considered Limit States. _____	91
Fig. 4-8: Demand to Capacity Ratio (DCR) for the simulated wall #2 at step #1 of analysis ( $H = 1.0\text{m} - V = 0.0\text{m/s}$ ). _____	91
Fig. 5-1: Reconstructed liquid and solid flood hydrograph. _____	94
Fig. 5-2: Maps of: (a) maximum flow depths, colour scale in meters; (b) maximum flow velocity modules, colour scale in m/s; (c) maximum total hydrodynamic force for unit width, colour scale in kN/m; (d) identification of the case study building (Jalayer et al. 2016) _____	95
Fig. 5-3: Test set-up for the panel in compression. _____	96
Fig. 5-4: Building before and after the event of October 2009. _____	96
Fig. 5-5: (a) the damaged wing modelled in HyDRA; (b) the three-dimensional substructure modelled in the fine elements; (c) the geometric configuration of the eastern wall; (d) the geometric configuration of the northern wall. _____	97
Fig. 5-6: (a) the footprint of the debris flow (the maximum depth) on the eastern wall (W2); (b) the footprint of the debris flow on the northern wall (W1); (c) hydrostatic and	

hydrodynamic force component profiles over the height of the wall _____	99
Fig. 5-7: Footprint of the velocity distribution on the modelled walls. _____	100
Fig. 5-8: Incremental analysis curves for the modelled substructure ( $V_{\text{flow}}=5\text{m/s}$ ). _____	100
Fig. 5-9: DCR of the wall W1 ( $H_{\text{flow}}=3\text{m}$ and $V_{\text{flow}}=5\text{m/s}$ ) for the mechanisms: (a) overturning; (b) bending; (c) shear in-plane; (d) shear out-of-plane. _____	101
Fig. 5-10: DCR of the wall W2 ( $H_{\text{flow}}=3\text{m}$ and $V_{\text{flow}}=5\text{m/s}$ ) for the mechanisms: (a) overturning; (b) bending; (c) shear in-plane; (d) shear out-of-plane. _____	101
Fig. 5-11: Comparison between the analysis results in terms of shear in-plane DCR of wall 2 (a) and bending DCR of wall 1 (b) with respect to the observed damage (c). _____	102
Fig. 5-12: The simulated Debris flow scenario in term of flow height (courtesy of G. Speranza, L. Martino and F. De Paola) _____	103
Fig. 5-13: Debris flow scenarios map in term of flow velocity (courtesy of G. Speranza, L. Martino and F. De Paola) _____	104
Fig. 5-14: The portfolio of buildings located in the Episcopio district, Sarno _____	105
Fig. 5-15: Fragility curves for class “RCO” at DLS (dashed lines) and CLS (solid lines). _____	108
Fig. 5-16: Fragility curves for class “MA1” at DLS (dashed lines) and CLS (solid lines). _____	108
Fig. 5-17: Fragility curves for class “MA2” at DLS (dashed lines) and CLS (solid lines). _____	109
Fig. 5-18: Fragility curves for class “MA3” at DLS (dashed lines) and CLS (solid lines). _____	109
Fig. 5-19: (a) observed damage after the event of 1998; (b) probability of exceeding the DLS in one year (analytic simulation of the event). _____	110
Fig. 5-20: Maps of three debris flow scenarios. (a), (c) and (e) represent the flow height for the minimum, the average and the maximum volume scenarios, respectively. (b), (d) and (f) represent the flow velocity for the minimum, the average and the maximum volume scenarios, respectively. _____	112
Fig. 5-21: Flooding hazard maps. (a), (c) and (e) represent the flooding height for return periods 10, 50 and 300 years, respectively. (b), (d) and (f) represent the flooding velocity for return periods 10, 50, and 300 years, respectively. _____	113
Fig. 5-22: the two building portfolios considered _____	114
Fig. 5-23: Break-down of the main features of the surveyed buildings. _____	115
Fig. 5-24: Map of the structural classes. _____	115
Fig. 5-25: Fragility curves for class “MA1” at DLS (dashed lines) and CLS (solid lines). _____	118
Fig. 5-26: Fragility curves for class “MA2” at DLS (dashed lines) and CLS (solid lines). _____	118
Fig. 5-27: Fragility curves for class “MA3” at DLS (dashed lines) and CLS (solid lines). _____	119
Fig. 5-28: Fragility curves for class “MA4” at DLS (dashed lines) and CLS (solid lines). _____	119
Fig. 5-29: Fragility curves for class “MAP” at DLS (dashed lines) and CLS (solid lines). _____	119
Fig. 5-30: Fragility curves for class “RCO” at DLS (dashed lines) and CLS (solid lines). _____	120
Fig. 5-31: Example of fragility curve interpolation for class “MA2”. _____	121
Fig. 5-32: (a) DCFD map for damage limit state (DLS) with acceptable risk corresponding to 50 years return period; (b) the map of return period capacities. _____	122
Fig. 5-33: (a), (c) and (e): probability of exceeding the DLS for the minimum, the average	

---

and the maximum volume scenarios, respectively. (b), (d) and (f): probability of exceeding the CLS for the minimum, the average and the maximum volume scenarios, respectively.

\_\_\_\_\_ 123

Fig. 5-34: (a), (c) and (e): The probability of exceeding the DLS in 10, 50 and 300 years, respectively. (b), (d) and (f): the probability of exceeding the CLS in 10, 50 and 300 years, respectively. \_\_\_\_\_ 124

---

# List of Tables

Tab. 1-1: Natural hazards subgroup definition and classification based on (Guha-Sapir and Hoyois 2012)	11
Tab. 1-2: Debris flow events in Castellammare di Stabia in the last 100 years.	24
Tab. 2-1: Statistics of topographic and debris-flow characteristic parameters (Chen et al. 2004).	33
Tab. 2-2: Yield stress and viscosity as function of sediment concentration (O'Brien et al. 2009). Conversion: Shear stress, 1 Pa = 10 dynes/cm <sup>2</sup> ; Viscosity, 1 Pa·sec = 10 dynes·sec/cm <sup>2</sup> = 10 poises.	39
Tab. 3-1: The uncertainties in geometrical parameters	49
Tab. 3-2: The uncertainties in material mechanical properties	49
Tab. 3-3: The uncertain in loading parameters	50
Tab. 3-4: Material characteristic parameters.	67
Tab. 3-5: Limit states definition for structural/non-structural walls.	71
Tab. 4-1: Global results description.	84
Tab. 4-2: Description of simulations results: the incremental analysis curve.	85
Tab. 4-3: Simulations results description: stresses and safety checks.	86
Tab. 4-4: The global results of the analysis.	89
Tab. 5-1: Geometrical uncertainties. Distributions: uniform U [min; max]; log-normal LN [median; logarithmic standard deviation]; fixed F [fixed value].	106
Tab. 5-2: Materials uncertainties. Distributions: uniform U [min; max]; log-normal LN [median; logarithmic standard deviation]; fixed F [fixed value].	107
Tab. 5-3: The uncertainties in loading parameters. Distributions: uniform U [min; max]; log-normal LN [median; logarithmic standard deviation]; fixed F [fixed value].	107
Tab. 5-4: The uncertainties in the geometrical parameters. Distributions: uniform U [min; max]; log-normal LN [median; logarithmic standard deviation]; fixed F [fixed value].	116
Tab. 5-5: The uncertainties in material mechanical properties. Distributions: uniform U [min; max]; log-normal LN [median; logarithmic standard deviation]; fixed F [fixed value].	117

---

---

Tab. 5-6: The uncertainties in loading parameters. Distributions: uniform U [min; max]; log-normal LN [median; logarithmic standard deviation]; fixed F [fixed value]. \_\_\_\_\_ 117